Machine learning in pre- and post-manufacturing stages of active array antennas

Onat, N.B.

DOI
10.4233/uuid:3655c889-58e2-4dc7-bc7c-a52533c9ae39

Publication date
2025

Document Version
Final published version

Citation (APA)
Onat, N. B. (2025). *Machine learning in pre- and post-manufacturing stages of active array antennas*. [Dissertation (TU Delft), Delft University of Technology]. https://doi.org/10.4233/uuid:3655c889-58e2-4dc7-bc7c-a52533c9ae39

Important note
To cite this publication, please use the final published version (if applicable).
Please check the document version above.

MACHINE LEARNING IN PRE- AND POST-MANUFACTURING STAGES OF ACTIVE ARRAY ANTENNAS

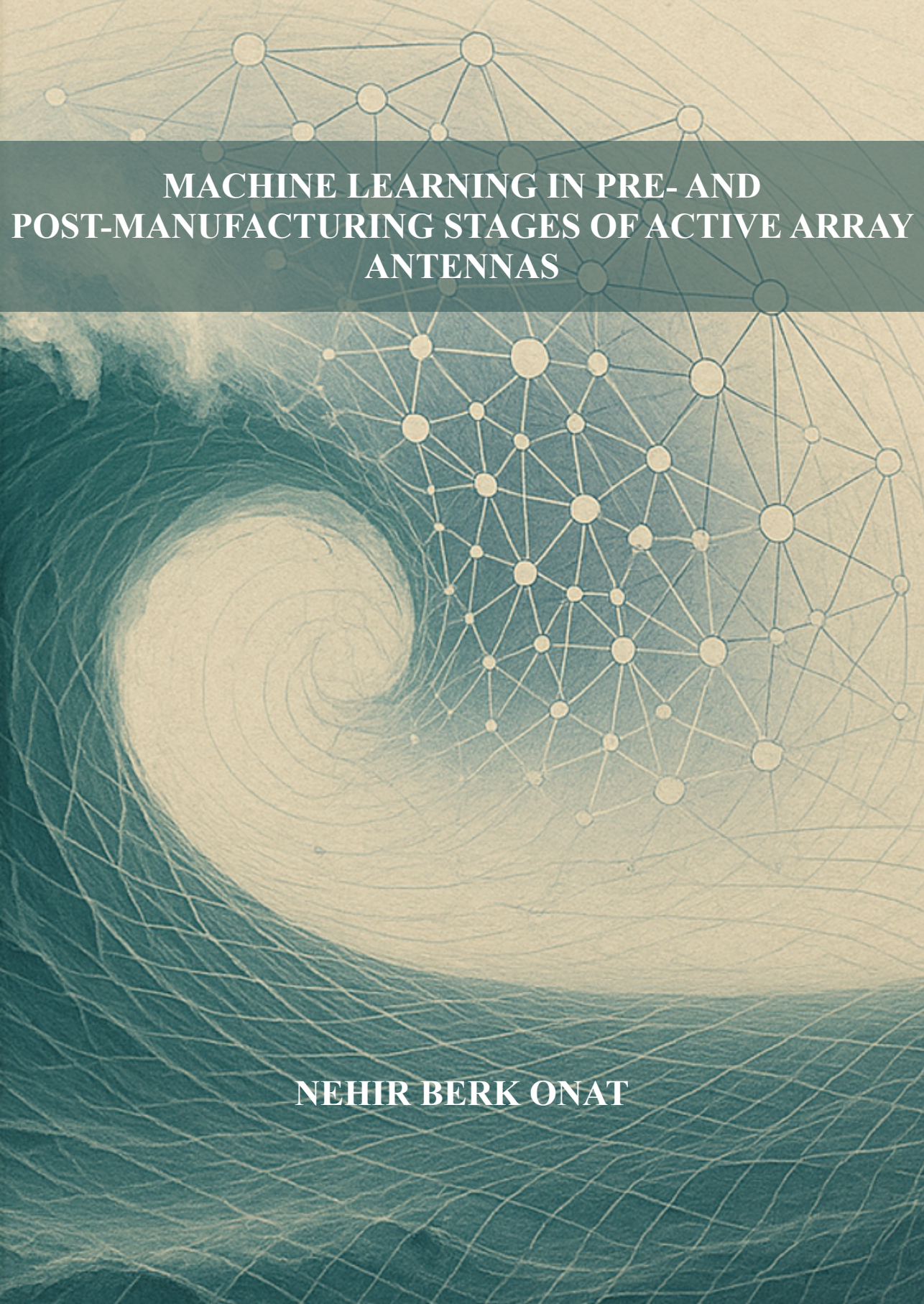

NEHIR BERK ONAT

Machine Learning in Pre- and Post-Manufacturing Stages of Active Array Antennas

MACHINE LEARNING IN PRE- AND POST-MANUFACTURING STAGES OF ACTIVE ARRAY ANTENNAS

Dissertation

for the purpose of obtaining the degree of doctor
at Delft University of Technology
by the authority of the Rector Magnificus, Prof. dr. ir. T.H.J.J. van der Hagen,
chair of the Board for Doctorates
to be defended publicly on
Tuesday 11 November 2025 at 17:30 o'clock

by

Nehir Berk ONAT

Master of Science in Electrical Engineering,
Eindhoven University of Technology, The Netherlands
born in Alanya, Türkiye

This dissertation has been approved by the promotors.

Composition of the doctoral committee:

Rector Magnificus,	chairperson
Prof. dr. A. Yarovoy	Delft University of Technology, promotor
Dr. Y. Aslan	Delft University of Technology, copromotor
Independent members:	
Prof. dr. ir. M.C. van Beurden	Eindhoven University of Technology
Prof. dr. ir. F.P. Widdershoven	Delft University of Technology
Prof. dr. S. Pollin	Katholieke Universiteit Leuven, Belgium
Prof. dr. M.J. Uetz	University of Twente
Dr. ir. R.F. Remis	Delft University of Technology
Reserve member:	
Prof. dr. ir. W. van Driel	Delft University of Technology

This research has been carried out at the Delft University of Technology in the Microwave Sensing, Signals and Systems (MS3) group.

Keywords: Active Arrays, Machine Learning, Mutual Coupling, Antenna Pattern.

Printed by: Proefschriftspecialist, 1506RZ Zaandam, The Netherlands.

Front & Back: Designed by N.B. Onat.

ISBN/EAN: 978-94-6384-869-5 (Paperback/Softback)
ISBN/EAN: 978-94-6518-171-4 (E-Book/PDF)

An electronic version of this dissertation is available at
http://repository.tudelft.nl/.

Author e-mail: nberkonat@gmail.com

To my family and my wife, for their endless love, patience and support.

CONTENTS

List of Acronyms

ADAM	Adaptive Moment Estimation
AUT	Antenna Under Test
CNN	Convolutional Neural Network
CCAA	Circularly Clustered Aperiodic Array
DoA	Direction of Arrival
DUCAT	Delft University Chamber for Antenna Tests
EEP	Embedded Element Pattern
EM	Electromagnetics
ESPCN	An Efficient Sub-pixel Convolutional Neural Network
E-Field	Electric Field
FoV	Field of View
FPGA	Field-Programmable Gate Array
GA	Genetic Algorithm
H-field	Magnetic Field
H-pol	Horizontal Polarization
IC	Integrated Circuit
IDM	Infinitesimal Dipole Modeling
MC	Mutual Coupling
MIMO	Multiple-Input and Multiple-Output
ML	Machine Learning
MSE	Mean Squared Error
MoM	Method of Moments
NF	Near Field
NN	Neural Network
PA	Power Amplifier
PINN	Physics Informed Neural Network
PCB	Printed Circuit Board
PSLL	Peak Sidelobe Level
PSO	Particle Swarm Optimization
RF	Radio Frequency
RX	Receiver
SLL	Sidelobe Level
SNR	Signal to Noise Ratio
SVD	Singular Value Decomposition
TX	Transmitter
OTA	Over-the-Air
VGA	Variable Gain Amplifier
V-pol	Vertical Polarization
X-pol	Cross Polarization

SUMMARY

The rapid advancement of next-generation wireless communication and sensing technologies demands high-performance, intelligent antenna systems capable of adaptive beamforming, efficient signal control, and reliable operation under dynamic conditions. Active phased arrays, especially when employing non-uniform (aperiodic) layouts, offer enhanced flexibility for power-efficient side-lobe control and improved spatial coverage. However, these benefits come at the cost of increased electromagnetic, thermal, and computational complexity. The realization of practical, IC-integrated aperiodic arrays therefore requires innovative design and diagnostic frameworks that can efficiently address challenges spanning both pre- and post-manufacturing stages.

Traditionally, the design and performance evaluation of active phased arrays have relied on deterministic electromagnetic simulations or optimization-based methods focusing primarily on radiation characteristics such as gain, beamwidth, and side-lobe levels (SLL). Yet, as arrays become increasingly complex, such methods face limitations in scalability, adaptability, and computational feasibility. Machine learning (ML) provides an emerging pathway to overcome these barriers by enabling data-driven modeling, optimization, and diagnosis of many types of large-scale or or non-uniform active arrays. This interdisciplinary challenge lies at the intersection of electromagnetics (EM), array modeling, and data-driven methods, requiring the development of frameworks that balance physical accuracy with computational efficiency.

The primary objective of this doctoral research is to develop and validate ML-based methodologies that enhance both the design and operation of active arrays, emphasizing efficient modeling, synthesis, and diagnosis under mutual coupling (MC), environmental effects and fabrication-induced uncertainties. The research addresses both pre-manufacturing (e.g., synthesis, EM modeling, and topology optimization) and post-manufacturing (e.g., calibration and fault detection) aspects of active arrays, with a focus on data-efficient and physics-supported ML techniques.

Chapter II introduces the underlying motivation, the state-of-the-art challenges in phased array systems, and the potential of ML in overcoming these limitations. A detailed analysis of pre- and post-manufacturing challenges highlights the critical issues of mutual coupling, irregular routing, calibration complexity, and environmental sensitivity. These observations establish the research need for intelligent, adaptive frameworks that integrate ML with physical modeling to enhance design reliability and post-deployment robustness.

Chapter III focuses on data-driven modeling of EM interactions in aperiodic phased arrays. A novel neural network (NN)-based framework is proposed for predicting embedded element patterns (EEPs) across the entire visible space for non-uniform planar arrays. The cascaded NN architecture, combining a fully connected NN and an efficient sub-pixel convolutional network, enables high-resolution pattern prediction with significant computational savings. The influence of dataset size and quality on prediction

reliability is analyzed, revealing critical insights into data efficiency and model generalization for large-scale array configurations.

Chapter IV expands upon these foundations by introducing hybrid ML-physics approaches to further improve prediction robustness. Two basis-function-assisted frameworks are developed using the Infinitesimal Dipole Model (IDM) and spherical harmonics. These models achieve compact, reliable EEP representation with smaller datasets while mitigating numerical instability. An ensemble learning method combining NN-based EEP prediction and constrained IDM is also introduced, achieving a 60% reduction in mean squared error (MSE) and improved prediction stability under MC effects. A stacked generalization strategy further enhances performance by optimally integrating multiple model outputs.

Chapter V applies these ML-assisted models to system-level synthesis and diagnostics. First, a novel ML-driven optimization method for MIMO radar arrays is proposed by integrating spherical harmonics-based EEP prediction into a particle swarm optimization (PSO) routine. This approach enables efficient MC-aware array topology design and minimizes maximum SLL in multi-beam configurations. Subsequently, ML-based post-manufacturing diagnostics are demonstrated for a 64-element active uniform array. A fully connected NN is trained using sparse far-field amplitude data to detect faulty elements in real time, offering a scalable, low-cost solution for performance monitoring and fault recovery.

The findings of this research collectively demonstrate that ML techniques can serve as a powerful tool to bridge the gap between EM theory and practical array implementation and operation. The developed frameworks offer data-efficient alternatives for MC-aware active array optimization, and system diagnostics, paving the way toward intelligent, reliable, and self-adaptive active array systems for future wireless communication and sensing applications.

SAMENVATTING

De snelle vooruitgang van de volgende generatie draadloze communicatie- en sensortechnologieën vraagt om performante, intelligente antennesystemen die in staat zijn tot adaptieve bundelvorming, efficiënte signaalsturing en betrouwbare werking onder dynamische omstandigheden. Actieve gefaseerde arrays bieden een grotere flexibiliteit voor energie-efficiënte controle van zijlobniveaus en verbeterde ruimtelijke dekking, vooral wanneer niet-uniforme (aperiodieke) opstellingen worden toegepast. Deze voordelen gaan echter gepaard met een toename van elektromagnetische, thermische en computationele complexiteit. De realisatie van praktische, IC-geïntegreerde aperiodieke arrays vereist daarom innovatieve ontwerptechnieken en diagnostische raamwerken die de uitdagingen in zowel de pre- als post-productiefase efficiënt kunnen aanpakken.

Traditioneel zijn het ontwerp en de prestatie-evaluatie van actieve gefaseerde arrays gebaseerd op deterministische elektromagnetische simulaties of optimalisatiemethoden die zich voornamelijk richten op stralingskarakteristieken zoals versterking, bundelbreedte en zijlobniveau (SLL). Naarmate arrays echter complexer worden, vertonen deze methoden beperkingen op het gebied van schaalbaarheid, aanpasbaarheid en rekenefficiëntie. Machine learning (ML) biedt een veelbelovende benadering om deze beperkingen te overwinnen door op data gebaseerde modellering, door optimalisatie en door de diagnose van vele soorten grootschalige of niet-uniforme actieve arrays mogelijk te maken. Deze interdisciplinaire uitdaging bevindt zich op het snijvlak van elektromagnetisme (EM), arraymodellering en op data gebaseerde methoden, en vereist de ontwikkeling van raamwerken die fysieke nauwkeurigheid combineren met computationele efficiëntie.

Het primaire doel van dit promotieonderzoek is het ontwikkelen en valideren van op ML gebaseerde methodologieën die zowel het ontwerp als de werking van actieve arrays verbeteren, met nadruk op efficiënte modellering, synthese en diagnose onder invloed van wederzijdse koppeling (MC), omgevingsinvloeden en onzekerheden die voortkomen uit de productie. Het onderzoek behandelt zowel de pre-productiefase (bijv. synthese, EM-modellering en topologie-optimalisatie) als de post-productiefase (bijv. kalibratie en foutdetectie) van actieve arrays, met een focus op data-efficiënte en fysisch onderbouwde ML-technieken.

Hoofdstuk II introduceert de onderliggende motivatie, de huidige stand van de techniek op het gebied van gefaseerde arraysystemen, en het potentieel van ML om deze beperkingen te overwinnen. Een gedetailleerde analyse van de pre- en post-productie uitdagingen benadrukt de kritieke kwesties van wederzijdse koppeling, onregelmatige routering, kalibratiecomplexiteit en omgevingsgevoeligheid. Deze observaties onderbouwen de noodzaak van intelligente, adaptieve raamwerken die ML integreren met fysische modellering om zowel de betrouwbaarheid van het ontwerp als de operationele robuustheid te verbeteren.

Hoofdstuk III richt zich op datagedreven modellering van elektromagnetische interacties in aperiodieke gefaseerde arrays. Een nieuw raamwerk, op neurale netwerken (NN) gebaseerd, wordt voorgesteld voor het voorspellen van ingebedde elementpatronen (EEP's) over de volledige zichtbare ruimte voor niet-uniforme vlakke arrays. De gelaagde NN-architectuur, die een volledig verbonden NN combineert met een efficiënte sub-pixel convolutionele netwerkstructuur, maakt hoge-resolutie patroonvoorspellingen mogelijk met significante besparingen in rekentijd. De invloed van datasetgrootte en -kwaliteit op de voorspellingsbetrouwbaarheid wordt geanalyseerd, wat cruciale inzichten oplevert in data-efficiëntie en modelgeneralisatie voor grootschalige arrayconfiguraties.

Hoofdstuk IV bouwt verder op deze fundamenten door hybride ML-fysica aanpakken te introduceren om de voorspellingsrobuustheid verder te verbeteren. Twee op basisfuncties gesteunde raamwerken worden ontwikkeld met behulp van het "Infinitesimal Dipole Model" (IDM) en sferische harmonischen. Deze modellen bereiken een compacte, betrouwbare representatie van EEP's met kleinere datasets, terwijl numerieke instabiliteit wordt verminderd. Verder wordt een "ensemble learning" methode voorgesteld, die NN-gebaseerde EEP voorspelling combineert met een beperkt IDM. Deze realiseert een reductie van 60% in de gemiddelde kwadratische fout (MSE) en een verbeterde voorspellingsstabiliteit onder MC-invloeden. Een strategie op basis van "stacked generalization" verbetert de prestaties verder door de uitvoer van meerdere modellen optimaal te combineren.

Hoofdstuk V past deze door ML ondersteunde modellen toe op systeemniveau synthese en diagnostiek. Allereerst wordt een nieuwe, door ML aangedreven optimalisatiemethode voor MIMO-radararrays voorgesteld, waarbij op sferische harmonischen gebaseerde EEP-voorspellingen worden geïntegreerd in een "particle swarm optimization" (PSO)-routine. Deze aanpak maakt efficiënte, MC-bewuste arraytopologie-ontwerpen mogelijk en minimaliseert het maximale SLL in configuraties met meervoudige bundels. Vervolgens worden ML-gebaseerde post-productie diagnostische technieken gedemonstreerd voor een actieve uniforme array met 64 elementen. Een volledig verbonden NN wordt getraind met behulp van schaarse ver-veld amplitudedata om defecte elementen in real-time te detecteren, wat een schaalbare en kostenefficiënte oplossing biedt voor prestatiemonitoring en foutherstel.

De bevindingen van dit onderzoek tonen gezamenlijk aan dat ML-technieken kunnen dienen als een krachtig hulpmiddel om de kloof tussen EM-theorie en praktische implementatie en werking van arrays te overbruggen. De ontwikkelde raamwerken bieden data-efficiënte alternatieven voor MC-bewuste optimalisatie van actieve arrays en systeemdiagnostiek, en effenen zo het pad naar intelligente, betrouwbare en zelf- adaptieve actieve arraysystemen voor toekomstige draadloze communicatie- en sensorapplicaties.

1

INTRODUCTION

1

1.1. THE ROLE OF ANTENNAS IN MODERN WIRELESS COMMUNICATION AND SENSING TECHNOLOGIES

The demand for advanced and reliable communication and sensing systems has grown significantly in recent years, driven by the rapid development of diverse technologies across various sectors. From wireless communications to radar-based applications, which cover a wide range of frequency bands from L-band (1-2 GHz) to S, C, X, Ku, Ka, up to W band (100 GHz), the need for systems that can support higher data rates, greater reliability, and enhanced performance has never been more critical. The evolution of communication networks and sensing has facilitated the growth of technologies like the Internet of Things (IoT), Machine-to-Machine (M2M) communication, and autonomous systems, all of which rely on robust wireless infrastructure.

The rapid evolution of communication networks is a central aspect of the technological landscape, with the 5G and 6G systems setting the stage for the next generation of wireless connectivity. These systems are designed to handle unprecedented data rates, ultra-low latency, and massive device connectivity, addressing the growing demand for high-speed communication, such as non-terrestrial networks. As the world becomes increasingly interconnected, reliable, high-capacity networks are more critical than ever. Beyond just speed, 5G and 6G aim to provide seamless connectivity across diverse environments, enabling innovations such as autonomous vehicles, internet over-satellite, immersive augmented and virtual reality experiences, and the continued expansion of IoT technologies. The challenge lies in designing efficient antenna systems, e.g., at base stations, payloads and user terminals, supporting these vast networks while ensuring security, scalability, and energy efficiency. The antenna systems, particularly when combined with beamforming capabilities, are instrumental in addressing the challenges posed by both emerging communication infrastructures and modern sensing platforms. The ability to dynamically steer and adapt radiation patterns is essential for systems that operate in increasingly congested and heterogeneous environments, where flexibility, precision, and adaptability are key.

Simultaneously, phased-array radar technology, which has long been used in defense, is increasingly adopted in civilian and industrial applications. In the automotive industry, radar is a cornerstone of advanced driver assistance systems (ADAS), enabling features such as adaptive cruise control, collision avoidance, and automated parking. The transition to higher frequency bands, such as 77 GHz, has improved the performance of automotive radar, allowing for better range and angular resolution, which is vital for the development of fully autonomous vehicles.

Radar also plays a key role in environmental monitoring. Advanced radar technologies like dual-polarization and phased array radars have revolutionized meteorology by offering more precise measurements of atmospheric conditions, enhancing weather forecasting, and improving our ability to monitor and respond to severe weather events. These radar systems enable better tracking of precipitation patterns and help meteorologists predict storms more accurately. Moreover, radar systems have found their way into human activity recognition (HAR), particularly in healthcare and smart home environments. Non-contact radar sensors can monitor vital signs, detect falls, and track movements in real time, offering a promising solution for elderly care and health moni-

Figure 1.1: The low frequency array (LOFAR) station composed by two regular high band antenna arrays [1].

toring. Similarly, in radio astronomy, large phased aperture-array antenna systems, such as the low frequency array (LOFAR) shown in Fig. 1.1 [1], are essential for probing the early universe, uncovering the origins and evolution of the cosmos, discovering planets, and monitoring space weather.

At the core of these advancements lies the optimal design of antennas, which are fundamental to the functionality of modern systems across various applications. As these technologies continue to evolve, understanding the key performance parameters of antennas becomes essential. Factors such as the antenna topology and beamforming weights, operating frequency, environmental influences, and the interaction between the antennas and circuits significantly affect the efficiency, radiation pattern, and overall performance of antenna systems. These critical parameters must be carefully con-

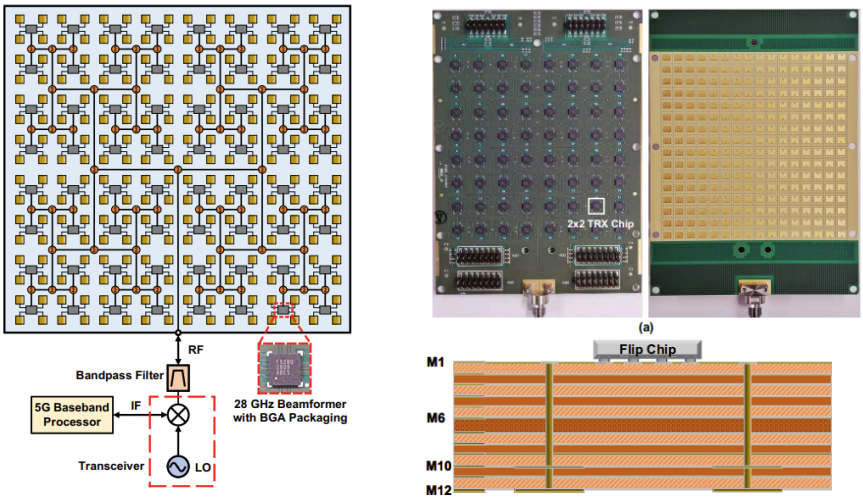

Figure 1.2: A 28 GHz 256-element active phased array for the 5G application [2].

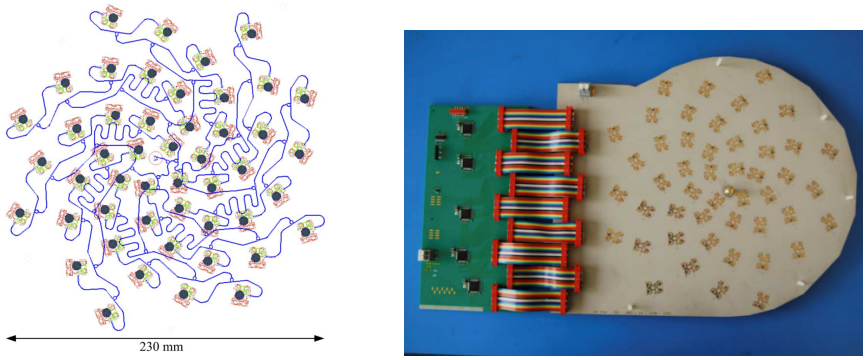

(a) (b)

Figure 1.3: An example aperiodic phased array for low-cost SatCom terminal antennas [3]. (a) Layout for the 48-element aperiodic array with beam forming network illustrated in blue; (b) Bottom view of the prototyped array with its control board.

sidered in the design process to ensure that antennas meet the requirements of their respective applications, whether for communication, sensing, or other advanced technologies.

(ACTIVE) PHASED ARRAYS AND STATE-OF-THE-ART CHALLENGES

Among the aforementioned developments, antenna design plays a crucial role, particularly in the context of active phased array systems that must meet demanding performance requirements. In the last decade, research has increasingly focused on integrated solutions where antennas are co-designed with multi- (4, 8 or 16) channel analog integrated circuits (ICs), enabling compact, silicon-based implementations [4–6], as Fig. 1.2 illustrates an example implementation of a 256-element phased array for 5G applications [2]. These active (i.e., IC-integrated) antenna systems aim to balance hardware and signal processing complexity, minimize calibration efforts, and ensure fast response times. A key enabling technology across these applications is adaptive beamforming, which allows dynamic control of radiation patterns to enhance signal quality, reduce interference, and support directive wireless communication and sensing.

Phased array antennas offer significant advantages over single-element antennas, including high gain, low side-lobe levels (SLL), and the ability to form shaped or multiple agile beams. These features make them widely used in wireless communications, radar, radio astronomy, and remote sensing [7]. In array synthesis, the radiation pattern can be tailored through adjustments in the number, position, and excitation of antenna elements. Among these options, non-uniformly spaced (aperiodic) phased arrays (e.g., see Fig. 1.3 [3]) have gained specific attention for offering greater design flexibility and enhanced power-efficient control over sidelobe levels (SLLs) [8, 9].

While these advancements broaden the capabilities of phased arrays, they also introduce significant performance challenges. The performance of active phased arrays, both uniform and non-uniform, depends on a range of interrelated factors that influence ra-

diation characteristics, impedance matching, and overall system efficiency. Ensuring reliable operation across diverse applications requires careful consideration of several key aspects. These challenges can be broadly categorized into pre- and post-manufacturing aspects, including but not limited to the examples summarized below.

- **Pre-Manufacturing Challenges:**

  Pre-manufacturing challenges in phased array design involve a combination of electromagnetic, computational, and physical layout complexities that must be addressed before fabrication. One of the most critical issues in this context is mutual coupling (MC), whose behavior is non-linear and highly dependent on geometry, frequency, and scan angle. These effects can significantly distort the embedded element patterns (EEPs) and reflection coefficients, making accurate modeling essential yet computationally intensive.

  Aperiodic arrays introduce additional complexity due to their irregular element spacing, which causes coupling between elements to vary significantly. Unlike periodic arrays, these interactions cannot be easily generalized or compensated in a straightforward manner. This variation complicates the synthesis process, often requiring multiple design iterations. Accurate modeling in such scenarios frequently depends on full-wave simulations, which become increasingly impractical for large or densely packed configurations. Moreover, because mutual coupling is often neglected during the early design phase, analytical predictions—especially regarding sidelobe performance—tend to be overly optimistic compared to real-world results.

  Physical design constraints further add to the challenge. In non-uniform layouts, routing between ICs and antenna elements becomes non-repetitive and irregular. Even when attempts are made to equalize path lengths, inconsistencies in amplitude and phase can arise, particularly at high frequencies where signal integrity is more sensitive. These combined electromagnetic and hardware-level factors make the design of active aperiodic arrays a highly complex, multi-domain problem that requires tight integration between modeling, layout, and system-level design.

- **Post-Manufacturing Challenges:** Post-manufacturing challenges typically arise from fabrication tolerances, assembly variations, and the impact of dynamic operating conditions that cannot be fully predicted during the design phase. One of the primary concerns is calibration. Differences in component behavior—particularly in aperiodic arrays, where elements may experience distinct routing paths and coupling effects—make uniform calibration difficult. Each element can exhibit different amplitude and phase characteristics due to both its geometric position and the associated electronic path.

  Environmental conditions also play a significant role in post-manufacturing behavior. Mechanical stress, temperature fluctuations, and the presence of nearby or dynamic scatterers, such as moving platforms or structural obstructions, can alter the effective behavior of the array. These changes often affect the mutual coupling dynamics, which are frequency-dependent and can vary across the operational

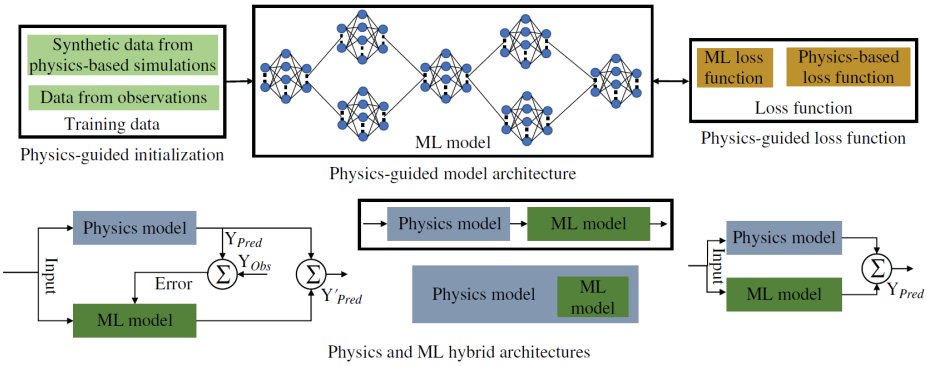

Figure 1.4: Physics-informed ML models [10].

bandwidth. On top of that, aging components, damaged ICs, or malfunctioning antenna elements can degrade performance and compromise system robustness over time.

Additionally, calibration procedures become more demanding in active aperiodic arrays due to their lack of regularity. Full calibration would ideally require characterizing each IC's response and the associated embedded element patterns across multiple operating conditions, including frequency, temperature, and IC control states. These variations must then be compensated dynamically to maintain consistent system performance, adding further complexity to post-manufacturing calibration workflows.

These post-manufacturing factors underscore the need for adaptive, intelligent methods that offer promising solutions for real-time correction, fault detection, and performance recovery. In addition, the pre-manufacturing challenges also highlight the growing need for design approaches that are efficient while remaining reliable. While machine learning (ML) has the potential to address many of these issues, it also plays a broader role in solving many complex EM problems.

1.2. THE ROLE OF MACHINE LEARNING IN WIRELESS COMMUNICATION AND SENSING

Machine learning (ML) is rapidly emerging as a robust framework enabling remarkable time and accuracy performance to solve highly non-linear complex EM problems[11]. Particularly, Neural networks (NNs) have become instrumental in parametric EM modeling and optimization. By capturing the relationship between the parameters and EM responses, trained NNs can provide rapid and accurate predictions, streamlining the simulation and design process. Furthermore, knowledge-based neural networks (KBNNs) or physics-informed neural networks (PINNs) [12] integrate prior physical models to improve accuracy, reduce training complexity and make the model physically consistent, as the example architecture is illustrated in Fig. 1.4. These techniques have collectively

transformed conventional EM modeling into a faster and more adaptive framework, enabling efficient high-performance component design with reduced computational overhead.

ML methodologies have been effectively applied to the modeling and optimization of various microwave components such as filters, couplers, and transmission lines [14], as well as for the synthesis of complex structures like microstrip circuits and vertical interconnects [15].

Applications such as compact lenses, spatial light modulators, holograms, and beam-steering devices require precise manipulation of phase and amplitude at sub-wavelength scales—capabilities made possible through ML models that map geometric features to EM responses. Therefore, the reconfigurable intelligence surface (RIS) design has also significantly benefited from deep learning techniques. Figure 1.5 illustrates an example ML framework for the inverse RIS design [13].

Another example of ML-driven methodologies in EM applications is in the biomedical domain, where it has enabled significant advancements in addressing the challenges of high-contrast inverse scattering problems [17, 18]. The developed models help enhance imaging quality while drastically reducing computational cost, making real-time or near-real-time imaging feasible. Such capabilities offer promising paths for medical diagnostics and monitoring applications based on electromagnetic sensing.

Direction of Arrival (DoA) estimation has also benefited from the integration of ML techniques, particularly in scenarios where traditional algorithms face limitations due to hardware constraints or environmental challenges. ML models have been applied to enhance the accuracy and robustness of DoA estimation by learning from observed data patterns, enabling better performance under low signal-to-noise ratios, limited snapshots, or incomplete sensor elements [19, 20]. These approaches offer a powerful alternative to classical methods, supporting real-time operation and improving the adaptability in dynamic environments.

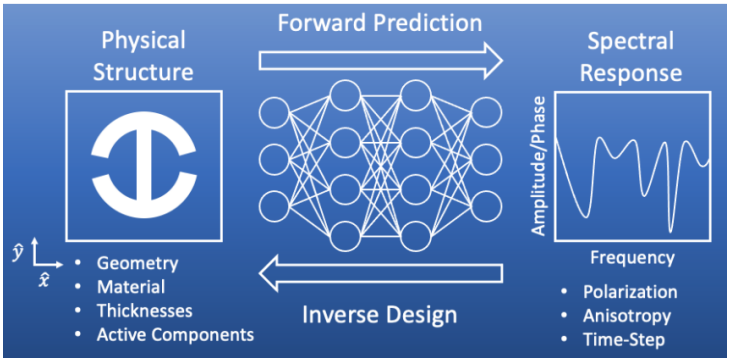

Figure 1.5: In inverse RIS design, ML algorithms learn and generalize complex EM relationships between the physical RIS structure (left column) and spectral response (right column) through training data [13].

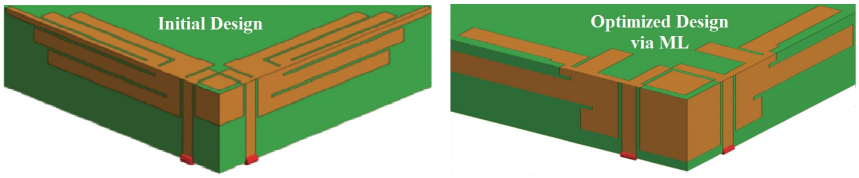

Figure 1.6: Optimized dual-port LTE Antenna Model with its initial design and ML-optimized design [16].

UTILIZATION OF ML IN THE FIELD OF (ACTIVE) ARRAYS AND CHALLENGES

As in the context of antenna design, data-driven models have enabled efficient design and parameter optimization by replacing computationally intensive simulations with fast, predictive tools [21]. An example of an ML application in antenna design is the optimization of an LTE dual-port antenna by Altair [16], as illustrated in Fig. 1.6. These applications highlight the role of ML in significantly reducing design time and computational cost while maintaining high accuracy across a range of EM design tasks. In addition, ML techniques have been applied in several phased array antenna studies for pattern prediction and array synthesis [22–24]. Rather than relying solely on array-level patterns, EEPs are often preferred, as they provide a more precise representation of how each element interacts with its environment. This level of detail is particularly important for calibration, as well as for advanced signal processing tasks, such as those in radar systems, where algorithms may operate directly on element-level responses instead of using conventional beamforming techniques.

Beyond the design phase, ML is increasingly being utilized to support real-time adaptation, calibration, and performance optimization of electromagnetic systems [25–27]. In dynamic environments, ML models can rapidly adjust system parameters to compensate for changing conditions, such as platform deformations, mutual coupling variations, or environmental disturbances, without the need for extensive recalibration or time-consuming simulations. This highlights the ML's growing role in addressing both pre- and post-processing challenges in phased array systems. However, despite its potential, the use of ML in antenna systems introduces its own set of challenges, listed as follows.

- **Data Quality and Generalization:** One of the primary challenges in applying ML to active phased arrays is creating datasets that accurately reflect the wide range of conditions these systems operate under. Variations in element geometry, spacing, excitation schemes, frequency ranges, and hardware characteristics must be represented to ensure generalization. A dataset that is too narrow (e.g., based only on ideal or uniform configurations) may lead to models that perform poorly when applied to real-world scenarios involving imperfections, mutual coupling, or environmental interactions. This is particularly important for aperiodic arrays, where the diversity of possible element locations significantly increases the complexity of the input space and must be adequately captured in the dataset.

- **Data Production:** Generating high-quality datasets for active phased arrays is often resource-intensive, as it typically requires full-wave simulations or extensive

measurement campaigns. This is especially demanding in large or aperiodic arrays where mutual coupling and non-ideal behaviors must be accurately captured. Additionally, creating training data for tasks like inverse synthesis or real-time beam correction can require expert knowledge and careful sampling to ensure broad coverage, adding to the complexity and cost of dataset preparation.

- **Model Selection and Complexity Management:** The nonlinear and high dimensional nature of active phased array behavior makes model selection a nontrivial task. Simpler models may fail to capture key dependencies such as those involving element interactions or frequency-dependent effects, while more complex architectures may be difficult to train, interpret, or deploy efficiently in real-time systems. Achieving a balance between model accuracy, computational cost, and interpretability remains a key design challenge.

- **Available Domain Knowledge:** Incorporating physical insights into ML models is often challenging in the context of active phased arrays, where interactions between electrical, thermal, and structural domains are tightly coupled. Embedding Maxwell-based constraints, array symmetries, or known behavioral patterns into learning frameworks (e.g., PINNs) in an effective way can improve generalization, reduce the need for massive training data, and enhance the reliability of the model.

1.3. RESEARCH OBJECTIVES AND NOVEL CONTRIBUTIONS

To address the aforementioned challenges in active phased array systems, this thesis aims to develop intelligent, data-driven frameworks that integrate ML techniques to improve the performance in the design and operational phases of these systems. The research focuses on exploring learning-based techniques to enhance the efficiency, scalability, and adaptability of phased array synthesis, optimization, and operational tasks. The objective is to improve performance and reliability in both pre-manufacturing (e.g., array synthesis and modeling with a focus on aperiodic array topologies) and post- manufacturing (e.g., real-time diagnosis) stages, while reducing design iteration cycles and computational burden. Ultimately, this work seeks to bridge the gap between traditional EM methodologies and learning-based solutions, offering scalable tools for next-generation communication and sensing applications.

These motivations give rise to a set of key research questions that define the scope and direction of this thesis:

1. How can data-driven methods support the practical design and implementation of aperiodic, IC-integrated active phased arrays by **addressing MC effects and layout-induced challenges in dynamic communication and sensing scenarios**?

2. How can MC effects in non-uniform planar arrays be effectively captured using data-driven models through accurate prediction of EEPs, **particularly under constraints of limited training data and array complexity**?

3. How can EEPs be efficiently represented through compact and reliable decomposition techniques, and how can these representations be leveraged to **enable accurate, robust, and data-efficient prediction under varying MC conditions**?

4. How can data-driven techniques be employed to enable MC-aware synthesis of MIMO arrays for **improved design performance and reliability under practical system-level constraints**?

5. How can these techniques be extended to support post-manufacturing diagnostics, **ensuring reliable operational behavior of active phased arrays in real-world environments**?

By addressing these research questions, the main contributions and results achieved in this thesis are summarized below:

- **A novel IC-integrated dual-polarized aperiodic phased array prototype (at 26 GHz) has been developed and experimentally validated,** serving as a practical proof of the challenges posed by non-uniform layouts, including complex routing, calibration difficulties, and the impact of MC effects in real-world implementations.
- **A novel neural network-based method has been proposed to predict embedded element patterns across the full visible space for non-uniform planar arrays**, significantly reducing computational load and highlighting the impact of dataset size on prediction reliability.
- **Two new alternative EEP prediction methods based on spherical wave expansion and constrained dipole modeling (IDM) have been proposed**, offering reduced dimensional complexity, and are combined within an ensemble framework to enhance accuracy and robustness under MC effects and data-limited conditions.
- **For the first time, MC-aware synthesis of aperiodic MIMO radar arrays has been demonstrated using ML models that predict embedded element patterns**, enabling efficient array optimization within a global optimizer (GO) framework.
- **A novel machine learning-based methodology, incorporating physics-informed neural networks, has been developed for real-time (fast) fault detection in mm-wave active phased arrays**, enabling fast and accurate diagnosis under IC nonlinearities and MC effects.

1.4. OUTLINE OF THE THESIS

Chapter 2 - *Active Aperiodic Phased Arrays: Design, Measurements and Challenges*
Presents the design and experimental validation of a novel IC-integrated, dual-polarized aperiodic phased array prototype. The chapter demonstrates the practical difficulties of implementing non-uniform layouts and identifies key challenges such as routing complexity, calibration difficulty, and mutual coupling effects. It also discusses the need for adaptive solutions in dynamic communication and sensing applications.

Chapter 3 - *ML-Based Embedded Element Pattern (EEP) Prediction and Challenges*
Introduces a preliminary NN-based framework to predict EEPs across the full visible

space for planar non-uniform arrays. A cascaded architecture combining low-resolution prediction with high-resolution upscaling is proposed to reduce computational cost in layout optimization. The impact of dataset size and quality on prediction accuracy is also thoroughly investigated.

Chapter 4 -*EEP Reconstruction Through Basis Functions*
Introduces two alternative methods for EEP prediction based on spherical wave expansion and constrained IDM. These approaches model antenna behavior using basis functions to reduce dimensional complexity and improve prediction stability in the presence of MC effects.

Chapter 5 -*Utilization of Basis Functions for EEP Prediction via Machine Learning*
Building on the basis function-based prediction methods, this chapter presents an ensemble learning framework that integrates multiple EEP prediction models to improve robustness and generalization. A two-branch hybrid architecture combining direct and indirect predictors is introduced, and further enhanced through a stacked generalization approach, which uses a meta-model to combine outputs from base learners, resulting in significantly improved accuracy of EEP prediction under MC effects and limited data conditions.

Chapter 6 -*Applications in Active Phased Arrays: Design and Diagnostics*
This chapter comprises two parts. The first part demonstrates the MC-aware synthesis of aperiodic MIMO radar arrays using ML-based EEP prediction via spherical wave expansion within a PSO framework. In the second part, the chapter presents a PINN approach for real-time fault detection in large-scale mm-wave active phased arrays, addressing challenges related to IC nonlinearities and mutual coupling in post-manufacturing diagnostics.

Chapter 7 -*Conclusions and Recommendations for Future Research*
The final chapter provides a comprehensive summary of the key findings and contributions presented throughout this thesis, highlighting the advancements made and their impact on the field. It also reflects on the limitations encountered and identifies promising directions for future research, outlining opportunities for further innovation and development.

2

Active Aperiodic Phased Arrays: Design, Measurements and Challenges

An active dual-polarized phased array with an aperiodic IC and antenna layout is designed and experimentally validated at 26 GHz. The array reuses components from a regular benchmark design and addresses practical challenges introduced by the non-uniform layout, including asymmetric RF routing, calibration complexity, and cross-polarization effects. A heuristic calibration procedure is developed to achieve near-uniform excitation and enable a fair performance comparison. Measurement results demonstrate significant sidelobe level (SLL) reduction with an acceptable impact on gain, beamwidth, and scan efficiency. The limitations of current modeling approaches, particularly regarding MC effects, are highlighted as motivation for the data-driven methods introduced in the following chapters.

Parts of this chapter have been published in:

Buenaventura-Camps, Marta and Aslan, Yanki and Freidl, Philipp and Aubry, Pascal and **Onat, Nehir Berk** and Janssen, Johan and Geurts, Marcel and Yarovoy, Alexander, "An Aperiodic mm-Wave Phased Array Controlled by Multi-Channel Analog Beamforming ICs," 2024 54th European Microwave Conference (EuMC), Paris, France, 2024, pp. 668-671.

And partly published in:

Y. Aslan, P. Aubry, **N. B. Onat**, J. Janssen, M. Geurts and A. Yarovoy, "Heuristic Over-the-Air Calibration of Beamformer ICs in Active mm-Wave Phased Arrays," 2023 IEEE Conference on Antenna Measurements and Applications (CAMA), Genoa, Italy, 2023, pp. 840-845, doi: 10.1109/CAMA57522.2023.10352655.

2.1. INTRODUCTION

There is a growing demand for power-efficient low-sidelobe silicon-based millimeter-wave (mm-wave) active phased arrays for the next-generation base stations, satellite user terminals and radars [28, 29]. At the current technology level, multi- (4 or 8) channel analog beamforming integrated circuits (ICs) are generally used to adjust the excitation weights of the antenna elements [30, 31]. The existing array systems from academia and the industry are all based on regular and symmetrical placement of the radiating elements [32–34]. The well-known benefit of this type of structure is low design and manufacturing complexity. However, unless power tapering is used, the periodicity of the topology leads to the appearance of the first few sidelobes that are too high to address the isolation requirements among multiple users (or targets) [35]. Additionally, the high density of elements on the antenna aperture causes thermal issues, which can deteriorate the performance and safety of the beamforming system [36].

Due to their high potential of achieving low sidelobes at optimal power efficiencies via spatial tapering [37], uniform-amplitude aperiodic arrays have been discussed in the literature from a mathematical perspective by focusing on different topology optimization strategies [38]. Although such algorithms provide excellent numerical results on the peak sidelobe level (PSLL) suppression, the practical design of the resulting phased array topologies in today's multi-channel IC technology for high-frequency applications has not yet been considered. The fully-irregular nature of such array layouts causes significant circuit routing challenges on the radio frequency (RF) signal distribution network and IC-to-antenna element feed lines, and results in serious calibration needs [39]. There are a few recent theory-level discussions on antenna clustering and mapping algorithms [40, 41], but, there is no prior work on practical non-regular distribution of the ICs and the realization of an asymmetrical feed network.

In this section, based on the mathematical optimization studies performed by the MS3 group at TU Delft [38, 41], we propose an innovative aperiodic-layout IC-integrated dual-polarized phased array system. The novelties are connected to the following achievements:

- placement and routing of dual-polarized multi-channel ICs in aperiodic arrays,
- design of an asymmetrical feeding network (from connectors to the beamforming ICs and from ICs to the array elements with equal propagation losses) for irregularly distributed ICs and antennas,
- prototyping of an aperiodic active phased array including the subsystems (i.e. the control, power and cooling units),
- heuristic IC calibration in aperiodic arrays,
- experimental verification of the aperiodic layout performance in active phased arrays.

This work (partly conducted as a M.Sc. thesis project at TU Delft [28]) re-uses as many components as possible (antenna element, IC, feed line, heat sink) from a reference regular array design [42] (see Fig. A.5) and calibration method [43]. The goal of

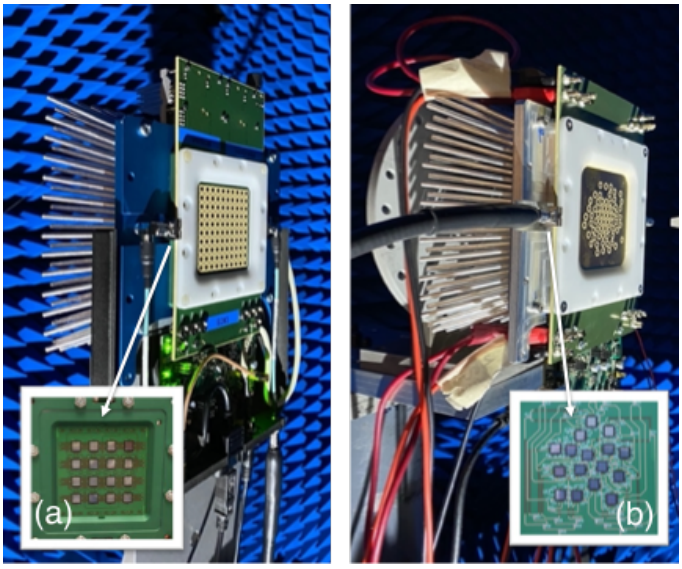

Figure 2.1: 64-element 26 GHz array: (a) square-grid [42], (b) aperiodic (new).

our work is to approximate uniform amplitudes and linearly progressive phases at the elements in both arrays for a fair comparison of the proposed topology with the conventional one, at the center frequency of 26 GHz. Addressing the feed network loss difference in the two arrays is left out of scope, as the position of the RF connectors is not optimized. This design work provides useful insights into identifying the challenges.

2.1.1. ARRAY SYSTEM DEVELOPMENT

ARRAY TOPOLOGY OPTIMIZATION

First, the methodology from [7] is executed, which utilizes iterative convex optimization, starting from initial regular topology every element moved in small step at each iteration, array factor (under no coupling) is linearized to realize a convex function. Maximum SLL is minimized over a pre-given scanning range. This first step finds the optimal element locations that would match the expected performance of the array.

Once the element locations have been computed, the second algorithm computes an efficient clustering of the elements and finds out which is the maximum line length (or maximum loss) from IC to the antenna element. Each beamforming (BF) IC can handle 4 RF input/output dual-polarized channels, so the antenna elements are clustered in groups of 4 elements using k-means clustering with equal size [28]. It should be noticed that only one polarization is simulated, although an extra 1.2 mm is assumed in the IC pin to be able to route both lines of vertical and horizontal polarization preserving the minimum distance from the design rules and avoiding crosstalk between them. Finally, an extra 1 mm is taken due to the distance from the center to the feeding point of the circular patch.

With these routing constraints, the algorithm identifies the chip position, the pair-

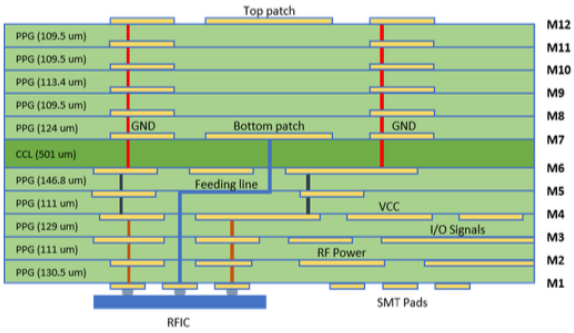

Figure 2.2: 12-layer (M1-M12) substrate Astra MT77.

ing between elements and pins, and the optimal IC location that minimizes the loss cost function. The resulting configuration is then used as the foundation for chip placement and feeding network design. The clustering algorithm is run 50 times, and the configuration that yields the shortest maximum line length is ultimately chosen.

BOARD STACK-UP

The board stack-up consists of 12 layers, as shown in Fig. 2.2. Astra MT77, with a dielectric constant of 3 for the core substrate and 2.95 for the pre-preg, is used as the dielectric material for the printed circuit board (PCB). The upper layers are dedicated to the antennas and are separated from the rest of the subsystems by layer M6, which includes the ground plane for the antenna array and ensures its independent design. The layers beneath M6 contain the routing for the feeding network, control signals, and the analog beamforming ICs at the bottom.

BEAMFORMING IC

The MMW9014K 24.25-27.5 GHz 4-channel dual-polarized ICs [42] have transmit (TX) and receive (RX) integrating a buffer, a phase shifter and a variable gain amplifier (VGA), with 8-bit phase and gain resolution.

ANTENNA UNIT

The antenna element is a circular pin-fed stacked patch [28] as in the square-grid benchmark array with $0.5\lambda_0$ inter-element spacing, where λ_0 is the free-space wavelength at the center frequency f_0 of 26 GHz. Adopted from [42], a circular fence is used for isolation. A 64-element aperiodic array is synthesized by following the convex optimization algorithm proposed for minimization of side lobes (without mutual coupling considerations) [38]. The aperture size in the benchmark array in Fig. A.5 is $3.5\lambda_0$ by $3.5\lambda_0$, while the proposed aperiodic one has an aperture of $4.3\lambda_0$ by $5\lambda_0$ due to sparsity on array edges.

IC TO ANTENNA FEEDING NETWORK

The ICs are distributed on M1 by following the k-means clustering algorithm [41], with several manual iterations for feasibility. The transmission lines in the feeding network

are designed to be similar to those in the reference array. On layer M5, a stripline is used to connect the IC RF pins with the corresponding feeding points of each patch. The stripline on layer M5 is surrounded by a ground on the same layer, and vias are used to connect to the upper and lower layers (M6 and M4) to prevent cross-talk with the striplines nearby. Additionally, a ground on layer M6 covers the entire stripline area to ensure isolation and proper grounding.

RF SIGNAL DISTRIBUTION NETWORK

To distribute the RF signal from external connectors to the beamforming ICs, Wilkinson power dividers are used, ensuring high isolation among the ports while splitting the signal. Microstrip lines on M1 are primarily used for Vertical polarization (V-pol.), and striplines on M2 are used for most of the Horizontal polarization (H-pol.). A combination of the two transmission line structures allow for signal crossing when necessary and provide improved signal isolation. Since the lines for each IC channel have different lengths, calibration of the ICs will be necessary. However, by using the same number of Wilkinson splitters for each signal path and by adding meander lines to lengthen some short lines, the dynamic range of the amplitude calibration has been minimized.

2.1.2. CONTROL SIGNALS

The adaptive beamforming is set up using the beamformer IC gain and phase settings, which can be controlled through the Serial Peripheral Interface (SPI) through Low-Voltage Differential Signaling (LVDS) for fast communication. The ICs are divided into two groups of eight, each controlled by a Field-Programmable Gate Array (FPGA). The pins of an IC, the clock and data input and output signal connections, the chip select and the signals to determine the RF function of each channel are provided in [28]. The control lines are routed on layers M3 (mostly) and M2. The FPGA is located on the right side of the panel where all lines are routed.

2.1.3. SUPPLY NETWORK

The supply network is mostly on M4 and connected to the ICs through the copper areas on M3. To avoid undesired capacitance from narrow lines, the copper layers are placed widely. The network is divided into 8 sections to reduce the noise. Each section feeds 4 ICs from 1 DC connector. The supplied voltage is kept within the upper and lower limits set on the ICs specifications, i.e. a maximum of 20 mV drop [28].

2.1.4. PANEL DESIGN

Complementary to the previous discussions, the 12 layers in the design are provided in Fig. 2.3. The two RF connectors are placed on the sides of the panel. The DC connectors for the supply are located on the corners, near the decoupling capacitors. Also, microFarad (around the array area) and nanoFarad (near the chips) capacitors are placed for docupling. The mechanics in the panel design (front casing, top frame, main PCB, bottom frame, FPGA board and heatsinks, interposers, stand and fan) are similar to the one in the reference array [42]. The top frame, main PCB and its interposer, bottom frame and thermal interfacing are updated to comply with the new dimensions.

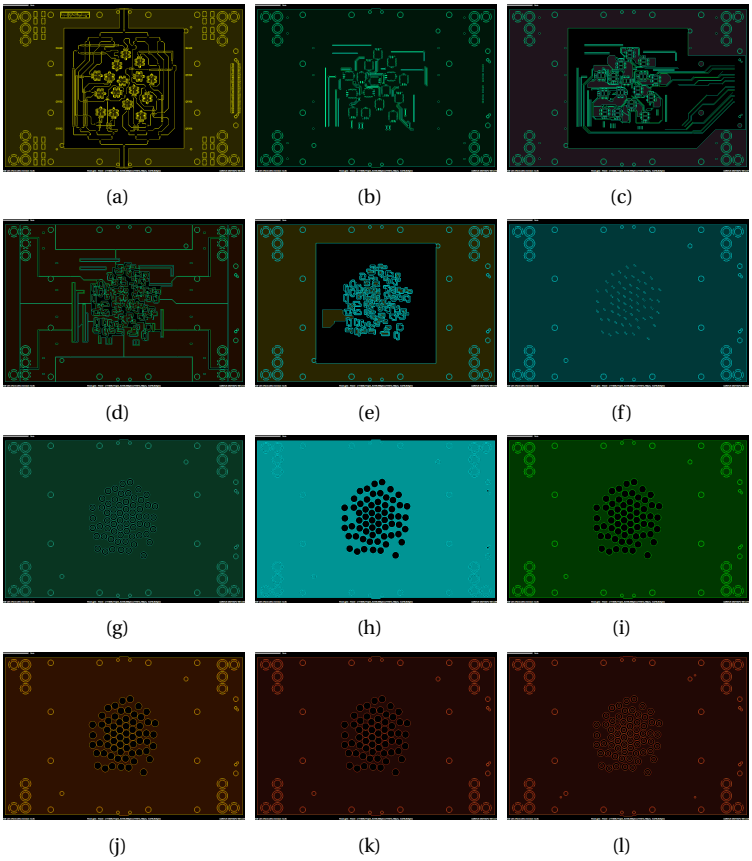

Figure 2.3: Layer by layer panel view [28]: (a) M1, (b) M2, (c) M3, (d) M4, (e) M5, (f) M6, (g) M7, (h) M8, (i) M9, (j) M10, (k) M11, (l) M12.

2.1.5. CALIBRATION

The measurements are conducted in the Delft University Chamber for Antenna Tests (DUCAT). Microwave Vision Group Open-Ended Waveguide (MVG OEW) 2200 is used as a near-field probe for IC-integrated embedded antenna response characterization in the Tx mode, based on the transmission coefficients (S_{21}) between the RF inputs and the probe. Due to the differences in line lengths from the RF inputs to the antenna element ports, load pull effects, temperature variations across the array and IC fabrication tolerances, the complex S_{21} responses for different gain-phase settings of the ICs vary for each channel. Here, the heuristic calibration method is used for H- and V-pol. activation separately at 26 GHz, which is explained in Appendix A.2 in detail, and briefly described in the following steps:

- The probe is accurately positioned in front of each antenna element.
- $|S_{21}|$'s are measured sequentially for the same IC phase setting (equal to 0 in our

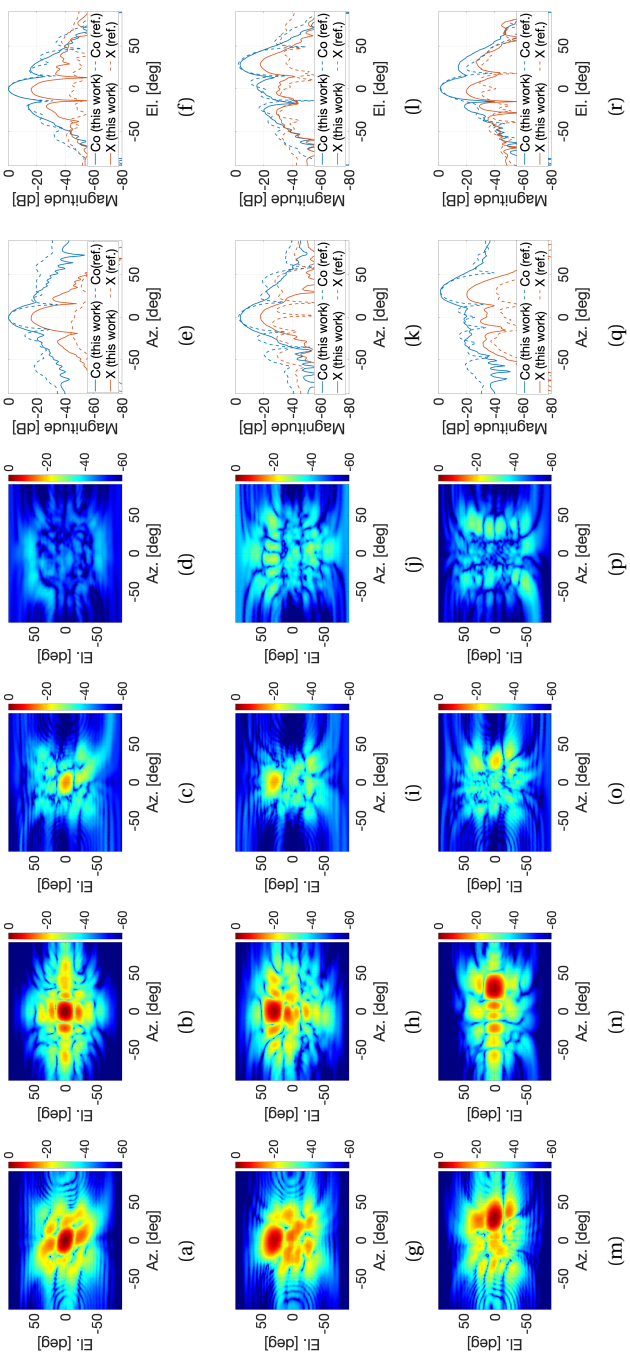

Figure 2.4: Radiation patterns at 26 GHz in H-pol. mode: (a) [0 0] deg. scan, co-pol., this work, (b) [0 0] deg. scan, co-pol., ref., (c) [0 0] deg. scan, x-pol., this work, (d) [0 0] deg. scan, x-pol., ref., (e) [0 0] deg. scan, 0 deg. elevation, (f) [0 0] deg. scan, 0 deg. azimuth, (g) [0 30] deg. scan, co-pol., this work, (h) [0 30] deg. scan, co-pol., ref., (i) [0 30] deg. scan, x-pol., this work, (j) [0 30] deg. scan, x-pol., ref., (k) [0 30] deg. scan, 30 deg. elevation, (l) [0 30] deg. scan, 0 deg. azimuth, (m) [30 0] deg. scan, co-pol., this work, (n) [30 0] deg. scan, co-pol., ref., (o) [30 0] deg. scan, x-pol., this work, (p) [30 0] deg. scan, x-pol., ref., (q) [30 0] deg. scan, 0 deg. elevation, (r) [30 0] deg. scan, 30 deg. azimuth.

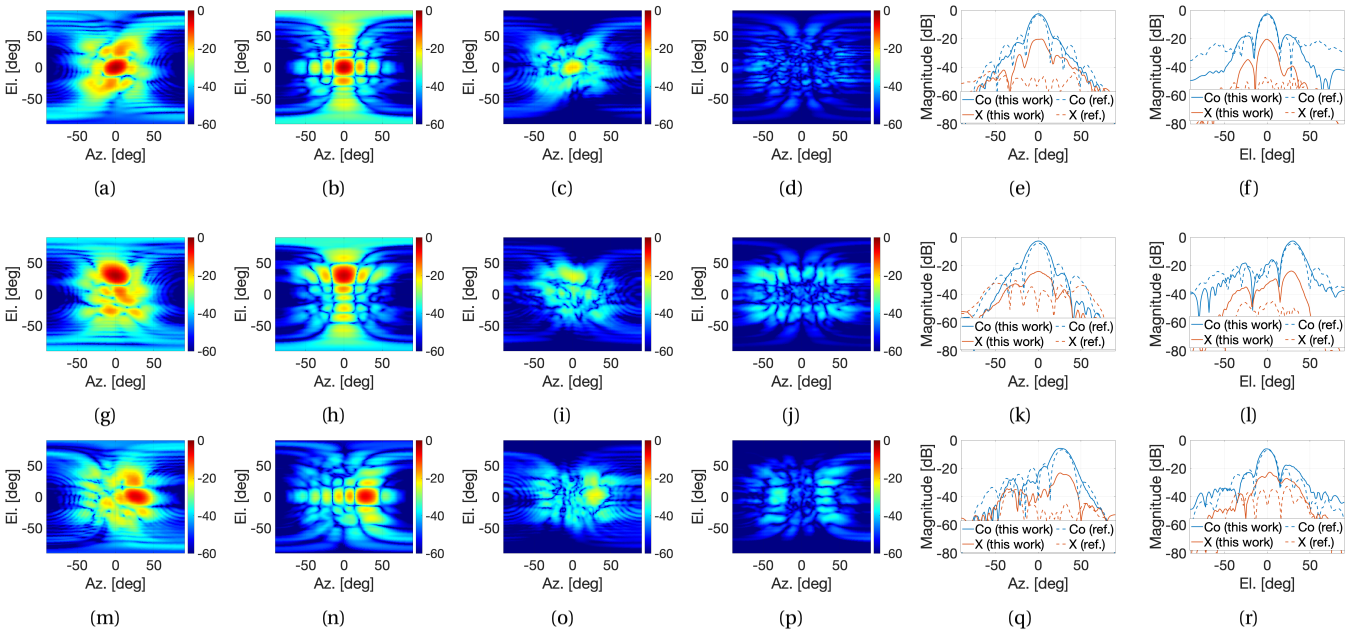

Figure 2.5: Radiation patterns at 26 GHz in V-pol. mode: (a) [0 0] deg. scan, co-pol., this work, (b) [0 0] deg. scan, co-pol., ref., (c) [0 0] deg. scan, x-pol., this work, (d) [0 0] deg. scan, x-pol., ref., (e) [0 0] deg. scan, 0 deg. elevation, (f) [0 0] deg. scan, 0 deg. azimuth, (g) [0 30] deg. scan, co-pol., this work, (h) [0 30] deg. scan, co-pol., ref., (i) [0 30] deg. scan, x-pol., this work, (j) [0 30] deg. scan, x-pol., ref., (k) [0 30] deg. scan, 30 deg. elevation, (l) [0 30] deg. scan, 0 deg. azimuth, (m) [30 0] deg. scan, co-pol., this work, (n) [30 0] deg. scan, co-pol., ref., (o) [30 0] deg. scan, x-pol., this work, (p) [30 0] deg. scan, x-pol., ref., (q) [30 0] deg. scan, 0 deg. elevation, (r) [30 0] deg. scan, 30 deg. azimuth.

Table 2.1: Radiation pattern performance of the aperiodic array in this work as compared to the referenced regular array.

	H-pol.								V-pol.							
Scan angle [deg-az. deg-el.]	**[0 0]**		**[0 30]**		**[30 0]**		**[30 30]**		**[0 0]**		**[0 30]**		**[30 0]**		**[30 30]**	
Cut-plane	**El.**	**Az.**	**El.**	**Az.**	**El.**	**Az.**	**El.**	**Az.**	**El.**	**Az.**	**El.**	**Az.**	**El.**	**Az.**	**El.**	**Az.**
Gain [dB]	/	/	-1.2	-1.2	+0.2	+0.2	-1	-1.5	+0.8	+0.8	+1.5	+1.5	+1	+1	+0.7	+0.8
HPBW [deg]	+3	n.c.	+4	n.c.	+4	n.c.	n.c.	n.c.	+3	n.c.	+4	n.c.	+4	n.c.	-1.5	-2
PSLL [dB]	-6	-1.2	-5.8	-3.3	-4.3	+6	-6.5	-4.3	-1.5	-2.2	-5.5	-1.5	-1	+3.8	-3.3	+2

Notes: The gain of each array is normalized with respect to its maximum at broadside. That is why the "/" sign is used for the gain at [0 0] degree scan in H-pol. mode. The "+" and "−" signs indicate increase and decrease, respectively. The abbreviation "n.c." denotes no change.

case) at each element for varied IC gain settings from the maximal to the minimal.

- New gain settings are calculated at each element to remove the $|S_{21}|$ discrepancies. The highest gain is given to the element with the largest feed line loss, which is nearly 20 dB higher than the loss in the reference array. This is done to achieve (nearly) uniform amplitudes to keep the work focus on the comparison of array layouts. It is worth noting that decreasing RF signal distribution losses in the aperiodic layout via connector type and location optimization remains as future work.
- The phases of the transmission coefficients, after the amplitude correction, are measured one by one.
- The required linear phases for a given scan angle are determined based on the known element locations, and new phase settings are set by assuming a 1.4-degree linear step size in the IC phase shifter settings.
- The IC settings are manually adjusted further for certain elements to achieve uniform amplitudes and linear phases as much as possible. The variations remain within ±0.3 dB and ±1 degree in all measurements as in the benchmark [43], which ensures a fair comparison.

2.2. PATTERN MEASUREMENT RESULTS

The radiation patterns of the proposed aperiodic array, with comparisons to the calibrated reference array results [43], are provided in Fig. 2.4 and Fig. 2.5 for H-pol. and V-pol. activation, respectively. 3 scan angles are considered: [0 0], [0 30], [30 0] degrees in the [azimuth (az.), elevation (el.)] representation. The results (including [30 30] degree scan) are summarized in Table 2.1 by considering the pattern performance (i.e. gain including the active components, half-power-beam-width (HPBW) and peak-side-lobe-level (PSLL)) at the two pattern cuts along the elevation and azimuthal planes. Based on these results, we can infer that:

- The PSLL is, in general, significantly (by up to 6.5 dB) lower in the aperiodic array, except for a few cases such as azimuthal cut-plane for [30 0] degree scan. The differences in different polarization modes and cut-planes originate from the varying mutual coupling.

- The HPBW is, in general, similar in the two arrays, except for the slight increase (by up to 4 degrees) in the azimuthal cut-plane of the aperiodic array patterns.
- For the aperiodic array, the scan loss is improved (by 1 dB on average) in the V-pol. case, while it is worse (by 0.75 dB on average) in the H-pol. mode.
- Due to the asymmetry in the feeding network, the cross-polarization (x-pol.) levels are significantly higher in the aperiodic array (except for the diagonal scanning).

2.3. CONCLUSION

The chapter introduced a novel aperiodic-layout IC-integrated dual-polarized phased array system prototype, experimentally verified and designed to address the previously unexplored practical challenges of implementing non-uniform array layouts using existing components from a regular reference array. It explored the mathematical modeling and optimization of aperiodic phased array topologies, noting that while these methods yield strong numerical results, practical implementation is hindered by routing complexity and calibration challenges due to irregular layouts.

While this chapter and Section 1.1 outline a wide range of challenges associated with aperiodic phased arrays, the thesis specifically addresses those related to the modeling and prediction of MC effects using data-driven methods. Chapters 3 through 5 develop novel EEP prediction methods, including NN models, basis function representations, and ensemble learning techniques, to enable more accurate and efficient design processes. Chapter 6 then applies these tools to real-world design and diagnostic scenarios, such as MIMO radar synthesis and fault detection. Other system-level challenges, though acknowledged, fall outside the scope of this thesis and will be briefly discussed as part of the future directions in the final chapter.

3

ML-Based Embedded Element Pattern (EEP) Prediction and Challenges

A neural network (NN)-based method is proposed to predict embedded element patterns (EEPs) across the entire visible space for non-uniform planar arrays. A cascaded model combining a fully connected network and a sub-pixel convolutional network (ESPCN) enables efficient, high-resolution pattern prediction with significantly reduced computational cost. Initial validation is performed using dipole elements, followed by extension to realistic patch antennas. The impact of training dataset size on prediction accuracy is examined, highlighting the need for alternative methodologies that can reduce the dimensionality of the problem and improve generalization.

Parts of this chapter have been published in:

N. B. Onat, I. Roldan, F. Fioranelli, A. Yarovoy and Y. Aslan, "Efficient Embedded Element Pattern Prediction via Machine Learning: A Case Study with Planar Non-Uniform Sub-Arrays," 2023 17th European Conference on Antennas and Propagation (EuCAP), Florence, Italy, 2023, pp. 1-5.

N.B. Onat, I. Roldan, F. Fioranelli, A. Yarovoy, Y. Aslan, "Dataset Dependency of Data-Driven ML Techniques in Pattern Prediction Under Mutual Coupling", 2024 4th URSI Atlantic Radio Science Meeting (AT-RASC), pp.1-4, 2024.

3.1. EFFICIENT EEP PREDICTION: A CASE STUDY WITH DIPOLES

3.1.1. INTRODUCTION

Many studies proposed powerful synthesis techniques for non-uniformly spaced arrays, however, one crucial challenge, the mutual coupling (MC) effect, was often neglected or has not been efficiently implemented in the synthesis process due to its highly complex nature [44]. The MC causes significant variations in the embedded element patterns (EEPs) and often degrades the performance of the array pattern. In commonly used iterative synthesis algorithms [5, 45], the obtained EEP for a single element differs in each iteration due to element position change, yielding different interactions between the neighboring elements. This currently makes the reliability of the outcome of the proposed layout optimization techniques questionable.

Various techniques have been proposed to include the MC effects in the synthesis of the non-uniformly spaced arrays, such as infinite-to-finite array approach [46], spherical wave expansion [47–49], impedance matrix analysis [50] and the virtual active element pattern expansion method [51]. However, most of the mentioned studies are valid for a particular type of antenna element, computationally expensive, or do not allow sufficient flexibility in array geometries.

Another and more straightforward methodology is to perform full-wave simulations during the synthesis to obtain EEPs at each design iteration. Although proven to be effective [52, 53], these techniques increase the computation time and load, which prevent the designers from (i) synthesizing large arrays, (ii) testing different what-if scenarios efficiently for different input parameter selections, (iii) having a large number of optimized array topologies, and (iv) achieving fast adaptive layout modulation when applicable.

Machine learning (ML) techniques have recently drawn attention due to their potential for efficiently solving non-linear complex problems with remarkable time and accuracy. Specifically, neural networks (NNs) were efficiently used in solving electromagnetics (EM) problems due to their ability to approximate the highly non-linear input-output mappings. Therefore, ML techniques have been exploited in some studies for realistic array pattern estimation and synthesis [22, 23], or to predict EEPs to include MC effects in the synthesis. For the latter, in [24] the author presents an efficient model to achieve accurate MC prediction by building a virtual active element model using Gaussian process regression (GPR). Another recent study aims to include the MC effects in nonuniform linear array synthesis by building a surrogate model for the EEPs using a multi-layer perceptron neural network (MLPNN) [54]. Although the mentioned studies illustrated the potential of ML in linear non-uniformly spaced arrays, to the best of our knowledge, none of the studies in the literature focus on predicting EEPs in the whole visible space (e.g., in theta-phi, θ, ϕ plane) for a flexible planar irregular array topology.

To fill the mentioned gap in the literature, a novel NN-based methodology is introduced to predict the EEPs on the θ, ϕ plane in the far-field for a planar non-uniform array. A 4-element planar non-uniformly spaced sub-array topology with adjustable element positions is used to test the proposed approach. In our original implementation, simple dipole antennas are initially used to rapidly generate training data and demonstrate the feasibility of the concept before transitioning to more realistic patch antenna models in later chapters. Two neural networks are cascaded in the proposed method: first, a fully connected neural network is trained to predict low-resolution EEPs, followed by

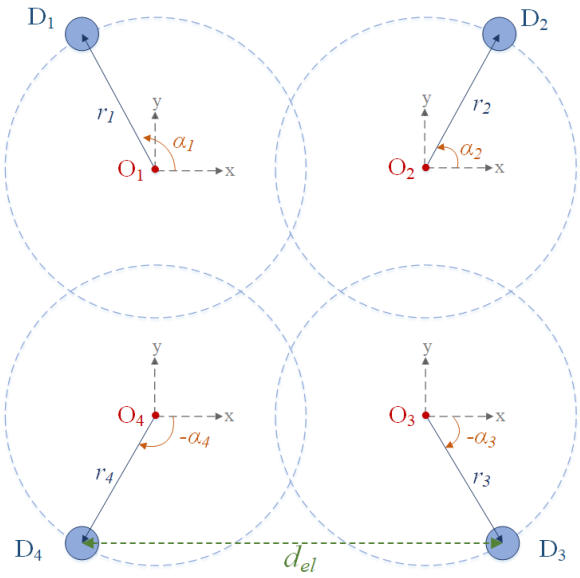

Figure 3.1: Irregular sub-array structure for $N = 4$ as designed in Appendix A.1.

the application of an efficient sub-pixel convolutional neural network (ESPCN) [55] to upscale the results to the desired high resolution. The trained model is planned to be integrated into an optimizer to significantly decrease the computational time and load by efficiently providing the EEPs for the desired sub-array configuration during the optimization process.

3.1.2. PROBLEM FORMULATION

The far-field equation for an N-element rectangular array can be formulated as:

$$F(\theta,\phi) = \sum_{n=1}^{N} E_n(\theta,\phi) e^{jk(x_n \sin\theta\cos\phi + y_n \sin\theta\sin\phi)} \tag{3.1}$$

where $E_n(\theta,\phi)$ is the EEP of the n-th element, $k = 2\pi/\lambda$ where λ is the wavelength at the operating frequency, x_n and y_n indicates the position of the elements in x and y coordinates, respectively. During an aperiodic array optimization, the EEPs become quite important due to the change in element positions. The ultimate aim of this study is to accurately estimate the EEP for any given element position, $\hat{E}_n(\theta,\phi)$, which is as close as possible to the full-wave simulated one, $E_n(\theta,\phi)$, in any given array layout with certain constraints (on the maximum aperture size, minimum element spacing, etc.). This problem can be simply formulated by the minimization of the mean squared error (MSE):

$$\rho = \frac{1}{NM} \sum_{n=1}^{N} \sum_{m=1}^{M} \left(|E_n^m(\theta,\phi)| - |\hat{E}_n^m(\theta,\phi)| \right)^2 \tag{3.2}$$

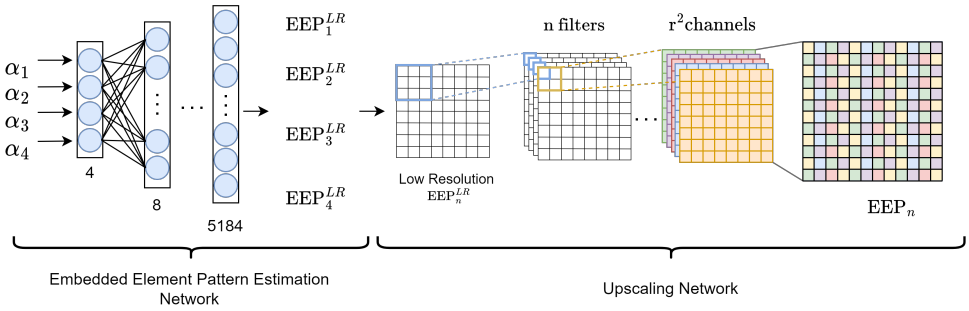

Figure 3.2: Block diagram of the proposed neural network architecture. It comprises two networks: the EEP estimation network and the upscaling network. The first one is a fully connected network, while the second is a convolutional neural network based on the ESPCN architecture.

where ρ is the MSE of the given problem and M is the total number of samples for each pattern. For this minimization problem, a NN framework can efficiently be trained to predict the EEP of an element for a given topology. In this way, the predicted patterns can be provided in real-time with high-precision with a fully-trained network for further use.

In order to realize and test the proposed solution on a small scale, our proposed approach is based on creating an optimized irregularity/sparsity in the array layout, while minimizing the losses and calibration requirements by preserving a circular sub-array arrangement. This concept is implemented using a 4-element planar sub-array architecture, as illustrated in Fig. 3.1 and explained in detail in Appendix A.1. In this figure, D_n for $n = 1, ..., 4$ indicates the array elements. The n-th element can move on the corresponding element circle, which has a fixed origin point O_n and a radius r_n. Furthermore, the element angle, α_n, is defined as the angle between the x-axis and the radius vector, which is the vector from O_n to E_n.

In this study, the radius of the circles is kept equal, and the allowable minimum distance between the elements, d_{el}, is defined to be 0.3λ, introducing more freedom to the elements and stronger coupling, unlike the conventional 0.5λ minimum element distance constraint. To validate the methodology, z-oriented dipole antennas are used as an array element, where the center frequency was chosen as 12 GHz for concept demonstration purposes. However, since all distances and spatial relationships are defined in terms of the wavelength, the absolute frequency does not affect the generality of the methodology. The EEPs for the training of the network are generated with CST Microwave Studio and exported in θ, ϕ plane. Since the proposed methodology requires low- and high-resolution data, as explained in the next section, the exported patterns have sizes of 36×36 and 180×180, respectively.

3.1.3. PROPOSED NN ARCHITECTURE

Neural networks (NNs) have been proven to be universal function approximators [11, 17], given enough layers and sufficient training data. For this reason, a NN is designed

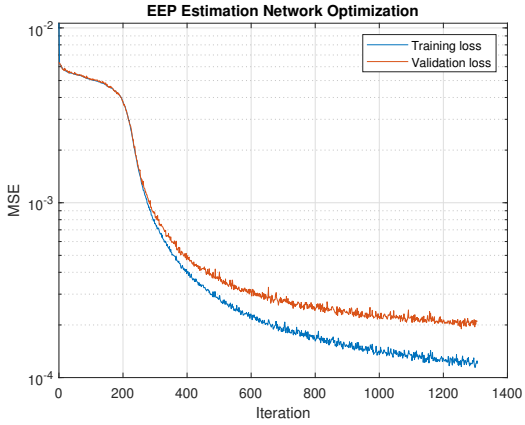

Figure 3.3: Evolution of the training and validation loss for the EEP estimation network. The validation loss converges to a value of $2e-4$.

in this work to estimate the EEP of four elements given the array topology. However, it is essential to note that this estimation will be done inside a large aperiodic array optimization algorithm in the future, and thus, the NN is designed for computational efficiency. Consequently, the size of the networks has been tried to maintain as small as possible.

In this work, the input variables are the four α_n angles, and the goal is to estimate high-resolution EEP (i.e., EEPs discretized every degree) of each element, taking into account the MC effects. Thus, the total number of samples to be estimated is $180 \times 180 \times 4 = 129600$. For this reason, a Feed-Forward NN architecture is unfeasible since it will require an enormous number of parameters to optimize. To overcome this problem, a novel approach that involves the concatenation of two NN is designed, where first low-resolution EEPs are estimated, and then they are upscaled to the desired resolution.

3.1.4. SIMULATION RESULTS AND DISCUSSION

The first NN is a fully connected network that has as input the four α_n and outputs a low-resolution estimation of the absolute value of each EEP, with 36×36 size (linearly down sampled from 180×180). An incremental approach is followed, where the number of layers in each layer is doubled until it reaches 5184 ($36 \times 36 \times 4$), corresponding to the dimension of the four EEPs. Therefore, the first NN consists of 12 layers, the first 11 with a hyperbolic tangent activation function and the last with a linear activation function. Then, once the first network is trained and can accurately estimate low-resolution EEPs, a second network is designed to upscale them to a higher resolution. With an efficient implementation in mind, the ESPCN network is used [55], which provides good upscaling performance while maintaining a simple architecture. This network uses two convolutional layers for feature map extraction and a sub-pixel convolution layer that aggregates the feature maps from the low-resolution space and builds the high-resolution image. In this work, the two hidden convolutional layers have n=32 filters and 3×3 kernel size, while the sub-pixel layer has r^2=25 filters to achieve five times the input resolution

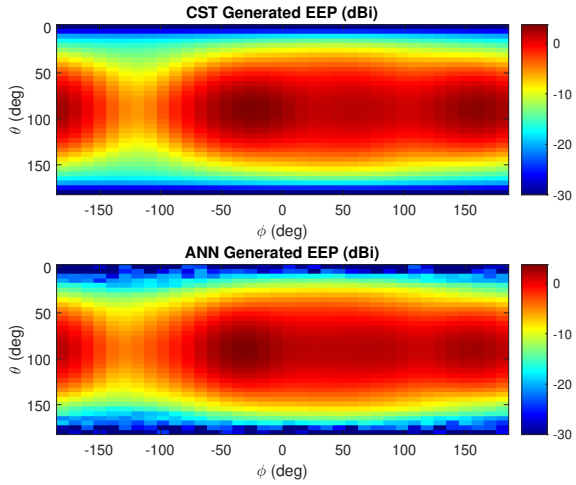

Figure 3.4: On the top plot an example of a low-resolution EEP (realized gain in [dB]) generated with CST. In the lower figure, the EEP predicted with the NN for the same array with the proposed NN for the same array topology shows very good agreement.

(upscaling from 36×36 to 180×180). A diagram of these two networks can be seen in Fig. 3.2.

In total, 9000 random sub-array topology simulations were run for the low-resolution dataset by taking into account the minimum element spacing criterion, and 3000 simulations were run for the high-resolution dataset. After each simulation, the EEPs are exported and post-processed with MATLAB to obtain the desired input (in terms of α angles) for the proposed NN models.

As explained in the previous section, the two networks are trained independently, but both use ADAM optimizer with the default hyperparameters (η=0.001, β_1=0.9, β_2=0.999, ϵ=1e-7) and the MSE metric as loss function. The 9000 4-tuple EEPs generated with CST are used as labels using 90% of them for training the networks and 10% for validation. First, the EEP estimation network is trained, and the evolution of the MSE over iterations can be seen in Fig. 3.3. As expected, the training loss is lower than the validation loss but still converges to a very low value of around $2e-4$. As an example of the output of the trained network, a low-resolution EEP generated with CST and with the network itself is shown in Fig. 3.4.

Once the first NN is trained, the upscaling network can be concatenated and trained to generate high-resolution EEPs. Fig. 3.6 shows the evolution of the pixel-wise MSE, and it can be seen how it converges again to a value close to $2.1e-4$. Moreover, now that both networks are trained, the four high-resolution EEPs can be estimated given the four angles. Fig. 3.5 shows one estimation example for a $\alpha_1 = 170$, $\alpha_2 = 65$, $\alpha_3 = 175$ and $\alpha_4 = 150$, for the CST-generated EEPs and for the NN-based proposed method. It is important to highlight that the NN estimation took only 0.15ms, while the computation with CST took 240s.

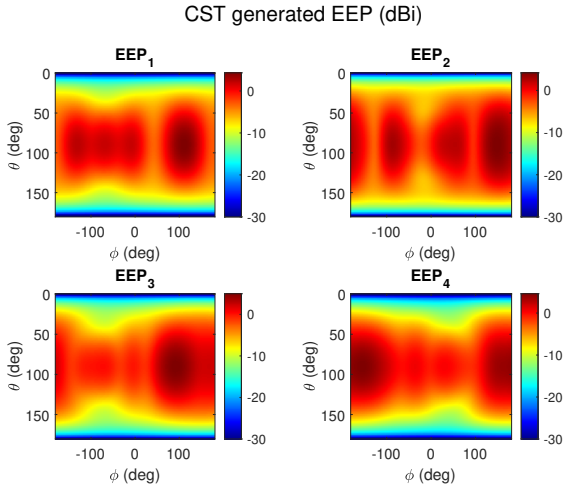

(a)

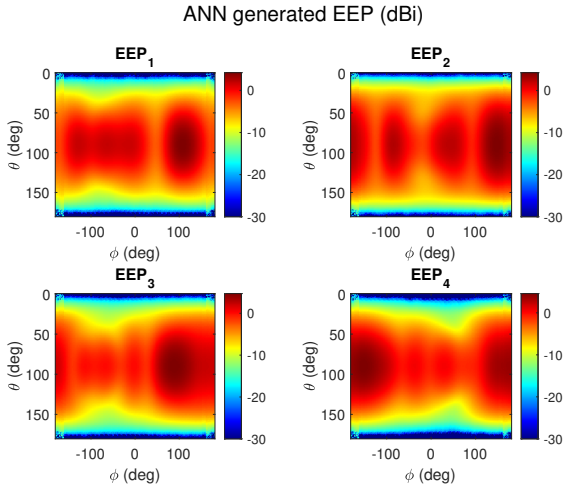

(b)

Figure 3.5: One example of EEP prediction for a realization where the elements are at 170°, 65°, 175°, and 150°. In (a), the EEPs were computed with CST, and in (b), the EEPs were computed with the trained neural network.

Finally, it is important to quantify the prediction error, beyond the good visual agreement of Fig. 3.5(a). To this end, the mean error in the peak (ϵ_{p}) between the CST-generated EEPs and the NN-generated EEPs is computed over all the validation tests as:

$$\epsilon_{\mathrm{p}} = 20\log\left|\sum_{k=1}^{K}\left(\sqrt{|E_k(\theta_{\mathrm{mk}},\phi_{\mathrm{mk}})|}-\sqrt{|\hat{E}_k(\theta_{\mathrm{mk}},\phi_{\mathrm{mk}})|}\right)\right|, \tag{3.3}$$

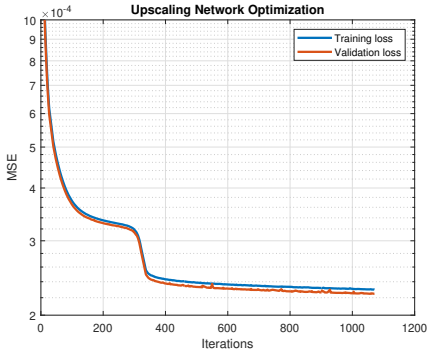

Figure 3.6: Evolution of the training and validation loss for the upscaling network. The validation loss converges to a value of $2.1e-4$.

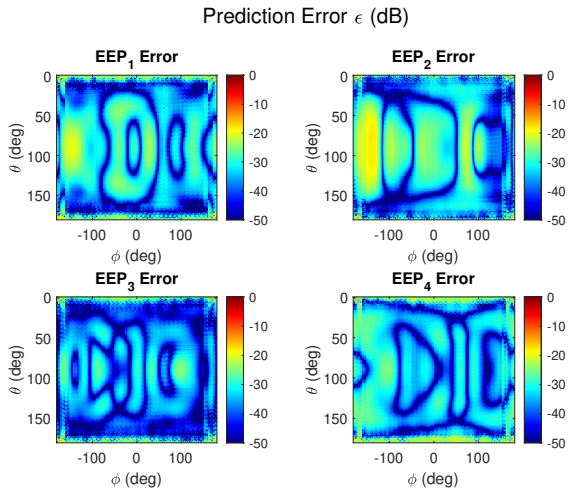

Figure 3.7: Point-wise error for the CST and NN generated EEPs. The elements are at 170°, 65°, 175°, and 150°. The maximum error is -17.88dB

with θ_{mk} and ϕ_{mk} are the angles where the maximum of the EEP for the k-th element is observed. K is the number of realizations (which is the validation set), yielding -39.61 dB mean peak error. Moreover, the point-wise error can be computed as:

$$\epsilon(\theta,\phi) = 20\log\left(\left|\sqrt{E(\theta,\phi)} - \sqrt{\hat{E}(\theta,\phi)}\right|\right). \tag{3.4}$$

As an example, the point-wise error for the same antenna configuration is shown in Fig. 3.7. As can be seen, the error in all the EEPs is very low, with the maximum error for this specific sample being -17.88 dB.

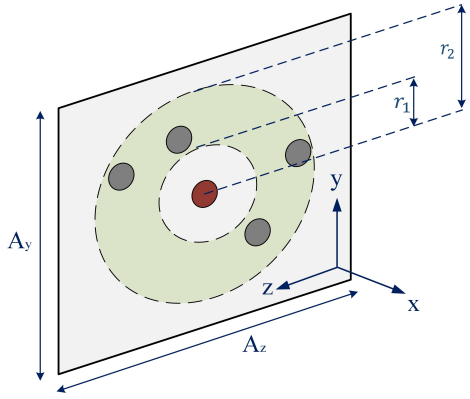

Figure 3.8: $K = 5$-element aperiodic array topology where the AUT, highlighted with the red color, is located at the center, $(y_o, z_o) = (0,0)$, and the neighboring elements (gray colored) are randomly positioned in the defined green region: $r_1^2 \leq (y_i^2 + z_i^2) \leq r_2^2$ where (y_i, z_i) is the location of the i-th neighbor element in λ.

3.1.5. CONCLUSION

An NN-based methodology has been applied to predict the EEPs of the antenna elements in the whole visible space for a semi-flexible non-uniform array topology. A fully-connected and the ESPCN networks have been concatenated in order to achieve high-resolution in the predicted EEPs. The error always remains below -18 dB, which is observed in the low-gain regions, while it is below -30 dB when the gain is relatively high.

3.2. IMPACT OF DATASET DEPENDENCY IN DATA-DRIVEN ML TECHNIQUES FOR EEP PREDICTION ON PATCH ARRAY APPLICATION

3.2.1. INTRODUCTION

Although ML-based studies are promising for MC and EEP prediction, since the performance of these methodologies highly depends on the training data, it is essential to have a randomly distributed dataset with sufficient data to achieve reliable predictions while avoiding over-fitting. This study investigates how the size of the dataset is crucial for the EEP prediction via NNs. Additionally, the pattern prediction performance variations in the validation set are discussed.

3.2.2. ANTENNA UNDER TEST (AUT)

In this study, a 5-element aperiodic array topology is considered. This comprises of a central element (the pattern of which is to be estimated) located at the origin, $(y_m, z_m) = (0,0)$, and of its neighboring elements which are randomly located with a minimum spacing of $\lambda/2$ in the region of $r_1^2 \leq (y_i^2 + z_i^2) \leq r_2^2$ where (y_i, z_i) is the location of the i-th neighbor element in λ with $i = 1, ..., 4$. Furthermore, r is the radius of the defined circle that is selected as $\lambda/2$. Figure 3.8 illustrates the considered $K = 5$-element array topology (with $K-1$ neighbor elements) where each element is a pin-fed rectangular patch

antenna designed for the operation frequency of 2.85 GHz. It is worth noting that the proposed method can be applied to any operating frequency and element type once the full-wave simulated training data is made available. This frequency is chosen to balance simulation accuracy and computational efficiency during preliminary dataset generation. The designed rectangular patch has a co-polarization electric ($e-$) field component in the θ direction, which will be referred to as the EEP. As e-field simulation in CST takes 1m reference distance for 1W of peak input power, subtracting a magnitude of 14.77 dB from the e-field pattern will result in the realized gain if the conversion is preferred. This applies to all e-field EEP figures throughout the thesis.

3.2.3. PROBLEM FORMULATION AND NN ARCHITECTURE

Following the work in [56], this study focuses on the power pattern prediction where each EEP is a function of θ and ϕ, both having 180 samples, resulting in a 180×180 matrix.

The considered architecture comprises two distinct components: the initial part produces a low-resolution EEP at 36×36, and the subsequent segment scales it up to the desired resolution of 180×180, corresponding to a 1-degree resolution. The upscaling process is implemented using the efficient sub-pixel convolutional neural network (ESPCN) [57] in the upscale block as shown in Fig. 3.10.

Furthermore, the successful estimation of the EEP relies on utilizing the structural similarity index (SSIM) as a loss during the training of the NN. Originally designed as a metric for evaluating image quality in the context of a reference image, typically to gauge losses from image compression, SSIM has more recently found application as a loss function in training neural networks [58].

The effect of the dataset size and performance variation in validation set of the proposed network are discussed in this section. To this extent, 3800 simulations with random topologies were run to generate the training dataset. The validation set of the proposed network remain as the same size as it is used in the the primary (main) training

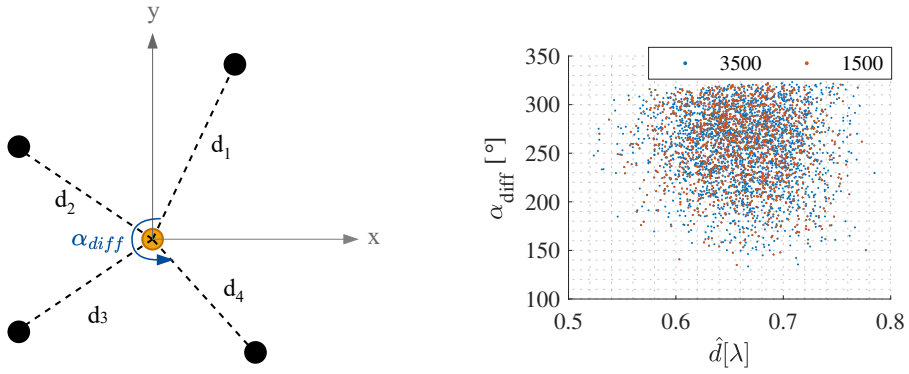

(a) Case topology

(b) Data Distribution

Figure 3.9: Analysis of distribution of the training datasets.

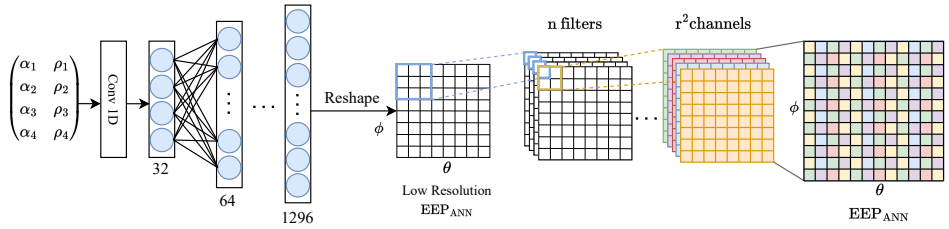

Figure 3.10: Block diagram of the utilized NN architecture comprising two concatenated networks based on the previous section.

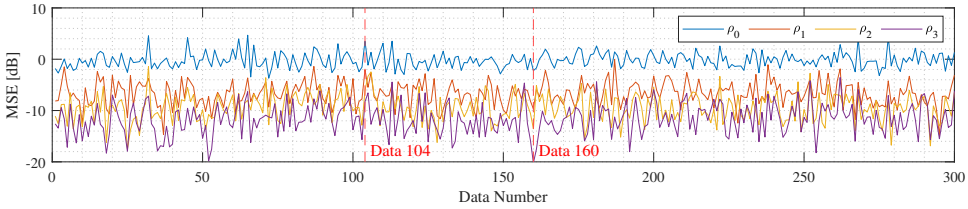

Figure 3.11: MSE results between the full-wave generated EEP of the full validation set and IEP (ρ_0), and predicted EEPs with the dataset sizes of 1500 (ρ_1), 2500 (ρ_2) and 3500 (ρ_3).

Table 3.1: MSE results for the IEP, indicated with the subscript 0, and three different dataset sizes: 1500, 2500 and 3500, indicated with the subscripts 1,2 and 3, respectively.

Topology	ρ_0 **[dB]**	ρ_1 **[dB]**	ρ_2 **[dB]**	ρ_3 **[dB]**
Average	0.3	-6.06	-8.65	-10.67
Data 104	3.5	-2.05	-12.9	-15.67
Data 160	-2.23	-9.7	-13.57	-20.21

dataset comprising 3500 samples, which is then gradually decreased to 2500 and 1500 for the analysis. While the mentioned validation set always remains the same, comprising 300 data points. The designed pin-fed patch antenna's isotropic element pattern (IEP) was simulated and compared as a benchmark. Furthermore, two extreme cases are selected for a detailed analysis.

To visualize the distribution of the datasets, the polar coordinate system is used. The distance d_i for $i = 1,2,3,4$ indicates the distance (in λ) between the main the corresponding neighbor element. The angle α_{diff} is the angle between element pairs having the maximum angle separation as shown in Fig. 3.9(a). The distance $\hat{d}$ shows the mean distance of the neighbor elements to the main element for each topology. Figure 3.9(b) illustrates the distribution of the datasets for the sizes of 1500 and 3500, where the density of the distribution increases as the data size increases. It is important to note that the angle α_{diff} remains larger than 100° due to the defined minimum element spacing of $\lambda/2$.

To quantify the prediction performance, the minimum squared error (MSE) cost func-

tion is utilized:

$$\rho_t = 10\log\left(\frac{1}{N_s^2}\sum_{j,k=1}^{N_s}\left(|E_{\mathrm{CST}}(\theta_j,\phi_k)| - |E_t(\theta_j,\phi_k)|\right)^2\right) \tag{3.5}$$

where N_s is the total number of samples for θ and ϕ, E_{CST} is the full-wave simulated EEP of the central element generated by the commercial software CST, E_{t} is the predicted EEP of the same element where $t = 0,1,2,3$ indicates IEP and the sizes of the dataset 1500, 2500 and 3500, respectively.

The MSE is evaluated over the validation set and shown in Fig. 3.11. The error between E_{CST} and E_{IEP} (ρ_0) remains at the level of 0 dB, reaching up to 5 dB and having an average error of 0.3 dB whereas the error between E_{CST} and the prediction E_1 which is trained with the smallest dataset has an average error of -6 dB as shown in Table 3.1. However, the variation in the error remains high; in other words, the prediction is highly dependent on the provided dataset, where the reliability of the methodology can become questionable.

When the data size is increased to 2500, the average error is reduced by almost 3 dB,

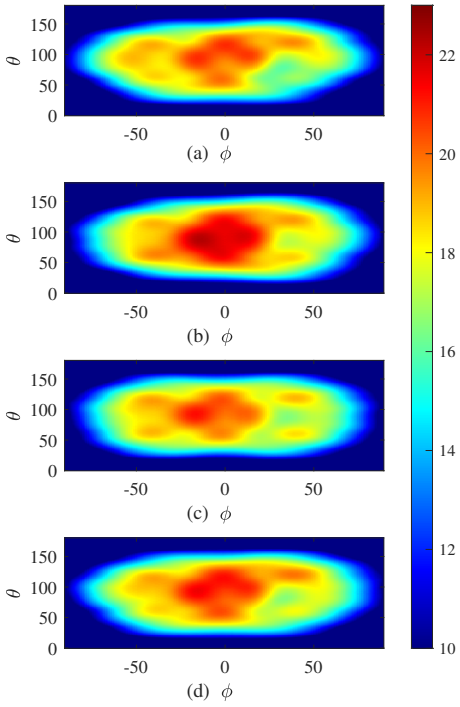

Figure 3.12: EEPs (e-field [dB]) for Data 104 with $(x_i, y_i) = \{(-0.25,-0.45),(0.2,-0.75),(0.5,0.2),(0.5,-0.3)\}\lambda$. (a) Full-wave simulated EEP; (b) Predicted with 1500 data; (c) Predicted with 2500 data; (d) Predicted with 3500 data.

going down to nearly -9 dB. The entire dataset is used in the training, so the error scales down to almost -11 dB. Although the variations can still be observed, these variations can become negligible as the error goes down beyond -10 dB. Data 104 and 160 are analyzed as extreme cases to validate this.

Figure 3.12 illustrates the CST-generated EEP and predicted EEPs for Data 104 which has one of the highest error value as shown in Table 3.1. In this topology, the location of the elements is given as $(x_i, y_i) = \{(-0.25, -0.45), (0.2, -0.75), (0.5, 0.2), (0.5, -0.3)\}$ where the neighbor elements are clustered at the top right corner, creating a special case. When the data size is small, the NN overestimates the peak region with the section where $\theta < 50°$ and $\phi > 0°$, increasing the error rate to -2.05 dB as can be seen in Fig. 3.12(b). The performance of the prediction drastically increases as the data size increases, reducing the error to -15.67 dB.

On the other hand, the trained model achieves one of the best predictions in Data 160 where the elements are located at $(x_i, y_i) = \{(-0.6, -0.2), (0.55, 0.4), (-0.25, 0.65), (-0.05, -0.7)\}$ in λ, having an error of nearly -10 dB with the low-size and -14 dB with the 2500 data as shown in Table 3.1. When the entire dataset is used, the difference between the full-wave generated EEP in Fig. 3.13(a) and predicted EEP in Fig. 3.13(b) becomes almost

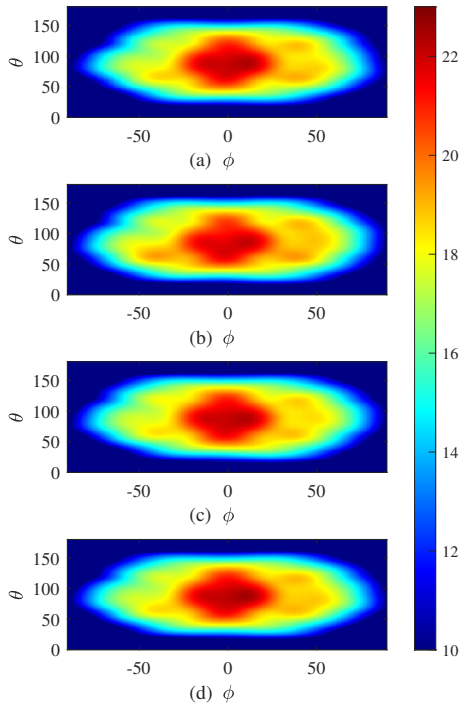

Figure 3.13: EEPs (e-field [dB]) for Data 160 with $(x_i, y_i) = \{(-0.6, -0.2), (0.55, 0.4), (-0.25, 0.65), (-0.05, -0.7)\}\lambda$. (a) Full-wave simulated EEP; (b) Predicted with 1500 data; (c) Predicted with 2500 data; (d) Predicted with 3500 data.

invisible while the error rate decreases below −20 dB.

3.2.4. CONCLUSION

The impact of training data on ML-assisted antenna pattern prediction under mutual coupling is studied. An NN-based methodology has been used to predict the EEP of a central patch antenna element in the close vicinity of randomly distributed patches. Two-stage networks, namely, fully connected and ESPCN, were used to achieve high resolution. It has been shown that the performance of the network is highly dependent on the training data, where the variation of the prediction error in the validation set becomes critical with the excessive reduction in the size of the dataset. Furthermore, with the increase in the number of elements, the disturbance on the EEP by the MC effect can become a more complicated problem, reducing the reliability of the prediction with a small dataset. This highlights the need to develop innovative techniques to maintain sufficient pattern prediction accuracy with a relatively small dataset.

3.3. CONCLUSIONS

This chapter proposed a novel ANN-based method to predict EEPs across the entire visible space (θ, ϕ plane) semi-flexible non-uniformly spaced dipole arrays, then extended for the planar patch arrays, addressing a gap in the literature where prior studies focused mainly on linear arrays or limited visible space. The proposed framework comprised a cascaded neural network (NN) architecture, combining a fully connected neural network for low-resolution EEP prediction with an efficient sub-pixel convolutional neural network (ESPCN) for high-resolution upscaling, enabling significant reductions in computational time and load during array layout optimization.

Furthermore, for the first time, the crucial role of dataset size for embedded element pattern (EEP) prediction via NNs is presented, highlighting how training data quality and size impact prediction reliability and discussing the variations in pattern prediction performance during validation. It was also emphasized that there is a need for new techniques to ensure accurate pattern prediction even with small datasets, as prediction reliability decreases when the dataset size is too small, particularly with a large number of elements and more complex mutual coupling effects.

4

EEP Reconstruction Through Auxiliary Basis Functions

An efficient method is presented to reconstruct embedded element patterns (EEPs) using auxiliary basis functions, enabling fast and accurate modeling of mutual coupling (MC) effects. Two complementary approaches are introduced. First, EEPs are modeled using a constrained array of infinitesimal dipole modeling (IDM) where dipoles are arranged in a sunflower topology, improving numerical stability while avoiding iterative optimization. The influence of dipole type and orientation on prediction accuracy is systematically analyzed. Second, EEPs are represented using spherical harmonic decomposition, providing a compact and interpretable basis that captures far-field variations with reduced complexity. Both methods demonstrate reliable EEP reconstruction and are suitable for machine learning (ML) tasks where reduced dimensionality and physical interpretability are essential.

Parts of this chapter have been published in:

N. B. Onat, A. Yarovoy and Y. Aslan, "Sunflower Array of Infinitesimal Dipoles for Constrained Antenna Modeling," 2024 18th European Conference on Antennas and Propagation (EuCAP), Glasgow, United Kingdom, 2024, pp. 1-5.

T. Dash, **N. B. Onat**, Y. Aslan and A. Yarovoy, "Embedded Element Pattern Reconstruction Using Spherical Harmonics to Model Mutual Coupling," International Conference on Electromagnetics in Advanced Applications (ICEAA), Palermo, Italy, 2025, accepted.

4.1. CONSTRAINED INFINITELY SMALL DIPOLE MODELING

4.1.1. INTRODUCTION

Infinitesimal dipole modeling (IDM) is a well-developed technique in formulating the fields generated by an arbitrary antenna [59]. It has been used in various applications including electromagnetic emission and interference characterization in printed circuit boards [60, 61], antenna diagnostics [62], self and mutual admittance computation in arrays [63], source identification and pattern prediction in near- and far-field [64].

In IDM, the actual antenna volume is replaced by an array of (both electric, $e-$ and magnetic, $m-$type) infinitesimal dipoles (IDs), the locations, orientations and moments (complex excitations) of which are to be determined [65]. In general, metaheuristic optimization algorithms, such as Genetic Algorithm [65, 66], Invasive Weed Optimization [63] and Differential Evolution [60], are used to find out the parameter values that minimize the difference between the fields of the actual antenna and the fields predicted by the IDM. Such techniques suffer from long computation time and high complexity in the case of characterization of large antennas [67], or when dynamic modeling is needed for a large amount of training dataset [61].

Constrained IDM was introduced to improve the algorithm's efficiency. In [68], it was shown that for planar antenna geometries, dipoles distributed only on the main radiation surface provide accurate fields. In [69], dipoles with fixed positions (on a Cartesian grid) and orientations were used. In [63], only e-type dipoles were considered in IDM, while in [60], only m-type dipoles were employed. Using a single type (e or m) of dipole and single orientation (x, y, or z) reduces the degrees-of-freedom solely to the dipole moments. In that case, the excitation of each dipole can be efficiently determined by solving a set of linear equations [62, 68]. However, due to the inversion of a Vandermonde-type matrix [70] with a high condition number, the number and topology of the dipoles become critical [71]. For performance stability of IDM against noise, both the condition number and errors in the estimated fields should be kept low. Towards the aim of creating irregularity in the array topology and reducing the number of dipoles, an iterative convex optimization algorithm was implemented in [67]. However, this algorithm brings additional computational complexity and results in a customized array topology for the device under test.

In this chapter, we propose, for the first time, to apply the sunflower array topology concept (studied in [72, 73] for grating lobe suppression) in constrained IDM to eliminate the use of optimizers (in minimizing the pattern error and the number of dipoles) for the best computational efficiency in a reasonable accuracy. We also present a novel discussion, driven by mathematical and physical insights, on the impact of the selected (common) type and orientation of the dipoles on the predicted patterns.

4.1.2. ANTENNA UNDER TEST (AUT)

For this work, before application to ML and aperiodic arrays in Chapter 5, a planar array with equally spaced 5 by 5 pin-fed rectangular patch antennas is designed as illustrated in Fig. 4.1. The center and corner elements, highlighted in yellow, are selected to demonstrate the performance of the proposed approach at the embedded pattern level. The application of the proposed IDM on the total array pattern on broadside is also studied.

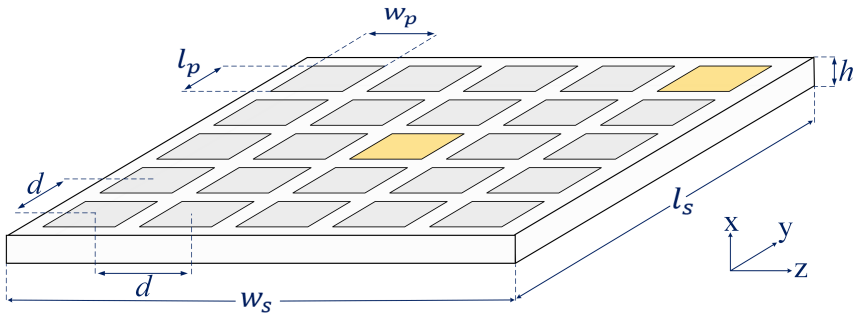

Figure 4.1: 5-by-5 planar array of pin-fed rectangular patch antennas as AUT. Selected elements are indicated in yellow.

Table 4.1: Values of array design parameters

Center frequency	2.85 GHz	**Substrate length** (l_s)	360 mm
Patch length (l_p)	33.71 mm	**Substrate width** (w_s)	360 mm
Patch width (w_p)	33.71 mm	**Substrate height** (h)	1.6 mm
Spacing (d)	0.5λ	**Relative Permittivity** (ϵ_r)	2.2

The design parameters of the array can be found in Table 4.1.

IMPLEMENTATION OF CONSTRAINED IDM

Although each $e-$ and $m-$dipole in the ID array contributes to achieving the desired radiated field, only $y-$ and $z-$oriented IDs are essential in the constrained IDM [68] since the AUT is placed on the $y-z$ plane as shown in Fig. 4.1. Table 4.2 summarizes the far-field expression of the IDs depending on the dipole type, orientation and polarization. In Table 4.2, I_y^e, I_z^e, I_y^m and I_z^m, are the dipole currents, θ and ϕ are the spherical angles, η is the free space impedance. For the n-th ID, $C_n(\theta,\phi)$ is formulated as:

$$C_n(\theta,\phi) = \mathrm{j}wl_0\frac{\mu}{4\pi r}\mathrm{e}^{-\mathrm{j}kr}\mathrm{e}^{\mathrm{j}k(\sin\theta\sin\phi y_n+\cos\theta z_n)} \tag{4.1}$$

which is a common multiplication factor for different orientations and polarizations of the ID with a length of l_0 at a far distance of r from its location (y_n, z_n). The formulation in (4.1) can be represented in a matrix form depending on the sampling of θ and ϕ. In this work, this matrix is converted into a vectorial form by concatenating its columns to fit into the problem formulation.

Since the co-polarization component of the AUT is along the ϕ direction, the $z-$ oriented $e-$dipole has no contribution. In this way, the total number of contributing components reduces from four to three. This study focuses on each dipole type and orientation to analyze the prediction performances from a mathematical perspective. From a physical perspective, as the radiation of each patch antenna element of the AUT can be approximated by two magnetic dipoles along the z-axis (on the radiating edges of the patch), working with the $z-$oriented $m-$dipoles becomes more meaningful.

In formulating the constrained IDM problem, the dipole currents are the complex coefficients to be determined in order to obtain the actual radiation pattern with low errors and high stability against noise. Towards this aim, the problem can fundamentally be described as:

$$\mathbf{Ax} = \mathbf{q} \tag{4.2}$$

where $\mathbf{q}$ is the electric far-field of the considered element or array (in the column vector form), $\mathbf{x}$ is a column vector that comprises the set of IDs coefficients, $\mathbf{A}$ is a matrix that describes the total electric field of an array of infinitesimal dipoles and can be expressed as:

$$\mathbf{A}_p^t = \mathbf{F}_p^t(\theta,\phi) \cdot \left[\langle \mathbf{C}_1(\theta,\phi) \rangle \quad \dots \quad \langle \mathbf{C}_N(\theta,\phi) \rangle \right] \tag{4.3}$$

where $\langle \mathbf{C}_n(\theta,\phi) \rangle$ represents the vectorial form of (4.1) obtained by concatenating its columns, $\mathbf{F}_p^t(\theta,\phi)$ is the multiplier of the $p-$oriented (i.e., $y-$ or $z-$) and $t-$type (i.e., $m-$ or $e-$) ID (see Table 4.2), and N is the total number IDs in the array. It is important to note that the polarization of the electric field in (4.3) is ϕ as it is the co-polarization component, and the polarization subscripts used in Table 4.2 are omitted here for brevity.

4.1.3. PROPOSED SOLUTION

The proposed methodology aims to estimate the dipole coefficients, $\mathbf{x}'$, to achieve a reasonably accurate desired radiation field, $\mathbf{q}'$ that matches $\mathbf{q}$. A straightforward solution, $\mathbf{x}'$, can be found by utilizing the least squares solution:

$$\mathbf{x}' = (\mathbf{A}^{\mathrm{H}}\mathbf{A})^{-1}\mathbf{A}^{\mathrm{H}}\mathbf{q} \tag{4.4}$$

if $\mathbf{A}^{\mathrm{H}}\mathbf{A}$ is invertible. Although the mentioned inverse matrix exists, the resulting $\mathbf{x}'$ has high sensitivity due to the high condition number of $\mathbf{A}$, which has a form of a Vandermonde matrix caused by the successive raise as a polynomial power by the dipole position as can be seen in (4.1). The matrix $\mathbf{A}$ is required to be relaxed by regularization to reduce the condition number, and to achieve a noise-tolerant solution. To achieve this, a two-step approach is proposed in this work:

1. A relatively small stochastic noise matrix $\boldsymbol{\xi}$ is introduced to the matrix $\mathbf{A}$ as in [74, 75], where $\boldsymbol{\xi} \rightarrow \mathcal{N}(\mu, \sigma^2)$ with the mean $\mu = 0$ and the variance $\sigma^2 = 10$.

Table 4.2: Electric far-fields radiated by IDs

Type	Orientation	Polarization	Electric Fields
Electric	y	θ	$E^e_{\theta,y}(\theta,\phi) = -\cos\theta\sin\phi I^e_y C(\theta,\phi)$
		ϕ	$E^e_{\phi,y}(\theta,\phi) = -\cos\phi I^e_y C(\theta.\phi)$
	z	θ	$E^e_{\theta,z}(\theta,\phi) = \sin\theta I^e_z C(\theta,\phi)$
		ϕ	$E^e_{\phi,z}(\theta,\phi) = 0$
Magnetic	y	θ	$E^m_{\theta,y}(\theta,\phi) = -\frac{1}{\eta}\cos\phi I^m_y C(\theta,\phi)$
		ϕ	$E^m_{\phi,y}(\theta,\phi) = \frac{1}{\eta}\cos\theta\sin\phi I^m_y C(\theta,\phi)$
	z	θ	$E^m_{\theta,z}(\theta,\phi) = 0$
		ϕ	$E^m_{\phi,z}(\theta,\phi) = -\frac{1}{\eta}\sin\theta I^m_z C(\theta,\phi)$

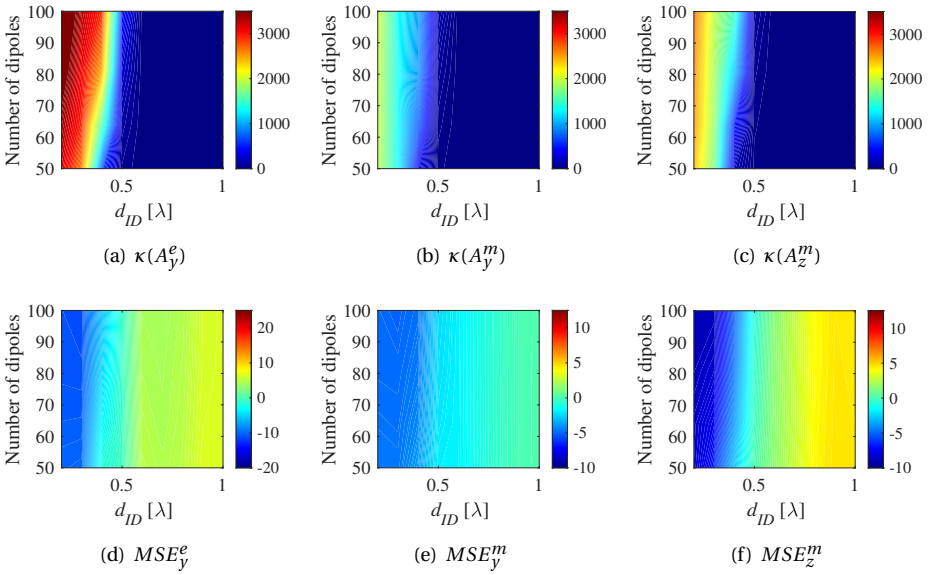

Figure 4.2: Regular topology analysis for the center element of the AUT: (a)-(c) condition number of the matrix **A** for the specified dipole types and orientations, (d)-(f) MSE between the full-wave generated and predicted EEPs of the AUT's center element for the selected ID types and orientations.

2. IDs form a sunflower array topology.

It is also important to mention that only the field magnitudes are formulated by IDM in this work; nevertheless, the work can be extended into complex patterns by including the phase information. This will bring an additional performance trade-off as the stochastic noise used for matrix regularization has an impact on the phases.

4.1.4. NUMERICAL RESULTS: *Cost Definition*

Due to the mutual coupling (MC) effect, the embedded element patterns (EEPs) are highly affected by the adjacent elements depending on their positions. The center and a corner element are selected in this work to demonstrate the effectiveness of the proposed methodology under pattern variations. Furthermore, the array far-field pattern is reconstructed with the predicted EEPs by the constrained IDM and compared with the full-wave simulation. The sunflower ID array topology performance is compared with the conventional regular square topology for different ID types and orientations. This analysis is carried out by jointly considering the condition number of the matrix **A**, $\kappa(\mathbf{A})$, and the mean squared error (MSE) between the simulated and IDM predicted far-field magnitudes:

$$MSE_p^t = 10\log\left(\frac{1}{N_s^2}\sum_{i,j=1}^{N_s}\left(|E_{\mathrm{CST}}(\theta_i,\phi_j)| - |E_p^t(\theta_i,\phi_j)|\right)^2\right) \tag{4.5}$$

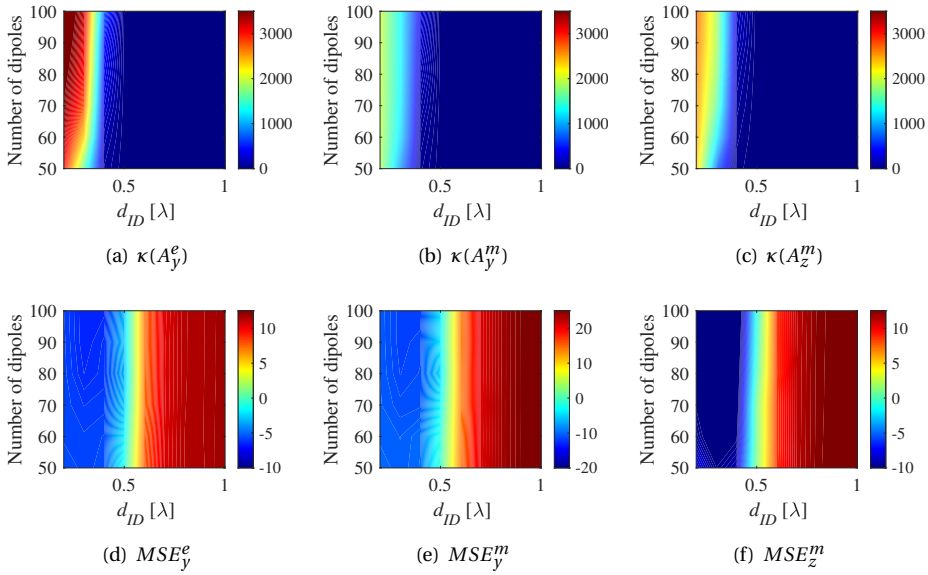

Figure 4.3: Sunflower topology analysis for the center element of the AUT: (a)-(c) condition number of the matrix **A** for the specified ID types and orientations, (d)-(f) MSE between the full-wave generated and predicted EEPs of the AUT's center element for the selected ID types and orientations.

where N_s is the number of samples for θ and ϕ, E_{CST} is the full-wave simulated electric field of the chosen element or the array in the far-field region that is generated by the commercial full-wave simulator CST.

4.1.5. NUMERICAL RESULTS: *Center Element*

The generated EEP of the center element (EEP_{CST}) is taken as a benchmark pattern. The $\kappa(A_p^t)$ and the MSE_p^t are analyzed to find an optimum topology for the constrained IDM. First, the IDs are positioned on the conventional square-grid topology and the number of dipoles are varied with the uniform dipole element spacing (d_{ID}) for a given dipole type and orientation as shown in Fig. 4.2.

As the element spacing increases, the correlation in the matrix **A** decreases, and the condition number is reduced. This is common to all cases as shown in Fig. 4.2. When d_{ID} becomes larger, the IDs start to exceed the defined aperture size. As the aperture is not sufficiently sampled, the MSE increases.

On the other hand, having a small element spacing between the IDs decreases the error between the original and predicted patterns, however, it increases the condition number. Likewise, increase in the number of IDs causes a higher condition number and better MSE when the element spacing is kept low (i.e., $d_{\text{ID}} < 0.5\lambda$), which can be seen as a slight diagonal slope in Fig. 4.2. Although having a large number of dipoles in the constrained IDM can provide more precise predictions, the precision is also limited by the d_{ID} and aperture size.

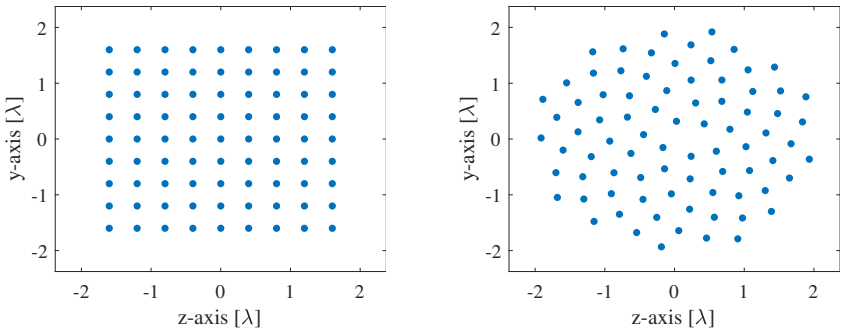

(a) Regular (b) Sunflower

Figure 4.4: 81-element conventional regular and proposed sunflower topologies for the constrained IDM.

Moreover, different dipole orientations and types affect the MSE (due to the differences in the angular dependence given in Table II) and the condition number. In line with the physical reasoning, $z-$oriented $m-$dipole-based constrained IDM shows a better MSE result while having an acceptable $\kappa(A_z^m)$ for $d_{\mathrm{ID}} < 0.5\lambda$ as illustrated in Fig. 4.2(c) and 4.2(f).

As for the sunflower array, the distance from the center to the n-th element, is formed as [72]:

$$\rho_n = d_{ID}\sqrt{\frac{n}{\pi}} \tag{4.6}$$

with the angular displacement of the n-th element:

$$\varphi_n = 2\pi n\beta \tag{4.7}$$

where β is the parameter that controls the angular displacement between two adjacent elements. As β is taken as $\beta = \frac{\sqrt{5}+1}{2}$, the sunflower topology is obtained. In Eq. (4.6), d_{ID} refers to the mean distance between the adjacent elements. Therefore, the analysis of element spacing in the framework of this paper is the mean distance in the sunflower topology.

By introducing the sunflower topology into the constrained IDM, the MSE is significantly improved for all cases as shown in Fig. 4.3. Due to its unique topology with maximal degrees of freedom, the proposed technique captures more details of the EEP and hence provides a wide range of low MSEs, allowing more flexibility in selecting the condition number. Besides, it decreases the condition number in a similar manner compared to the square-grid topology, as illustrated in Fig. 4.3(a), 4.3(b) and 4.3(c). Similar to the regular topology, the $z-$oriented $m-$dipoles have the lowest error particularly when the dipole spacing is lower than 0.5λ.

To visualize the field prediction performance of the proposed topology in the IDM, 81 IDs with a dipole spacing of $d_{\mathrm{ID}} = 0.4\lambda$ were chosen as an example case study as both topologies are illustrated in Fig. 4.4. The simulation results are listed in Table 4.3. It

Table 4.3: Results of the EEP prediction with 81-element IDM for AUT's center element

Dipole	MSE_{reg}	MSE_{sun}	$\kappa(\mathbf{A})_{reg}$	$\kappa(\mathbf{A})_{sun}$
$y-$orien. $e-$ID	-2.4 dB	-6 dB	2467.8	402.4
$y-$orien. $m-$ID	-4.5 dB	-5.5 dB	951.9	203.5
$z-$orien. $m-$ID	-4.7 dB	-11.5 dB	1121.2	133.29

is observed that the proposed topology outperforms the conventional topology in the constrained IDM, and the $z-$oriented $m-$dipole gives the best results as expected. The error is kept below -11 dB while the condition number is reduced from 1121.2 to 133.29, which provides significant stability against noise and stability of the matrix A during the inversion process.

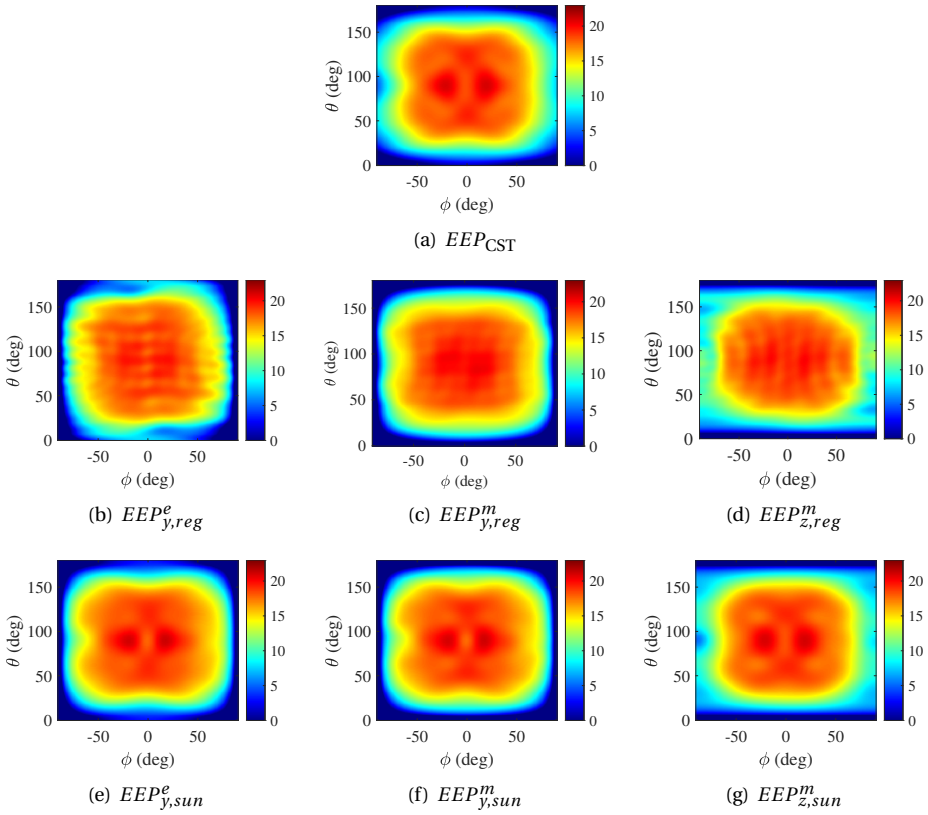

(a) EEP_{CST} (b) $EEP^{e}_{y,reg}$ (c) $EEP^{m}_{y,reg}$ (d) $EEP^{m}_{z,reg}$

(e) $EEP^{e}_{y,sun}$ (f) $EEP^{m}_{y,sun}$ (g) $EEP^{m}_{z,sun}$

Figure 4.5: EEP comparison (in terms of $|E|$) for the center element of the AUT where each topology comprises 81 IDs with $d_{ID} = 0.4\lambda$. The subscripts reg and sun stand for the regular and sunflower topology constrained IDM.

Table 4.4: Results of the EEP prediction with 81-element IDM for AUT's corner element

Dipole	MSE_{reg}	MSE_{sun}	$\kappa(\mathbf{A})_{reg}$	$\kappa(\mathbf{A})_{sun}$
$y-$orien. $e-$ID	-2 dB	-5.6 dB	2479.1	402.3
$y-$orien. $m-$ID	-3.3 dB	-4.31 dB	946.4	203.4
$z-$orien. $m-$ID	-4.3 dB	-8 dB	1122.9	133.3

Beyond the error and condition number quantification, Fig. 4.5 illustrates the comparison between the full-wave simulated and proposed methodology. It is also important to mention that the edges of the EEPs generated by the proposed constrained IDM show small unmatched regions depending on the dipole type and orientation, which brings different θ, ϕ dependence in the ID pattern. In fact, each ID case has a better prediction ability on different edges; the $z-$oriented $m-$dipoles provide good prediction for the angles $60^\circ < |\phi| < 90^\circ$, while the $y-$oriented $e-$dipoles are better at $150^\circ < \theta$ and $\theta < 30^\circ$. Although the effect of mismatches in these regions is small on the MSE (due to low field magnitudes), this is still a small drawback of the proposed constraint with a single-type dipole simplification.

4.1.6. NUMERICAL RESULTS: *Corner Element*

The EEP of a corner element is expected to be different than the middle element due to the finite size of the ground plane and the MC effects caused by the other adjacent elements. For this purpose, a corner element, which is highlighted in Fig. 4.1 with yellow, was chosen as the second case study.

The same analysis for the condition number and MSE is conducted as done in the previous section. The simulations show very similar results that are obtained for the middle element as provided in Fig. 4.2 and 4.3.

The simulation results for the study case with 81 IDs are illustrated in Fig. 4.6 and Table 4.4. Since the EEP of the corner element shows more asymmetrical behavior than the middle element, the field prediction becomes more challenging. Nonetheless, the proposed topology achieves relatively good results, having an error of about -8 dB, while keeping the condition number below 140.

4.1.7. NUMERICAL RESULTS: *Array With Broadside Radiation*

Further study was conducted for the reconstruction of the array pattern (AP) with the obtained EEPs by the proposed methodology. For this purpose, each EEP was predicted by using the sunflower topology with $p-$oriented $t-$dipoles in the constrained IDM. The obtained array pattern, AP_p^t, further is compared with the full-wave simulated array pattern, AP_{CST}.

Fig. 4.7 illustrates the $\theta = 90^o$ and $\phi = 0^o$ pattern cuts. While the prediction achieves good matching with the full-wave simulated pattern cuts, there are some disparities in the extreme angles. Since the prediction is based on absolute patterns, the phase information is missing during the reconstruction, causing potential errors at extreme angles.

4.1.8. CONCLUSION

The sunflower array topology concept has been introduced in the constrained IDM problem to achieve computational efficiency with satisfying antenna far-field prediction accuracy. The impact of the type and orientation of dipoles on the MSE and the corresponding condition number were analyzed for a 5 by 5 patch array as the AUT. The use of magnetic dipoles oriented along the radiating edges of a patch is motivated. A case study with 81 IDs showed that the proposed topology decreases the MSE of the EEP prediction by 6.8 dB and 3.7 dB for the center and edge element, respectively. Moreover, the condition number is reduced by a factor of 10. Lastly, the broadside pattern of the AUT was reconstructed by the predicted EEPs with the proposed methodology and compared with the full-wave simulation result. A good agreement was observed on the pattern cuts; however, the prediction performance degraded at far side lobes. Future study will focus on the complex pattern predictions to overcome this degradation.

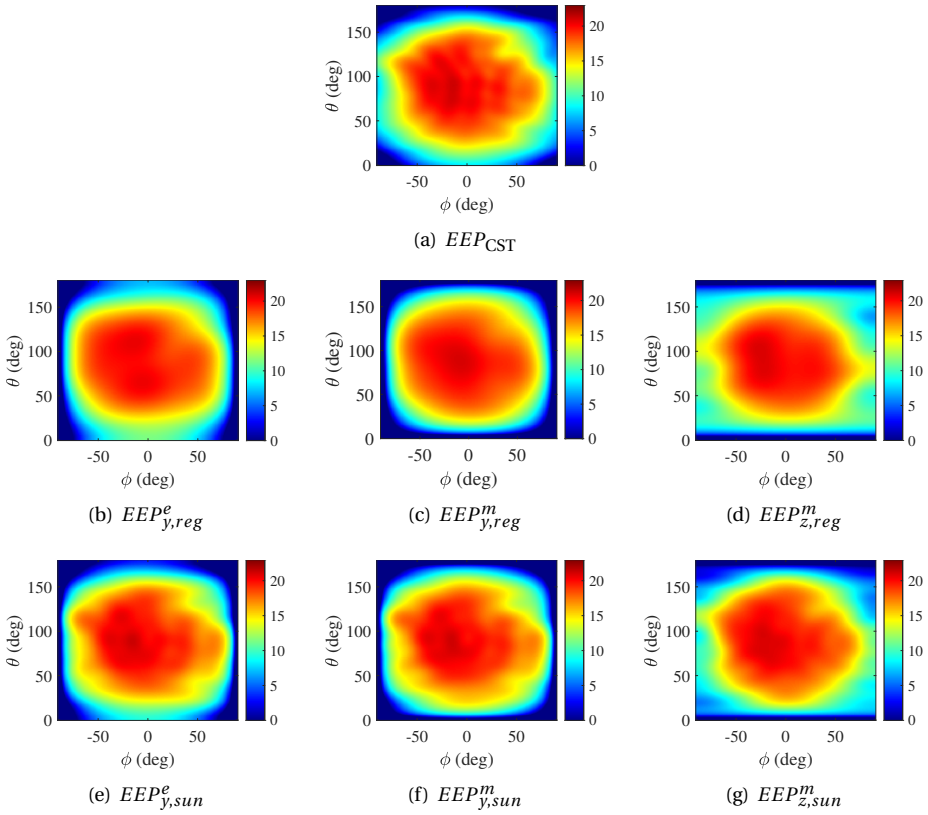

(a) EEP_{CST}

(b) $EEP^{e}_{y,reg}$ (c) $EEP^{m}_{y,reg}$ (d) $EEP^{m}_{z,reg}$

(e) $EEP^{e}_{y,sun}$ (f) $EEP^{m}_{y,sun}$ (g) $EEP^{m}_{z,sun}$

Figure 4.6: EEP comparison (in terms of $|E|$) for the corner element of the AUT where each topology comprises 81 IDs with $d_{ID} = 0.4\lambda$. The subscripts reg and sun stand for the regular and sunflower topology constrained IDM.

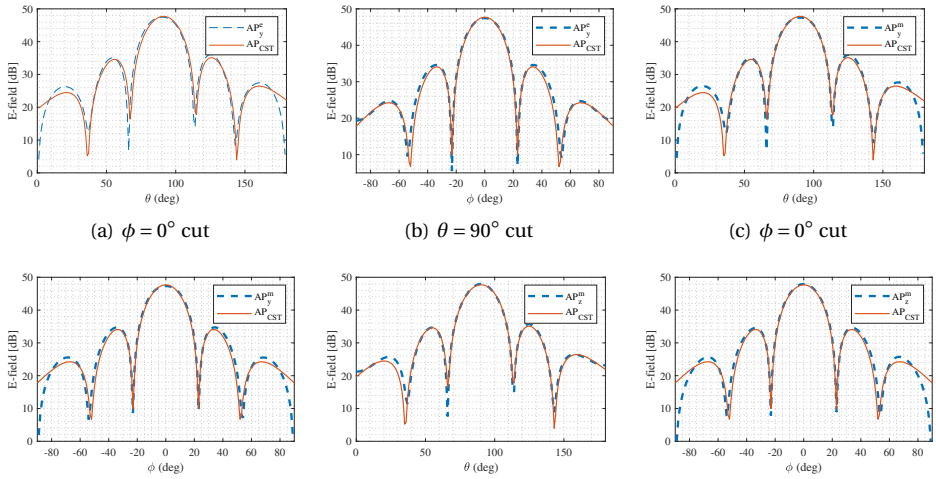

(a) $\phi = 0°$ cut (b) $\theta = 90°$ cut (c) $\phi = 0°$ cut

(d) $\theta = 90°$ cut (e) $\phi = 0°$ cut (f) $\theta = 90°$ cut

Figure 4.7: Array far-field pattern (in terms of $|E|$) comparison for the constrained IDM with the proposed sunflower topology.

4.2. USING SPHERICAL HARMONICS TO MODEL MUTUAL COUPLING EFFECTS ON EMBEDDED ELEMENT PATTERNS

4.2.1. INTRODUCTION

This chapter presents a methodology to characterize the effect of mutual coupling on the EEP far-fields with a relatively low number of parameters. This helps us effectively model the EEP far-fields for any antenna system. In this work, we have chosen the spherical harmonic basis functions to generalize these far-field patterns. These basis functions are characterized by mode numbers $l \in \mathbb{Z}^+$ and $m \in \mathbb{Z}^+$, and each specific combination of these mode numbers gives rise to a distinct far-field pattern. The complex EEP far-fields are assumed to be explained by a weighted sum of these modes. The asymmetry in the patterns could be explained by estimating the weights of each mode. After knowing the dominant modes that can explain the EEP far-fields of the majority of the antenna elements in an array (by performing randomized tests), the weights can be reused for other purposes, such as predicting the patterns for another (unknown) configuration of the array [76, 77]. This way of representing the complex patterns is much more efficient and requires much less time than the full-wave simulations. This work, however, does not focus on the use cases of the estimated weights but focuses more on the estimation of these weights and the reconstruction of the EEP far-fields. The pattern stability against small errors in the weights is also studied, providing valuable inputs for the potential use cases.

Although the proposed procedure is generic and applicable to various scenarios, in this work, we have validated our results against full-wave simulations of an array of pin-fed circular patch antennas.

4.2.2. THEORY OF SPHERICAL HARMONICS

The EEP far-field patterns are decomposed into modes of spherical harmonics. The complex electric field can be represented as a weighted sum [78, Eq. (2.2)]:

$$E(\theta,\phi) = \sum_{l=0}^{\infty} \sum_{m=-l}^{+l} c_l^m Y_l^m(\theta,\phi), \tag{4.8}$$

where

$$Y_l^m(\theta,\phi) = \sqrt{\frac{2l+1}{4\pi}\frac{(l-|m|)!}{(l+|m|)!}} P_l^{|m|}(\cos\theta)\exp\left(\mathrm{j}m\phi\right), \tag{4.9}$$
$$l \in [0,\infty], m \in [-l,+l],$$

where the numbers l, and m represent the mode indices, θ is the elevation angle, ϕ is the azimuth angle in standard spherical coordinate system, P_l^m are the associated Legendre functions of lth degree (or level) and mth order (modes). The c_l^m in (5.4) are the complex weights of these modes. These modes are orthonormal, meaning that:

$$\int_{\Omega} Y_l^m(\theta,\phi) Y_{l'}^{m'}(\theta,\phi) d\Omega = \delta_{ll'}\delta_{mm'} \tag{4.10}$$

where δ is the Kronecker delta function and Ω is the surface area. In matrix form, (5.4) can be written as:

$$\mathbf{e} = \mathbf{Y}\mathbf{c}, \tag{4.11}$$

where $\mathbf{Y} \in \mathbb{C}^{(N_\theta N_\phi)\times L^2}$ has all the spherical wave mode basis functions $\mathbf{Y} = [\mathbf{y}_0^0, \mathbf{y}_1^{-1}, \mathbf{y}_1^0, \mathbf{y}_1^1, \cdots, \mathbf{y}_{L-1}^{L-1}]$ ($L-1$ being the highest degree, L being the number of degrees used). Entries to this matrix $\mathbf{Y}$, i.e., $\mathbf{y}_l^m \in \mathbb{C}^{(N_\theta N_\phi)\times 1}$ are a vectorized form of the spherical modes, where N_θ and N_ϕ are the number of elevation and azimuth directions, respectively. Therefore, $\mathbf{c} \in \mathbb{C}^{L^2\times 1}$, where $\mathbf{c} = [c_0^0, c_1^{-1}, c_1^0, c_1^1, \ldots, c_{L-1}^{L-1}]^{\mathrm{T}}$. Uppercase and lowercase bold fonts refer to matrices and vectors, respectively. Therefore, the vector $\mathbf{e} \in \mathbb{C}^{(N_\theta N_\phi)\times 1}$.

4.2.3. EEP FAR-FIELD RECONSTRUCTION

Given a noisy vectorized far-field measurement, $\mathbf{f} \in \mathbb{C}^{(N_\theta N_\phi)\times 1}$, the coefficients $\mathbf{c}$ are estimated using least squares:

$$\hat{\mathbf{c}} = \left(\mathbf{Y}^{\mathrm{H}}\mathbf{Y}\right)^{-1}\mathbf{Y}^{\mathrm{H}}\mathbf{f}, \tag{4.12}$$

where $\mathbf{Y}^{\dagger} = (\mathbf{Y}^{\mathrm{H}}\mathbf{Y})^{-1}\mathbf{Y}^{\mathrm{H}}$ is the Moore-Penrose inverse [79]. We employ a *Singular Value Decomposition* (SVD)-based approach for computational efficiency and numerical stability via low-rank approximation. The basis function matrix $\mathbf{Y}$ (with independent columns) is decomposed as [79]:

$$\mathbf{Y} = \mathbf{U}\boldsymbol{\Sigma}\mathbf{V}^{\mathrm{H}}, \tag{4.13}$$

where $\mathbf{U} \in \mathbb{C}^{N_\theta N_\phi \times N_\theta N_\phi}$ is a complex unitary matrix, $\boldsymbol{\Sigma} \in \mathbb{C}^{N_\theta N_\phi \times L^2}$ is a rectangular diagonal decaying matrix with non-negative real numbers on the diagonal, and $\mathbf{V} \in \mathbb{C}^{L^2\times L^2}$ is a complex unitary matrix. The coefficients are then computed as:

$$\hat{\mathbf{c}} = \mathbf{V}\boldsymbol{\Sigma}^{-1}\mathbf{U}^{\mathrm{H}}\mathbf{f}. \tag{4.14}$$

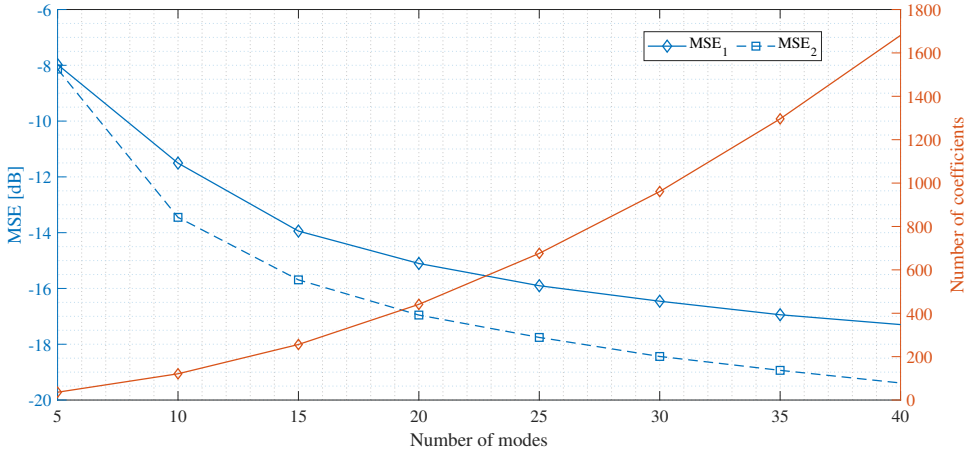

Figure 4.8: Reconstruction analysis of the proposed methodology, showing MSE, number of modes, and coefficients for the corner and center elements of the AUT depicted in Fig. 4.1. MSE_1 and MSE_2 represent the mean squared error between the full-wave simulated pattern and the reconstructed pattern for the corner and center elements, respectively.

After the coefficients are computed, the reconstruction of the absolute electric field can be determined using:

$$\hat{\mathbf{e}} = \mathbf{Y}\hat{\mathbf{c}}. \tag{4.15}$$

4.2.4. ANTENNA UNDER TEST (AUT)

Similar to the previous section, this work considers the same planar array with equally spaced 5 by 5 pin-fed patch antennas as illustrated in Fig. 4.1. The center and corner elements, highlighted in yellow, are selected to demonstrate the performance of the proposed approach at the embedded pattern level. The design parameters of the array can be found in Table 4.1.

4.2.5. RESULTS

Following the AUT topology in Fig. 4.1 and the MSE formulation given in (4.5) to quantify the reconstruction error, the number of modes and their corresponding coefficients are analyzed for the center and corner elements, similar to the previous section. To verify the robustness of the reconstruction, a complex-valued white Gaussian noise with a noise standard deviation of 1% of the coefficient values has been added to the estimated weights of the modes $\hat{\mathbf{c}}$:

$$\hat{\mathbf{c}}^{(\mathrm{err})} = \hat{\mathbf{c}} + \mathbf{n}, \text{ where } \mathbf{n} \overset{i.i.d}{\sim} \mathcal{CN}(\mathbf{0}, \mathrm{diag}(\hat{\mathbf{c}}^2/10^4)). \tag{4.16}$$

Fig. 4.8 shows the analysis of the EEP reconstruction performance for the chosen number of modes, where MSE_1 and MSE_2 represent the mean squared error between the full-wave simulated EEP and the reconstructed EEP for the corner and center elements, respectively. As expected, the MSE decreases with an increasing number of modes. How-

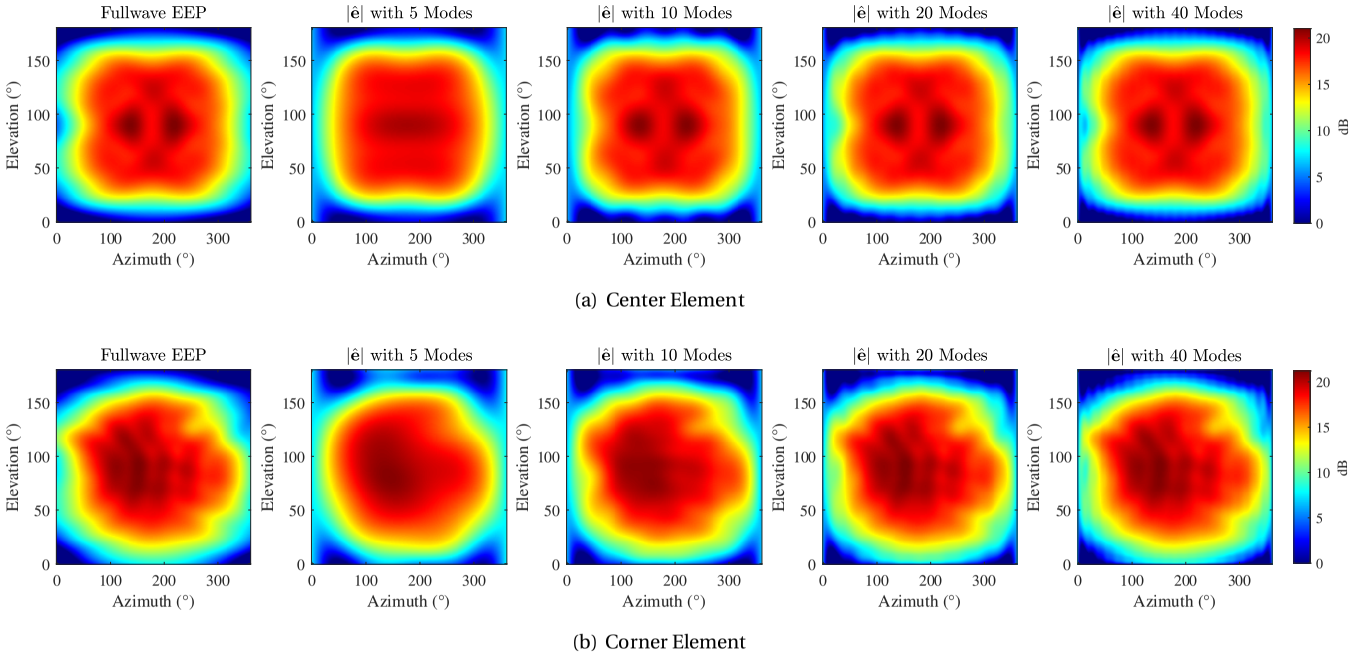

Figure 4.9: Comparison of full-wave simulated ($|\mathbf{e}|$) and reconstructed EEPs ($|\hat{\mathbf{e}}|$) for the (a) corner and (b) center elements of the AUT shown in Fig. 4.1. The EEPs are reconstructed using different numbers of modes (as indicated in the subtitles) to visually illustrate the impact of the number of modes utilized on reconstruction performance.

ever, this also leads to a larger number of coefficients, which is particularly important for ML applications, as these coefficients need to be predicted.

Furthermore, the MSE exhibits different behavior for the center and corner elements due to the impact of MC effects on the EEPs as discussed in the previous section. Fig. 4.9(a) and 4.9(b) illustrate the fullwave simulated EEP with the reconstructed EEPs with different modes. The improvement in reconstruction performance with a higher number of modes can be clearly observed in these figures. Therefore, it is crucial to find a balance between the number of modes and the reconstruction performance, as will be discussed in the next chapter.

4.2.6. CONCLUSION

A novel methodology to efficiently model the MC effects on the EEP far-fields is presented. A more generic decomposition of the EEP far fields is proposed with spherical harmonics. The decomposition is carried out with the SVD algorithm, which makes it numerically stable and computationally efficient. A suitable number of significantly contributing modes can, therefore, be decided by thresholding based on the requirements of the application of interest. An example of the number of contributing modes is presented by considering the MSE for the estimated patterns. It is shown that the reconstruction is adequate for both the amplitude and the phase of the EEP far fields, except for the edges of the field of view. The results of this study suggest that the proposed methodology can be applied efficiently to antenna array problems for calibration or optimization purposes. The next chapters will demonstrate a method where the spherical wave coefficients can be predicted and subsequently used to reconstruct the EEP of an AUT for a given aperiodic topology.

4.3. CONCLUSIONS

This chapter proposes two different methods for fast and efficient decomposition of EEPs, namely, Infinitesimal Dipole Modeling (IDM) and spherical wave expansion. IDM simplifies complex antenna structures by replacing them with infinitesimal dipoles, where each dipole's parameters (excitations) are optimized to match the original fields. While effective, this method often struggles with numerical instability and high computational cost, especially for large arrays. To improve performance, a sunflower-inspired dipole layout was introduced, offering more stable results without relying on iterative optimization.

To further reduce complexity and improve generalization, an alternative approach based on spherical wave expansion was utilized. By capturing the key features of EEPs using a compact set of basis functions, this method is less sensitive to numerical instabilities, offering a scalable and reusable solution for pattern predictions.

Both of these methods provide a reliable EEP reconstruction with high accuracy, efficiency, and robustness, which is essential for ML prediction tasks to reduce the complexity of the problem.

5

UTILIZATION OF BASIS FUNCTIONS FOR EEP PREDICTION VIA MACHINE LEARNING

A robust and scalable methodology is presented for accurate embedded element pattern (EEP) prediction in non-uniform arrays using machine learning (ML). By leveraging constrained infinitesimal dipole modeling (IDM) and spherical wave decomposition as auxiliary basis functions, the framework addresses mutual coupling (MC) effects through EEP prediction with reduced training data requirements. An ensemble prediction framework is introduced, improving generalization and minimizing local prediction errors. To further improve the prediction performance, a stacked generalization technique is proposed, enabling adaptive weighting of auxiliary basis functions. Results demonstrate improved prediction accuracy, model robustness under limited data, and suitability for MC-aware array synthesis applications.

Parts of this chapter have been published in:

N. B. Onat, I. Roldan, F. Fioranelli, A. Yarovoy and Y. Aslan, "Constrained Infinitesimal Dipole Modeling-Assisted Ensemble Prediction of Embedded Element Patterns via Machine Learning," in IEEE Transactions on Antennas and Propagation, vol. 72, no. 9, pp. 7353-7358, Sept. 2024.

N. B. Onat, I. Roldan, F. Fioranelli, A. Yarovoy and Y. Aslan, "Stacked Generalization for Enhanced Embedded Element Pattern Prediction in Non-Uniform Arrays," in URSI Radio Science Letters, accepted for publication.

And partly submitted in:

N. B. Onat, T. Dash, A. Yarovoy and Y. Aslan, "Machine Learning-Assisted Prediction of Spherical Harmonics and Application to the Synthesis of Accurate MIMO Radar Patterns," in IEEE Antennas and Wireless Propagation Letters, under revision.

5.1. CONSTRAINED INFINITESIMAL DIPOLE MODELING (IDM) ASSISTED ENSEMBLE PREDICTION OF EEP VIA MACHINE LEARNING

In the previous chapters, it is shown that the ML-based techniques, especially NNs with their ability to approximate highly nonlinear functions, have been successfully utilized for MC-affected EEP estimations in aperiodic arrays. However, the proposed methods have two major limitations:

(1) Data-driven ML techniques require a large amount of data to avoid over-fitting, significantly increasing the computational time and load for data production.

(2) There is a high dependency of the result on the training data, which results in large prediction performance deviations at different array elements.

Therefore, there is a need to find a reliable method to ensure sufficiently accurate EEP prediction under different MC effects, while reducing the size of the training set.

The major contributions of this work are listed below:

- The constrained infinitesimal dipole modeling (IDM) approach [69, 80] is used for the first time in NN training for robust pattern estimation under limited data size.
- A novel ensemble prediction technique that combines direct pattern prediction with IDM coefficient prediction is proposed to enhance the performance of a single architecture in low-complexity NNs.
- An optimal data-size dependent ensembling weight is introduced for the best pattern prediction accuracy.

5.1.1. SIMULATION SETTINGS

ANTENNA UNDER TEST (AUT)

To demonstrate the performance of the proposed technique, 5-element irregularly spaced rectangular pin-fed patch antenna elements (at 2.85 GHz center frequency designed in the previous chapter) have been utilized as the example aperiodic topology illustrated in Fig. 3.8, where the main design parameters for this section are already listed in Table 4.1. The AUT for EEP prediction is placed at the origin $(0,0)$, while the neighboring elements are randomly distributed (to create a dataset with full-wave simulations) in a defined region limited by an inner and an outer circle. The radius of the inner circle, r_1, is equal to 0.5λ. The radius of the outer circle (r_2) is selected as λ to observe the MC effect on the EEPs by keeping the elements close to each other. The allowed minimum distance between the elements is kept at 0.5λ, making the dataset quasi-random.

EMBEDDED ELEMENT PATTERN (EEP) AND CONSTRAINED INFINITESIMAL DIPOLE MODELING (IDM)

In ML-assisted estimations of $E_n(\theta,\phi)$, the EEPs of each AUT in the training dataset can be simulated via full-wave commercial software. Then an NN can be trained on the pattern data on spherical coordinates [76]. Alternatively, the EEPs can be efficiently approximated by using the constrained IDM where the original array surface is populated with

an equivalent array of infinitesimal electric, $e-$ and magnetic, $m-$dipoles [67]. The excitation coefficients of the dipoles can be estimated via inversion of a Vandermonde-type matrix [70], which is relaxed by introducing a relatively small Gaussian noise [74, 75]. Although using both dipole types along the $y-$ and $z-$ axes in a dense ID array provides a more accurate approximation of the pattern, the inversion of a matrix with a high condition number makes the ID coefficients very sensitive against errors. Improving robustness is critical as it is expected that NN predictions introduce errors in the ID coefficients. In [81], it was shown that the best condition number versus pattern approximation error trade-off is achieved when only $m-$dipoles oriented along the radiating edges of a patch, i.e. along the $z-$axis, are used on a sunflower ID array layout. In particular, for a maximal array radius of λ as in Fig. 1, the use of 81 dipoles was motivated as the optimal ID array size [81]. This preliminary study is exploited in this paper in the IDM formulation for NN-based EEP prediction.

5.1.2. PROPOSED METHODOLOGIES

In this section, two different methods for estimating the absolute EEPs are presented. Both of them use as input the coordinates of the four elements placed in the ring in Fig. 3.8. The first (benchmarked) method directly estimates the center element's EEP, including the neighbor elements' effect. On the other hand, the second and novel method estimates the ID coefficients, and with this, IDM is applied to obtain the EEP. Moreover, both methods are combined in an innovative ensemble model to generate better predictions than each of them alone. Fig. 5.1 shows a block diagram of the full pipeline, highlighting in blue the direct EEP prediction, in green the IDM prediction, and in yellow the ensemble model.

In the next subsections, each block is explained in detail.

DIRECT NN EEP PREDICTION

A Neural Network inspired by the one presented in [76] has been designed to predict the central element's EEP directly in the θ-ϕ domain. The NN consists of two different parts; the first one generates a low-resolution EEP of 36×36, while the second part upscales it to the desired resolution of 180×180 (1-degree resolution in azimuth and elevation). In contrast with the method presented in [76], both blocks are trained together, and therefore, the intermediate low-resolution result is not provided. The upscale block is based on the efficient sub-pixel convolutional neural network (ESPCN) [82]. A schematic of the proposed architecture can be seen in the blue part of Fig. 5.1.

The input to the proposed network $P \in \mathbb{R}^{4\times 2}$ contains the position in polar coordinates of the elements, and it is fed to a 1D convolutional layer with 16 kernels, which encodes the spatial relationships. Then, seven fully connected layers are used, increasing the number of neurons in each step until it reaches 1296. The number of layers and neurons have been tuned manually following a heuristic search [83]. The output of the fully connected layers is then reshaped from 1296 into a 36×36 matrix resembling a low-resolution EEP. Finally, the ESPCN architecture is used to upscale it to a 180×180 matrix. This architecture uses two convolutional layers for feature map extraction and a sub-pixel convolution layer that aggregates the feature maps from the low-resolution space and builds the high-resolution image. In this work, the two hidden convolutional

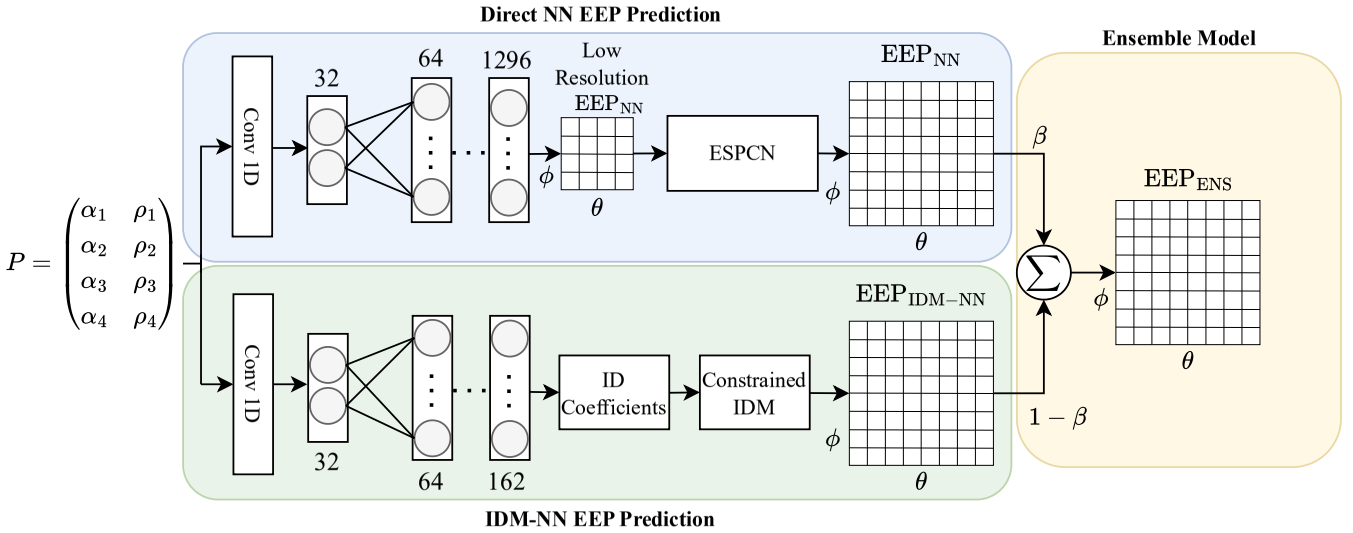

Figure 5.1: Block diagram of the proposed method. The upper branch (in blue) directly predicts the EEP using a two-stage network based on the previous study [76] and the ESPCN [82] architecture. The lower branch (in green) uses a neural network to estimate the ID complex coefficients, and then the constrained IDM generates the EEP. Finally, the ensemble model (in yellow) combines both predictions to generate a higher-quality estimation.

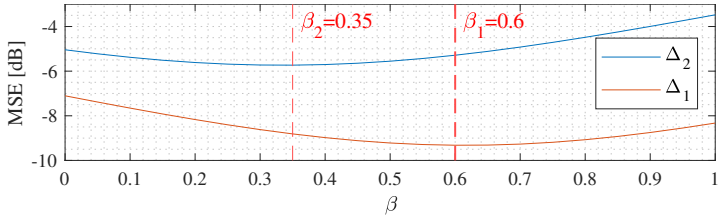

Figure 5.2: Analysis of the weighting value, β, for the ensemble prediction where Δ_1 and Δ_2 represent the datasets comprising 3500 and 1500 data, respectively. The MSE of each point is calculated over the validation set where $\beta_1 = 0.6$ and $\beta_2 = 0.35$ provide the minimum error for the datasets Δ_1 and Δ_2, respectively.

layers have n=32 filters and 3×3 kernel size, while the sub-pixel layer has r2=25 filters to achieve five times the input resolution (upscaling from 36×36 to 180×180). The whole NN model is composed of 2 million parameters, which is a small number for NN architectures [84], with an estimation time several orders of magnitude faster than full-wave simulations [76].

The key to a successful estimation of the EEP is the use of the structural similarity index (SSIM) as a loss for training the neural network. The SSIM was originally developed as a metric for measuring image quality given a reference image, usually to assess the losses due to image compression. However, it has been used recently as a loss function for training neural networks [85]. Formally, the SSIM is defined per pixel as:

$$\mathrm{SSIM(p)} = \frac{2\mu_x\mu_y + C_1}{\mu_x^2 + \mu_y^2 + C_1} \cdot \frac{2\sigma_{xy} + C_2}{\sigma_x^2 + \sigma_y^2 + C_2}, \tag{5.1}$$

where:

- The means μ and standard deviations σ are computed with an 11×11 Gaussian filter of width 1.5.
- $C_1 = (k_1 L)^2$, $C_2 = (k_2 L)^2$, are two constants.
- L is the dynamic range of the matrix (i.e., the difference between the maximum and minimum value).
- k_1 and k_2 are set to the default values of 0.01 and 0.03.

Then, the loss for each matrix can be defined as:

$$\mathscr{L}^{\mathrm{SSIM}}(\mathrm{P}) = 1 - \frac{1}{N}\sum_{p \in P} \mathrm{SSIM(p)}. \tag{5.2}$$

The use of the SSIM loss is a critical component of this work since the value of each matrix element in the EEP is strongly correlated with its neighbors. The SSIM enforces this structural information, in contrast with minimum squared error (MSE) or mean absolute error (MAE), which are computed per cell independently.

Table 5.1: Results for each case study and the average over the validation sets with the benchmark patterns.

Error (MSE)	**Avg. 1**	**Avg. 2**	**Case 1**	**Case 2**	**Case 3**
ε_{IEP} [dB]	0.10	0.07	-0.23	-0.85	-1.73
ε_{UNT} [dB]	0.60	0.55	1.43	-0.18	-0.56
ε_{NN} [dB]	-8.30	-3.48	-10.03	-0.67	-12.80
$\varepsilon_{\text{IDM-NN}}$ [dB]	-7.10	-5.04	-2.69	-9.83	-9.14
ε_{ENS} [dB]	-9.32	-5.73	-5.53	-7.51	-14.10

Notes: Avg. 1 and Avg. 2 indicate the average MSE of the networks trained with the datasets Δ_1 and Δ_2 over the same validation set, whereas the cases are trained with the dataset Δ_2. Case 1, 2, and 3 correspond to the data numbers 129, 205, and 94, respectively.

IDM-NN EEP PREDICTION

A schematic of the network is presented in Fig. 5.1 highlighted in green. The second approach aims to estimate the 81 $z-$oriented $m-$type IDs complex excitations coefficients for given element positions. In this case, the estimation space is much smaller (81 complex coefficients vs 32400); therefore, a simpler network has been used. Similarly, the first layer is a 1D convolutional layer with 16 kernels to encode the spatial information. Then, in order to maintain the same number of layers as in the previous architecture (to have the same network depth and fair comparison of results), seven fully connected layers are included with a final output vector of dimension 81×2 (real and imaginary parts).

The network is trained using the ADAM optimizer [86] with the default hyperparameters (η=0.001, β_1=0.9, β_2=0.999, ϵ=1e-7) and the MSE between the estimated and the true ID coefficients as loss function. Once the ID coefficients are predicted the EEP can be estimated using the IDM technique explained in previous sections.

ENSEMBLE MODEL

A common practice to tackle difficult tasks in machine learning is to use the predictions of different models and combine the outputs to obtain better performance than any of the models alone. This is known as ensemble models, and this technique is used to overcome the limitations that each of the proposed methods presents. Moreover, this allows the design of low-complexity NN architectures suitable for problems when the number of training data is limited. Although several tools can be utilized to obtain an ensemble model, this study employs a simple pixel-wise weighted sum to show the potential of the ensemble prediction with the proposed methods, as illustrated in Fig. 5.1 highlighted in yellow.

5.1.3. RESULTS

Defining the cost function is a critical task due to the high difference between the minimum and maximum values of the EEP, causing a challenge in quantifying the prediction error. In this study, the error is computed for the region $45° \leq \theta \leq 135°$ and $-45° \leq \phi \leq 45°$, which describes the angular region of interest for the typical array applications,

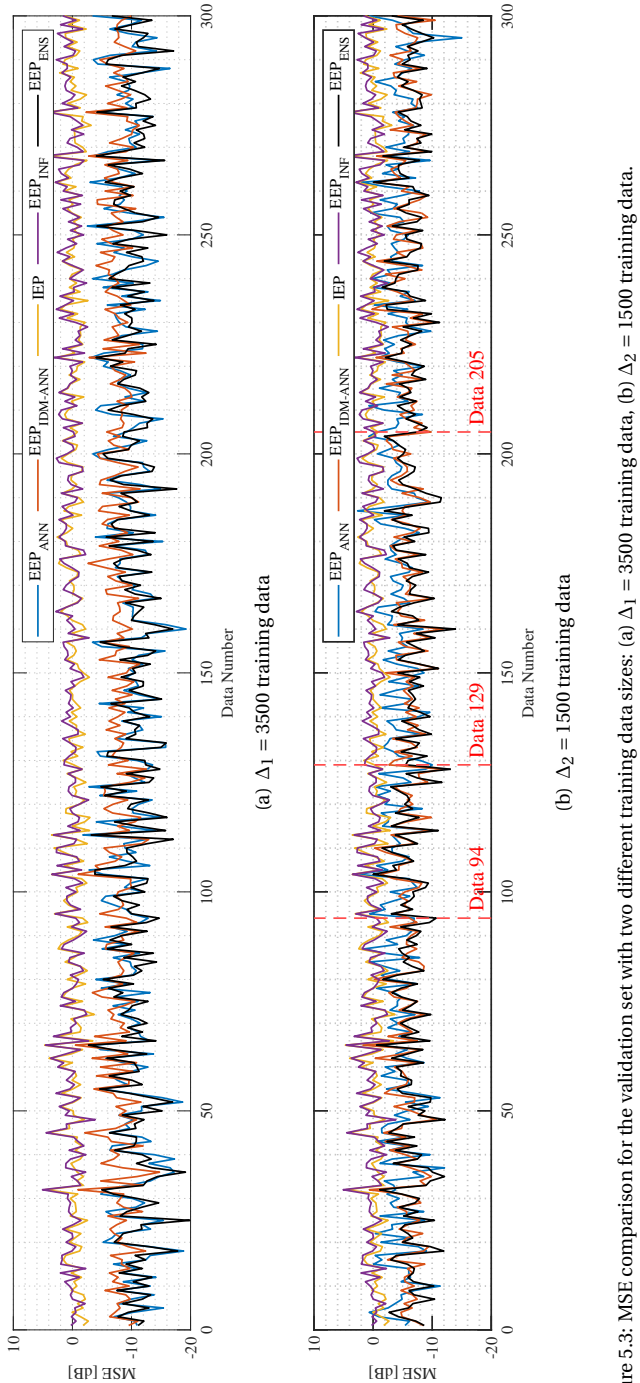

(a) $\Delta_1 = 3500$ training data

(b) $\Delta_2 = 1500$ training data

Figure 5.3: MSE comparison for the validation set with two different training data sizes: (a) $\Delta_1 = 3500$ training data, (b) $\Delta_2 = 1500$ training data.

comprising the high-gain part of the EEP. Therefore, the absolute level of the resulting error is naturally expected to be high regardless of the chosen error function. To this extent, a commonly used error function, MSE, ε_p with p indicating the used methodology and given in (4.5), has been utilized to quantify the error between the full-wave simulated and predicted EEPs.

Two different-sized datasets with quasi-randomly generated 1500 and 3500 full-wave simulations by CST, where each dataset comprises an EEP of an AUT with 180-by-180 samples (in terms of E-field magnitudes in dB), were used for the training of the NNs. These two datasets were chosen based on the average error analysis, whereas reducing the dataset below 1500 data increases the error significantly (larger than −3.7 dB), while the error remains relatively low (below −9.2 dB) beyond 3500 data for the considered topology. Among these data, 300 of them were chosen as a validation for both sets.

The results are presented for five different EEP methodologies, which demonstrates the potential of the proposed ensemble prediction. These methodologies include: (i) full-wave simulated isolated element pattern (IEP), (ii) full-wave simulated unit cell element pattern in an infinite array (EEP_{UNT}), (iii) direct ANN predicted EEP (EEP_{ANN}), (iv) IDM-ANN predicted EEP ($\text{EEP}_{\text{IDM-ANN}}$), and (v) ensemble-predicted EEP (EEP_{ENS}).

The weighting factor, β, is analyzed to obtain an optimum choice for the ensemble prediction block for each training set. Figure 5.2 illustrates the MSE results for each β value for the datasets Δ_1, comprising 3500 training data, and Δ_2, comprising 1500 training data. The cost function MSE is calculated over the same validation set. While the minimum error is obtained by $\beta = 0.35$ for the network trained with the dataset Δ_2, the value of the weight factor shifts to 0.6 with the increase of the training data as shown in Fig. 5.2. It is possible to use ensemble learning techniques to learn the best β for each situation, which is left out of the scope of this work and will be considered in future work.

First, each model is trained with the large dataset, Δ_1, and the corresponding results are illustrated in Fig. 5.3(a) for each validation data, and Table II shows the average results. While the MSE of the IEP and EEP_{UNT} has an average of 0.3 dB, the NN-direct predicted element pattern EEP'_{NN} and the IDM-NN predicted element pattern $\text{EEP}'_{\text{IDM-NN}}$ have an average error of −8.3 dB and −7.1 dB, respectively. Although the MSE of the ANN-based methods generally remains low, the error in specific topology cases can be observed to be higher than the others. These high errors are reduced by the proposed ensemble prediction where the error in EEP'_{ENS} has an average MSE of −9.3 dB over the validation set.

When the size of the data set is reduced by almost 60% to 1500 data, the prediction performance of the NN-based methods becomes worse. Yet, the performance of the proposed ensemble methodology remains in the acceptable range, as can be seen in Fig. 5.3(b) and Table 5.1. To illustrate the performance of the trained networks visually and to highlight the benefits of ensemble prediction, three extreme cases, namely Data 129, 205, and 94, have been selected from the validation set as visualized in Fig.5.3(b). The topologies of these cases are illustrated in Fig. 5.4 with the full-wave simulated AUT pattern (EEP_{CST}) where the MC effect on the EEPs can easily be observed as compared to the IEP and EEP_{UNT}. A summary of the average error result comparisons for the three cases is also provided in Table 5.1 for completeness.

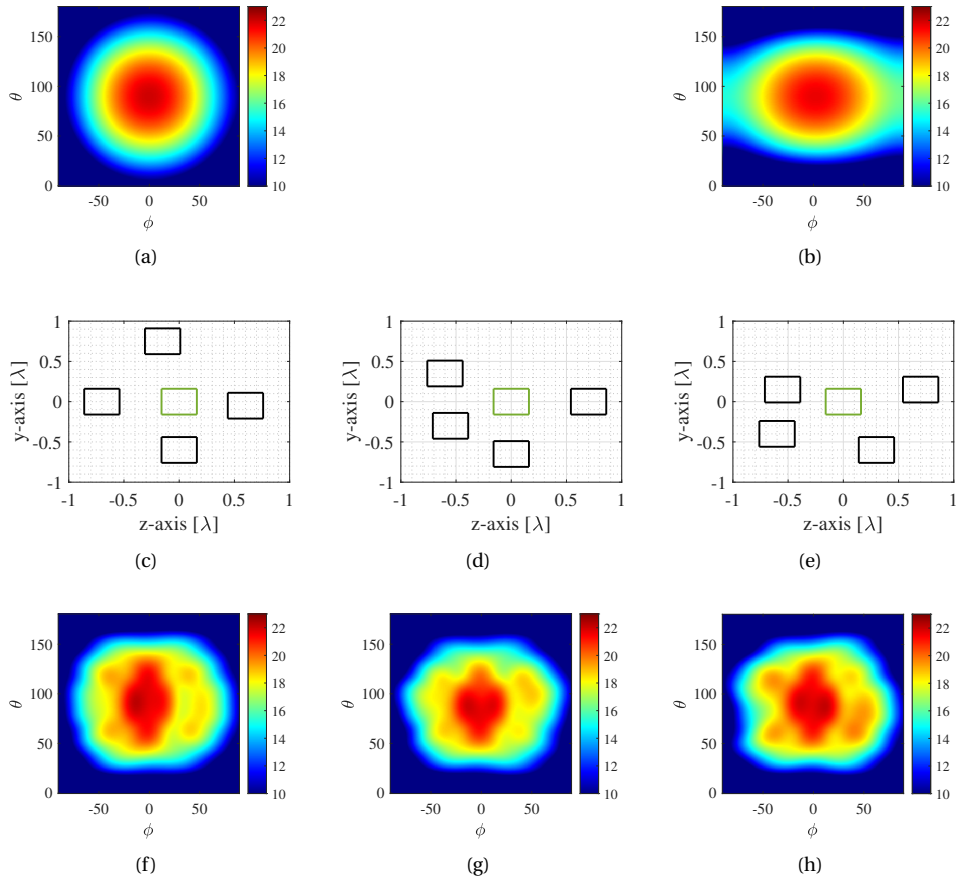

Figure 5.4: 5-element array topologies with different case studies with the corresponding EEPs (E-field, in dB) where the MC effect can easily be observed. The green and black rectangles in the topology figures illustrate the main and neighbor elements, respectively. (a) IEP, (b) EEP_{UNT}, (c) Topology of Data 129, (d) Topology of Data 205, (e) Topology of Data 94, (f) EEP_{CST} of Data 129, (g) EEP_{CST} of Data 205, (h) EEP_{CST} of Data 94.

TOPOLOGY CASE 1

In the first example in Fig. 5.5, while both models provide the outline of the full-wave simulated pattern of the AUT, IDM-NN model fails to predict particularly main beam region and corner regions (e.g., $-60° < \phi < -25°$ and $30° < \theta < 70°$) as can be observed in Fig. 5.5c. Errors in these regions are suppressed by the prediction of the NN-direct model as a result of the ensemble prediction that is shown in Fig. 5.5b. In this way, the MSE between the full-wave simulated pattern and prediction is reduced from -2.69 dB to -5.53 dB.

TOPOLOGY CASE 2

In a case like this, the NN methodology suffers from a higher prediction error, while the IDM-NN model provides a better prediction, as seen in Fig. 5.6. In this example, the

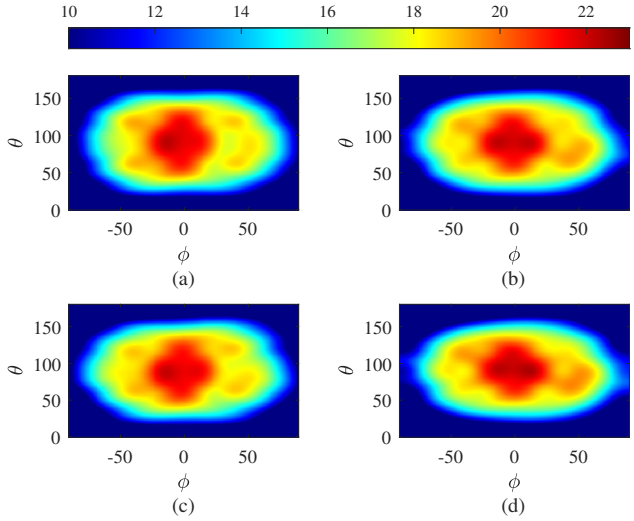

Figure 5.5: Case 1: EEP (E-field, in dB) prediction results for Data 129 with the training set Δ_2: (a) EEP_{CST} is full-wave simulated EEP, (b) EEP_{ENS} is the ensemble predicted EEP, (c) EEP_{NN} is the direct NN predicted EEP, (d) $\text{EEP}_{\text{IDM-NN}}$ is the IDM-NN predicted EEP.

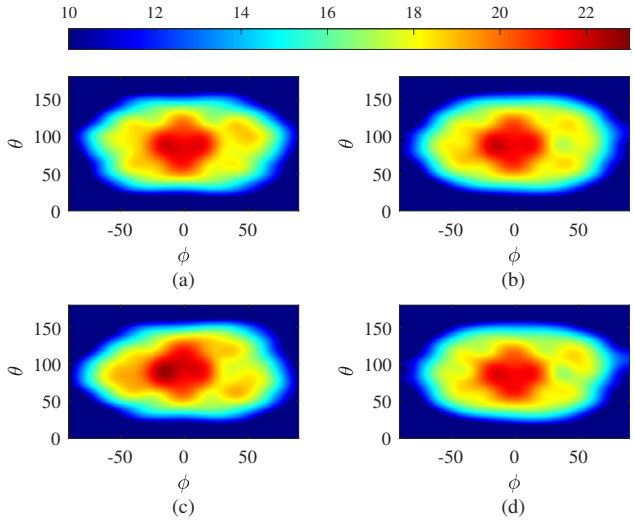

Figure 5.6: Case 2: EEP (E-field, in dB) prediction results for Data 205 with the training set Δ_2: (a) EEP_{CST} is full-wave simulated EEP, (b) EEP_{ENS} is the ensemble predicted EEP, (c) EEP_{NN} is the direct NN predicted EEP, (d) $\text{EEP}_{\text{IDM-NN}}$ is the IDM-NN predicted EEP

.

error by the NN-direct prediction is reduced from −0.67 dB to −7.51 dB by the superior

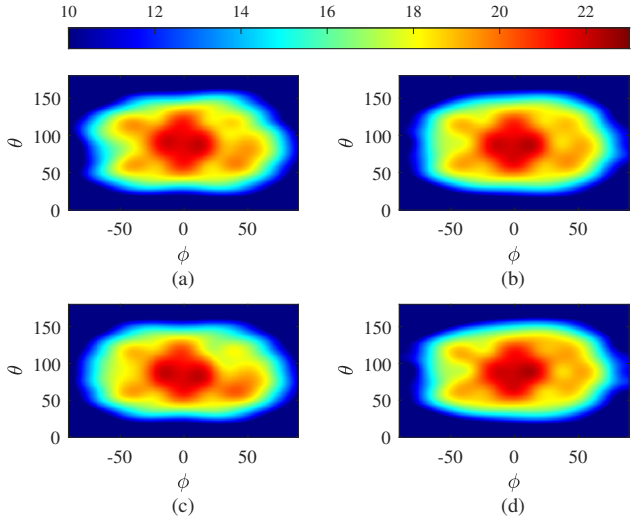

Figure 5.7: Case 3: EEP (E-field, in dB) prediction results for Data 94 with the training set Δ_2: (a) EEP_{CST} is full-wave simulated EEP, (b) EEP_{ENS} is the ensemble predicted EEP, (c) EEP_{NN} is the direct NN predicted EEP, (d) $\text{EEP}_{\text{IDM-NN}}$ is the IDM-NN predicted EEP.

prediction by the IDM-NN model, as can be seen in Table 5.1.

TOPOLOGY CASE 3

In rare cases, the error of both predictions can be relatively low, as shown in Fig. 5.3(b). Particularly in these cases, the ensemble prediction reduces and stabilizes the peak errors even more by averaging the resulting patterns from the proposed ANN methodologies. Even with a simple averaging, the obtained ensemble prediction agrees with the full-wave simulation by decreasing the error from −9.14 dB to −14.1 dB as visually illustrated in Fig. 5.7.

5.1.4. CONCLUSION

A novel ensemble prediction technique is proposed to achieve sufficiently accurate and fast EEP prediction under different MC effects with reduced training data size. The method is based on combining; (i) a direct approach comprising a two-stage NN that predicts EEPs in $\theta-\phi$ plane from the full-wave simulated data, and (ii) the constrained IDM, where ID excitations are predicted by a second NN, obtaining the EEP from the predicted coefficients. For validation, quasi-random 5-element S-band pin-fed rectangular patch array topologies are employed. The results have proven the potential of the proposed method in achieving a lower MSE in EEPs (by about 60% on average) while reducing the data size (by nearly 60%). Future work will explore more advanced neural network architectures and the training of the full ensembling model as a single structure. Additionally, to improve the accuracy of the datasets towards the real products, future work might also consider introducing realistic parameter sensitivity-error models

in the simulations.

5.2. STACKED GENERALIZATION FOR ENHANCED EMBEDDED ELEMENT PATTERN PREDICTION

5.2.1. INTRODUCTION

An ensemble prediction framework was proposed in the previous section to achieve accurate and fast EEP prediction under varying MC effects with a reduced training dataset. This was achieved by manually applying a weighted sum to the prediction results from the base models, where the weighting factor, β, is optimally chosen based on the performance of the base models on the validation set. However, such manual strategies fail to exploit the localized advantages of each method (for instance, one network may provide superior estimation of the main lobe, while the other may perform better in estimating the SLLs).

In this section, we propose a new stacked generalization model where the meta model via a custom Hadamard layer:

- determines optimal weighting matrices for each base model to exploit their localized strengths,
- eliminates the averaging error caused by the manual computation over the validation set,
- enables multiple base model integration to enhance the prediction performance.

5.2.2. PROBLEM FORMULATION

To ensure consistency with the methodologies in the previous section, this study utilizes the same 5-element, irregularly spaced, rectangular pin-fed patch array topology operating at the same center frequency, 2.85 GHz, as depicted in Fig. 3.8. The AUT is positioned at the center of the array's aperture, while the neighboring elements are confined to a defined region —highlighted in green in Fig. 3.8— bounded by an inner and outer circle. The inner circle has a radius corresponding to the minimum element spacing, $r_1 = \lambda/2$, r_2 is set equal to r_1. This configuration maintains the elements close to each other, allowing for the observation of the MC effects on the EEP for varied array topologies.

The pattern error is computed for the region $20° \leq \theta \leq 160°$ and $-70° \leq \phi \leq 70°$ describing the angular region of interest for common array applications, where θ and ϕ follow the standard spherical coordinate system. To quantify the error between the predicted and full-wave generated EEP, the MSE given in (4.5) is utilized as in the previous chapter.

For the ML-assisted prediction of EEPs, the training data can be generated using full-wave simulations with randomized array layouts around an element under test. The power pattern of the element generated for the dataset is a function of the spherical angles θ and ϕ, e.g., each having 180 samples, resulting in a 180 by 180 matrix. A straightforward prediction method is a direct EEP estimation using a neural network on this

dataset. An alternative method is to modify the base model and estimate the EEP under the new base. IDM is one technique that can serve as a base [69, 80] through ID coefficients, which are used in EEP prediction through the array factor relation.

In the IDM approach, the array surface is replaced by an equivalent array of infinitesimal electric (e-) and magnetic (m-) dipoles, with excitation coefficients derived by inverting a Vandermonde-type matrix, adjusted with Gaussian noise for stability. While a dense array of e- and m-dipoles offers higher accuracy, the high condition number of the matrix makes the coefficients sensitive to errors, particularly those introduced by NNs. Our previous work identified an optimal trade-off between condition number and pattern approximation error by using only m-dipoles oriented along the radiating edges (z-axis) of a patch, arranged in a sunflower layout. For a maximum array radius of λ, 81 dipoles were found to be optimal where it was utilized to enhance array prediction performance in previous section.

5.2.3. REVISITING PREVIOUSLY PROPOSED EEP PREDICTION METHODOLOGIES

This section summarizes the two previously proposed methods used for estimating the absolute EEPs, as well as the manual ensemble method combining both.

DIRECT ESTIMATION

The input to the proposed network $P \in \mathbb{R}^{4\times 2}$ represents the positions in polar coordinates of the antenna elements, and they are processed through a 1D convolutional layer with 16 kernels to encode spatial relationships. This is followed by seven fully connected layers, incrementally increasing the neurons to 1296, determined via heuristic tuning. The output is reshaped into a 36×36 matrix resembling a low-resolution EEP, which is then upscaled to 180×180 using an ESPCN architecture. This involves two convolutional layers (32 filters, 36×36 kernel size) and a sub-pixel convolutional layer (25 filters) for upscaling. The model contains 2 million parameters, making it relatively lightweight, and achieves estimation speeds significantly faster than full-wave simulations. A critical component of the design is the use of the Structural Similarity Index (SSIM) as a loss function during training. SSIM enforces structural relationships between matrix elements, which are crucial for EEP accuracy, outperforming traditional loss functions like MSE or MAE that treat matrix cells independently.

IDM-BASED ESTIMATION

The second approach estimates 81 z-oriented m-type ID complex excitation coefficients for the given element positions, reducing the estimation space from 32,400 to 81 coefficients. The architecture includes a 1D convolutional layer with 16 kernels for spatial encoding, followed by seven fully connected layers to match the depth of the previous network for consistent comparisons. The final output is an 81×2 vector representing the real and imaginary parts of the coefficients. The network is trained using the ADAM optimizer with default hyperparameters (η=0.001, β_1=0.9, β_2=0.999, ϵ=1e-7) and the Mean Squared Error (MSE) loss function to minimize the error between the predicted and true ID coefficients. Once the coefficients are estimated, the EEP is computed using the previously described IDM technique.

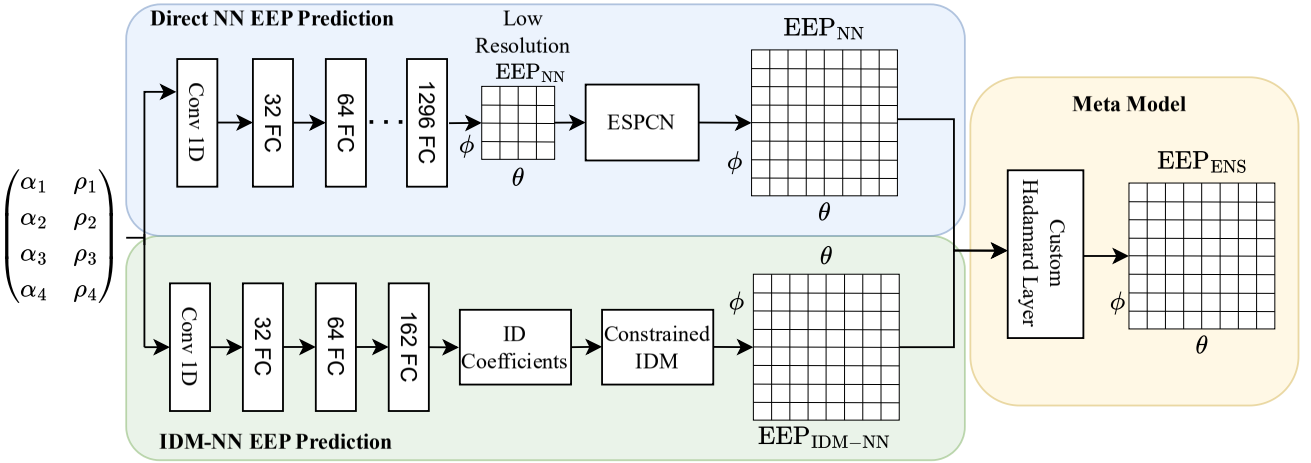

Figure 5.8: The block diagram of the proposed approach. The lower path (green) comprises an NN for estimating the ID complex coefficients, which is utilized to reconstruct the EEP via constrained IDM. In the upper path (blue), a two-stage network and the ESPCN architecture are used to predict the EEP directly. The proposed meta model (yellow), the custom Hadamard layer, enhances the prediction performance from preliminary predictions of the base models.

Table 5.2: The average MSE results for the base and stacked generalization models trained with Δ_1 and Δ_2 with the additional results of two example cases of these models trained with the dataset Δ_1.

Error (MSE)	Dataset		Cases with Δ_1	
	Δ_1	Δ_2	Case 1	Case 2
ϵ_{IEP} [dB]	-10.56	-10.56	-11.61	-12.29
ϵ_{NN} [dB]	-16.10	-18.85	-15.66	-24.63
$\epsilon_{\text{IDM-NN}}$ [dB]	-16.54	-19.60	-18.50	-18.34
ϵ_{ENS} [dB]	-17.73	-21.02	-19.67	-24.64

EMPIRICAL ENSEMBLE PREDICTION

The method presented in the previous section utilized two distinct networks, base models, to estimate EEPs independently (explained in the previous section), subsequently combining them to produce a more accurate EEP by leveraging the strengths of each network. The original methodology achieved this combination through a weighted average, with the weighting coefficient β determined manually over the validation set and must be recalculated whenever the dataset size or type changes.

Figure 5.2, illustrates the change of the β depending on the dataset size. In addition to manually determining β, a single coefficient cannot achieve consistent performance across various datasets due to differences in the prediction performance of the base models.

5.2.4. NEWLY PROPOSED TECHNIQUE: STACKED GENERALIZATION

The proposed method replaces the simple weighted average discussed in Section 3.3 with a newly trained single-layer network to enhance prediction performance. This network utilizes a custom layer designed specifically for this application, which computes the Hadamard product of the preliminary EEPs and adds them as follows:

$$EEP_{\text{ENS}} = EEP_{\text{NN}} \odot A + EEP_{\text{IDM-NN}} \odot B \tag{5.3}$$

where $\odot$ is the Hadamard product and $A \in \mathbb{R}^{140\times140}$ and $B \in \mathbb{R}^{140\times140}$ are the weights. EEP_{ENS}, EEP_{NN}, and $EEP_{\text{IDM-NN}}$ denote the predicted EEPs by the meta, NN-direct and IDM-NN models, respectively, given in Fig. 5.8. The network aims to find the optimal matrices A and B to maximize the prediction accuracy. With this, it is possible to have different averages for different EEP regions, exploiting each method's advantages.

Figure 5.8 shows the block diagram of the full approach. For this work, each network has been trained independently. The first two networks were trained as described in previous section. The single-layer ensemble has been trained using Adam optimizer and MSE as a lost function. Either or 1500 (dataset Δ_1) or 3500 (dataset Δ_2) EEPs have been used for training, 200 for validation, and 50 for tests. All the results presented in the next section are computed in the test set, with data completely unseen for the network.

5.2.5. SIMULATION RESULTS

In this section, the results are presented for four different EEP methodologies to illustrate the potential of the proposed stacked generalization model. These methodologies comprise: (i) full-wave simulated isolated element pattern (IEP), (ii) NN-direct predicted EEP

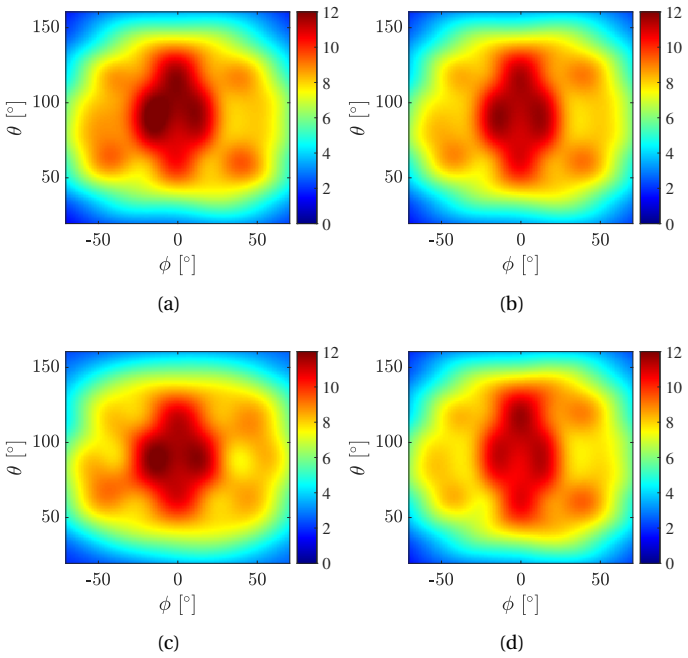

Figure 5.9: EEP (in linear) of Case Topology 2 with (y_i, z_i) = {(-0.60, -0.10), (0.25, -0.50), (0.20, 0.60), (0.70,-0)}λ and AUT is located at the origin. (a) Full-wave generated EEP, (b) EEP_{ENS}, (c) $\text{EEP}_{\text{IDM-NN}}$, (d) EEP_{NN}.

(EEP_{NN}), (iii) IDM-NN predicted EEP ($\text{EEP}_{\text{IDM-NN}}$), and (iv) ensemble predicted EEP via stacked generalization (EEP_{ENS}).

Table 5.2 shows the results for each methodology described above. While the meta model learns how to weigh the predictions of each base model to enhance the final prediction, it improves the average MSE (ε_{ENS}) error over the test set, achieving −17.73 dB and −21.02 dB in average with the datasets Δ_1 and Δ_2, respectively. Although the proposed base models perform well with larger datasets, their performance begins to fluctuate with the smaller dataset, reducing the reliability of the predictions, which is partly reflected in the average MSE errors shown in Table 5.2. To illustrate this, two array topologies (case 1 and 2) from the test set are chosen where the models are trained with the smaller dataset, Δ_1.

In case topology 1, while the IDM-NN model achieves an MSE ($\varepsilon_{\text{IDM-NN}}$) of −18.50 dB, the error of the NN-direct model (ε_{NN}) remains at −15.66 dB above the average MSE. The difference in the error can also be observed on the EEPs where the NN-direct fails to predict the high gain region accurately, as illustrated in Fig. 5.9. On the other hand, the proposed meta model improves the performance of the prediction and reduces the MSE to −19.67 dB, below the average MSE. As Fig. 5.9 shows, the final predicted EEP comprises the localized accuracies of the preliminary predictions.

In some rare cases, one method may significantly outperform the other. In such instances, the meta-model must intelligently combine the predictions, giving more weight

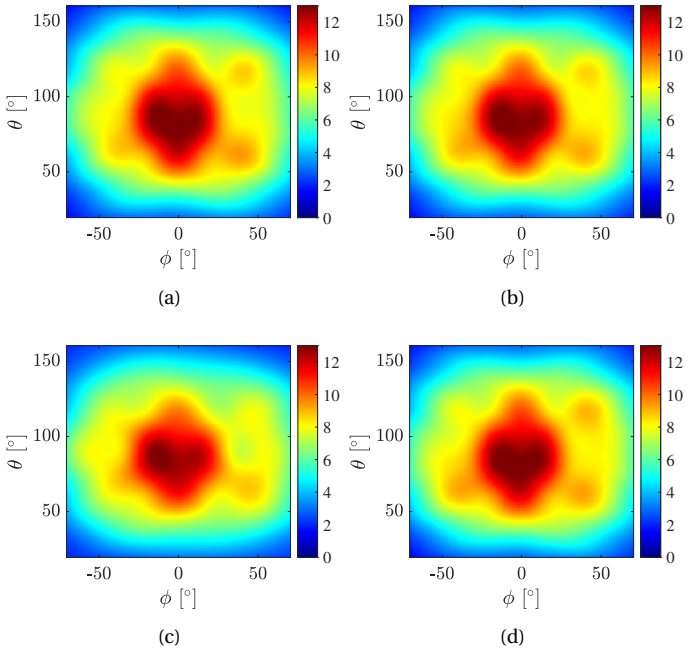

Figure 5.10: EEP (in linear) of Case Topology 2 with (y_i, z_i) = {(0.30, 0.60), (-0.50, 0.60), (-0.20, -0.60), (-0.65,-0.20)}λ and AUT is located at the origin. (a) Full-wave generated EEP, (b) EEP_{ENS}, (c) $\text{EEP}_{\text{IDM-NN}}$, (d) EEP_{NN}.

to the base model that provides the more accurate result. Figure 5.10 presents the case topology 2, where the NN-direct model delivers one of the best predictions, achieving an MSE of −24.63 dB, while the IDM-NN model remains above −18.5 dB. As expected, the proposed meta-model accurately generates the final prediction by weighing the NN-direct model's prediction, resulting in an MSE of −24.64 dB as shown in Fig. 5.10.

5.2.6. CONCLUSION

This chapter presents a novel stacked generalization method designed to improve the prediction accuracy of EEPs under the MC effects. The approach combines two base models: a two-stage NN for direct EEP prediction using full-wave generated data, and a fully connected NN for estimating IDM coefficients, which approximate full-wave EEPs through constrained IDM. A key innovation of the proposed method lies in its meta-model, which determines optimal weighting matrices for each base model to exploit their localized strengths. This eliminates averaging errors associated with manual computations. Furthermore, the framework supports the integration of multiple base models, enhancing overall prediction performance. The effectiveness of the proposed method is validated on non-uniformly spaced 5-element pin-fed patch antenna arrays, demonstrating its capability to deliver accurate and efficient EEP predictions. This work establishes a foundation for developing more robust prediction methodologies for complex antenna systems, especially in scenarios where dataset size and accuracy are critical

constraints.

5.3. SPHERICAL HARMONICS-BASED EEP PREDICTION

5.3.1. INTRODUCTION

In previous sections, it has been discussed that many of the EEP prediction approaches, especially those based on neural networks, require large and carefully generated datasets to generalize the prediction problem. As an example technique, the IDM has been proposed to enhance the prediction performance with stacked generalization, but these methods often suffer from numerical instability, particularly due to the ill-conditioning of matrices involved in the IDM formulation, making the technique less error tolerant.

To overcome these limitations, EEP prediction using spherical wave expansion offers a fundamentally different and highly efficient approach, as explained in Section 3. By representing EEP far-fields (e-fields) as a superposition of spherical harmonic modes, the method captures both the symmetry and asymmetry in radiation patterns using only a compact set of coefficients. Once the dominant modes for a given array topology are identified, their associated weights can be reused to estimate EEPs for other configurations with minimal computation and high accuracy.

This framework not only provides a physically interpretable and compact representation of EEPs but also demonstrates robustness to small errors in coefficient estimation, which is an essential quality for real-world applications. In addition to the previously proposed approaches, spherical wave expansion offers a scalable, stable, and data-efficient solution for fast and accurate EEP prediction.

The problem formulation of the problem is based on Section 4.2, however, this section focuses on the absolute pattern prediction in aperiodic topologies. Furthermore, the application of the methodology in MIMO radars will be further discussed in the next chapter, as this chapter introduces the prediction technique.

5.3.2. PROBLEM FORMULATION

ANTENNA UNDER TEST (AUT)

This work considers a K-element (K to be varied between 2 to 8) irregularly spaced, pin-fed circular patch antenna array operating at a center frequency of 10 GHz. The use of a different antenna element type, number, and frequency not only demonstrates the methodological diversity and broader applicability of the proposed approach but also aligns with the design specifications of the array prototype presented in Appendix A.1. Figure 3.8 illustrates an example aperiodic array topology, and the key design parameters are provided in Table 5.3. The aim is to predict the EEP of the AUT, which is positioned

Table 5.3: Antenna design parameters

Center frequency	10 GHz	**Aperture length** (A_y)	2λ
Patch radius	4.44 mm	**Aperture width** (A_z)	2λ
Feeding type	pin-fed	**Substrate height** (h)	0.41 mm
Circle rad. $[r_1, r_2]$	$[0.5, 1]\lambda$	**Relative permittivity** (ϵ_r)	3.55

at the origin (0,0), while the surrounding elements are randomly placed within a specified region, constrained by an inner and an outer circle. The inner circle has a radius of $r_1 = 0.5\lambda$, where λ is the wavelength. The outer circle has a radius of $r_2 = \lambda$, ensuring that the MC effects on the EEPs can be analyzed by maintaining close element spacing. To preserve a quasi-random distribution, the minimum allowable separation between elements is set at 0.5λ. Furthermore, each EEP in the topology can be found by changing the AUT between the elements in the topology.

SPHERICAL HARMONICS

The EEP far-field patterns can be decomposed into modes of spherical harmonics, which are considered the basis functions. Since this work focuses on the optimization of the array power pattern, the absolute value of the electric field is considered. The aforementioned field can be represented as a weighted sum [78, Eq. (2.2)]:

$$|E(\theta,\phi)| = \sum_{l=0}^{\infty} \sum_{m=-l}^{+l} c_l^m Y_l^m(\theta,\phi), \tag{5.4}$$

where

$$Y_l^m(\theta,\phi) = \sqrt{\frac{2l+1}{4\pi}\frac{(l-|m|)!}{(l+|m|)!}} P_l^{|m|}(\cos\theta)\exp\left(\mathrm{j}m\phi\right), \tag{5.5}$$
$$l \in [0,\infty], m \in [-l,+l],$$

where the numbers l, and m represent the mode indices, θ is the elevation angle, ϕ is the azimuth angle, P_l^m are the associated Legendre functions of lth degree (or level) and mth order (modes). The c_l^m in (5.4) are the complex weights of these modes. These modes are orthonormal, meaning that:

$$\int_{\Omega} Y_l^m(\theta,\phi) Y_{l'}^{m'}(\theta,\phi) d\Omega = \delta_{ll'}\delta_{mm'} \tag{5.6}$$

where δ is the Kronecker delta function and Ω is the surface area. The (5.4) can be written with matrix form as:

$$|\mathbf{e}| = \mathbf{Y}\mathbf{c}, \tag{5.7}$$

where $\mathbf{Y}$ contains all the spherical wave mode basis functions $\mathbf{Y} = [\mathbf{y}_0^0, \mathbf{y}_1^{-1}, \mathbf{y}_1^0, \mathbf{y}_1^1, \cdots, \mathbf{y}_{L-1}^{L-1}]$ ($L-1$ being the highest degree, L being the number of degrees used). Each entry to this matrix $\mathbf{Y}$, i.e., $\mathbf{y}_l^m \in \mathbb{C}^{(N_\theta N_\phi)\times 1}$ are vectorized form of the spherical modes (basis functions), where N_θ and N_ϕ are the number of elevation and azimuth directions, respectively. The matrix $\mathbf{Y} \in \mathbb{C}^{(N_\theta N_\phi)\times L^2}$ is then a 2D matrix. Therefore, $\mathbf{c} \in \mathbb{C}^{L^2\times 1}$, where $\mathbf{c} = [c_0^0, c_1^{-1}, c_1^0, c_1^1, \ldots, c_{L-1}^{L-1}]^{\mathrm{T}}$. Uppercase and lowercase bold fonts refer to matrices and vectors, respectively. Therefore, the vector $|\mathbf{e}| \in \mathbb{R}^{(N_\theta N_\phi)\times 1}$.

EEP FAR FIELD RECONSTRUCTION

If the noisy vectorized far-field measurement, $\mathbf{f} \in \mathbb{C}^{(N_\theta N_\phi)\times 1}$, is given, the spherical wave mode coefficients are estimated using least squares:

$$\hat{\mathbf{c}} = \left(\mathbf{Y}^{\mathrm{H}}\mathbf{Y}\right)^{-1}\mathbf{Y}^{\mathrm{H}}\mathbf{f}, \tag{5.8}$$

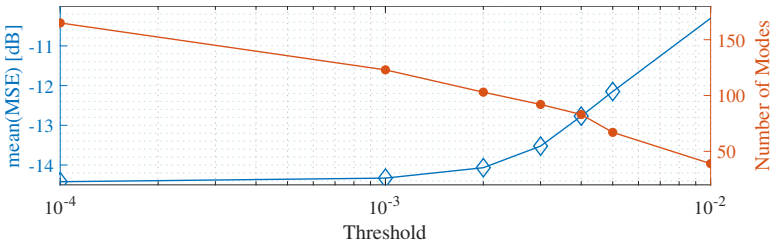

Figure 5.11: An example comparison plot showing the selected number of modes with a defined threshold for the absolute value of the coefficients, where MSE quantifies the error over the 4-element dataset comprising 4000 randomly generated topologies.

where $\mathbf{Y}^{\dagger} = (\mathbf{Y}^{\mathrm{H}}\mathbf{Y})^{-1}\mathbf{Y}^{\mathrm{H}}$ is the Moore-Penrose inverse [79]. This paper employs a *Singular Value Decomposition* (SVD)-based approach for computational efficiency and numerical stability via low-rank approximation. The basis function matrix $\mathbf{Y}$ (with independent columns) is decomposed as [79], and the coefficients are compued as:

$$\mathbf{Y} = \mathbf{U}\Sigma\mathbf{V}^{\mathrm{H}}, \quad \hat{\mathbf{c}} = \mathbf{V}\Sigma^{-1}\mathbf{U}^{\mathrm{H}}\mathbf{f}, \tag{5.9}$$

where $\mathbf{U} \in \mathbb{C}^{(N_\theta N_\phi)\times 1}$, $\Sigma \in \mathbb{C}^{L^2\times L^2}$ (a decaying diagonal matrix), and $\mathbf{V} \in \mathbb{C}^{L^2\times L^2}$. The number of significant modes used is $L^2 = 169$ after manual investigation. After the coefficients are computed, the reconstruction of the absolute electric field can be determined using:

$$|\hat{\mathbf{e}}| = \mathbf{Y}\hat{\mathbf{c}}. \tag{5.10}$$

5.3.3. SIGNIFICANT SPHERICAL MODES FOR EEP PREDICTION AND THE PROPOSED NN ARCHITECTURE

Following the AUT topology in Fig. 3.8 with variable $K-$element, the NN model takes the coordinates of neighboring elements in the defined region as input. Since the num-

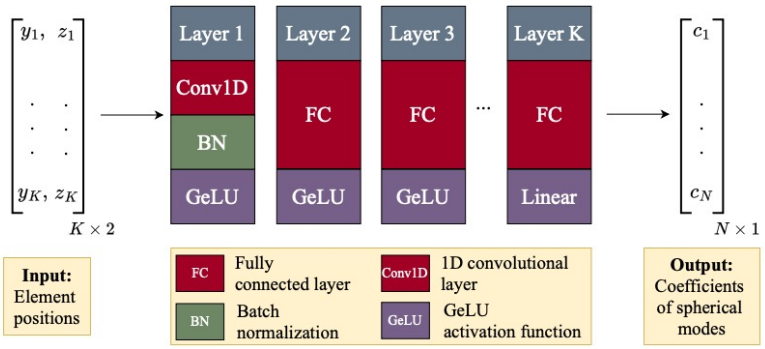

Figure 5.12: Block diagram of the proposed architecture. K is the considered total number of neighbor element in the topology, N is the number of considered modes. The number of layers increases linearly with the number of elements considered. After each layer, the GeLU activation function is applied, except in the final layer, where a linear activation is used.

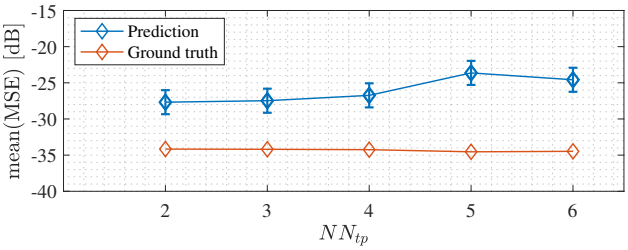

Figure 5.13: Mean MSE comparison over the test set: (red) between the full-wave simulated pattern and the reconstructed pattern using ground truth coefficients; (blue) between the full-wave simulated pattern and the reconstructed pattern using NN-predicted coefficients, with vertical lines indicating the standard deviation of the corresponding model, NN_{tp}.

ber of neighboring elements varies by topology, separate models are developed for each case, ensuring accurate predictions. The trained models predict the spherical mode coefficients, $\hat{\mathbf{c}}$ in (5.8), of the AUT. Using a pre-calculated $\mathbf{Y}$, the AUT's field is reconstructed from the predicted coefficients. As discussed in Section 5.3.2, the number of significant modes is determined as $L^2 = 169$, though further reduction is possible by eliminating modes with near-zero values without compromising the field reconstruction performance. The optimal number of modes is selected based on dataset analysis to balance accuracy and efficiency. The reconstruction error is quantified using the MSE:

$$MSE = 10\log\left(\frac{1}{N_s^2}\sum^{N_s}(|\mathbf{e}| - |\hat{\mathbf{e}}|)^2\right) \tag{5.11}$$

where N_s is the total number of samples of the vector $\mathbf{e}$, which comprises the full-wave simulated electric field of the chosen element in the far-field region that is generated by the commercial full-wave simulator CST, $\hat{\mathbf{e}}$ is the corresponding reconstructed pattern in vector form as given in (5.10).

The relation between the MSE, the chosen absolute threshold value for the coefficients, and the number of modes was investigated in each dataset to find the optimal number of modes. As each topology comprising a different number of elements shows a similar behavior, Fig. 5.11 illustrates this relation for the 4-element dataset comprising 4000 randomly generated topologies. The mean MSE and the number of modes are related inversely. With an increase in the threshold, the mean MSE increases, while the number of modes decreases (represented by the two lines in Fig. 5.11). The optimal trade-off can be identified at the point where a noticeable change occurs upon manual inspection, which, in this case, is observed around 81 modes.

Since the estimation space consists of 81 complex coefficients, a relatively simple network can be used for prediction. The model begins with a 1D convolutional layer with 16 kernels to encode spatial information, followed by a fully connected layer that outputs an 81×2 matrix (real and imaginary parts). As the number of elements in the topology increases, the network depth grows to handle the increased prediction complexity. Initially, four fully connected layers are used after the convolutional layer, with neurons increasing up to 162. The number of layers and neurons was fine-tuned heuris-

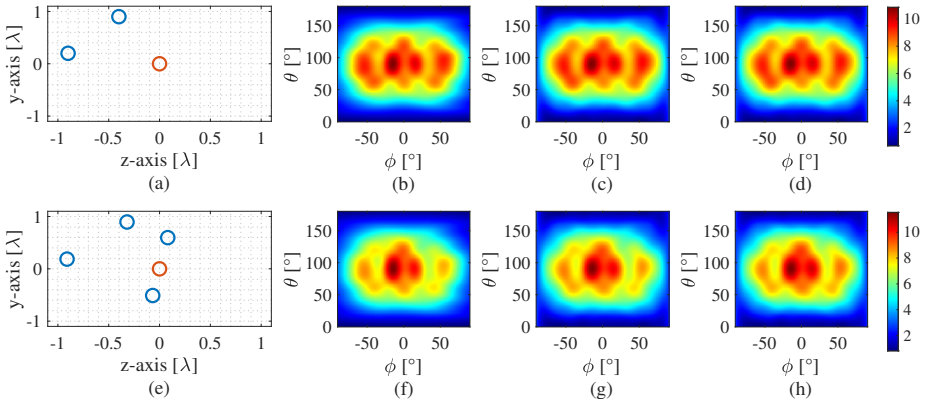

Figure 5.14: Example topology results for the 2- (K = 3-element topology) and 4-element neighboring (K = 5-element topology) cases are shown (electric fields in linear scale). (a) and (e) illustrate the array topologies, where the red circle represents the AUT and the blue circles represent the neighboring elements; (b) and (f) display the full-wave simulated patterns of the AUT for each case, respectively; (c) and (g) show the reconstructed patterns using the ground truth coefficients; (d) and (h) depict the reconstructed patterns using the NN-predicted coefficients.

tically for each model. To prevent overfitting, dropout layers were introduced when the fully connected layers increased to six for the 5- and 6-element cases. Figure 5.12 illustrates an example architecture, where K represents the maximum number of neighboring elements, and N is the number of utilized modes, set to 81 in this study.

The network is trained using the ADAM optimizer [87] with the default hyperparameters (η=0.001, β_1=0.9, β_2=0.999, ϵ=1e-7) and the MSE between the estimated and the true coefficients as the loss function. Once the coefficients are predicted, the field can be reconstructed by using (5.10).

5.3.4. PREDICTION RESULTS

For this study, five NN models have been developed, each corresponding to a specific number of neighbor elements. Models for cases with 2 to 6 elements have been designed, with the circular region depicted in Fig. 3.8 constrained to λ, as discussed in Section III. As for the single element, the isolated element pattern is assumed due to the negligible effect of the single element on the AUT. For each case, 4000 quasi-randomly distributed data were generated with CST. These far-field patterns were then processed into the coefficients of the spherical wave modes. From this dataset, 80% are chosen as training; the rest are divided equally for the validation and test sets.

Figure 5.13 presents the mean MSE comparison for two cases: (1) between the full-wave simulated pattern and the reconstructed pattern using ground truth coefficients, and (2) between the full-wave simulated pattern and the reconstructed pattern using NN-predicted coefficients. While the resulting mean errors remain below -25 dB for most of the cases, indicating high accuracy, the standard deviation of the predictions remains within 2 dB, as shown in the same figure. As the number of elements exceeds four, the prediction errors increase due to the growing complexity of the problem. However, this

error can be mitigated by incorporating additional data.

Figure 5.14 shows an example of 2- and 4-element cases, highlighting the impact of additional neighboring elements on the EEP of the AUT. In both cases, the trained models successfully predict the coefficients, which allow for the reconstruction of the field with high accuracy.

5.3.5. CONCLUSION

This section presented a spherical wave expansion framework for predicting EEPs in aperiodic antenna arrays. By decomposing farfield responses into a compact set of spherical harmonic modes, the method enables efficient and scalable representation of EEPs while preserving key physical characteristics of the radiation behavior. The proposed NN architecture predicts the modal coefficients directly from the array topology, allowing accurate field reconstruction. The approach supports variable array configurations and maintains robustness across different element counts and spatial arrangements. These capabilities make the method well-suited for practical design scenarios where MC effects must be captured efficiently.

5.4. CONCLUSIONS

This chapter introduces a novel ensemble learning framework for accurate and efficient prediction of EEPs under varying MC effects, with a focus on reducing data dependency. The approach combines a two-stage neural network model for direct EEP prediction with a constrained IDM-based model, where neural networks predict the dipole excitations for reconstructing the fields. A stacked generalization scheme is used to intelligently merge the strengths of both models, improving overall prediction accuracy while avoiding manual ensembling or averaging errors.

Additionally, spherical wave expansion was employed as a compact and scalable representation for EEPs, allowing NNs to learn the relevant coefficients even in complex array configurations. By using spherical waves, EEPs can be predicted more effectively, reducing the sensitivity of the model to errors from a high condition number in the IDM. Furthermore, the proposed framework effectively captures the localized variations caused by MC effects by designing separate models tailored to different numbers of neighboring elements.

6

APPLICATIONS IN ACTIVE PHASED ARRAYS: DESIGN AND DIAGNOSTICS

This chapter focuses on two distinct applications of machine learning (ML) in active array systems: array design and fault diagnostics. The first part introduces a mutual coupling (MC)-aware synthesis method for irregular MIMO radar arrays, where a neural network (NN) predicts embedded element patterns (EEPs) based on spherical harmonics. This model is integrated into a particle swarm optimization (PSO) framework to improve pattern accuracy across multiple beam directions. The second part presents an NN-based approach for detecting faulty elements using sparse, amplitude-only far-field measurements. Validated on a 64-element active array, the method achieves high localization accuracy and outperforms conventional heuristic techniques. These applications demonstrate how ML can effectively support both forward and inverse problems in pre- and post-manufacturing stages of the active arrays.

Parts of this chapter have been published in:

N. B. Onat, T. Dash, A. Yarovoy and Y. Aslan, "Machine Learning-Assisted Prediction of Spherical Harmonics and Application to the Synthesis of Accurate MIMO Radar Patterns," in IEEE Antennas and Wireless Propagation Letters, under revision.

A. Kannan, **N. B. Onat**, M. S. A. Yarovoy and Y. Aslan, "Detection of Faulty Elements From Sparse Far-Field Data in Active Phased Arrays via Machine Learning," in IEEE Open Journal of Antennas and Propagation, doi: 10.1109/OJAP.2025.3542185.

6.1. MACHINE LEARNING-ASSISTED SYNTHESIS OF ACCURATE MIMO RADAR PATTERNS

6.1.1. INTRODUCTION

Irregular multiple-input multiple-output (MIMO) antenna topologies have been proposed for high-resolution imaging purposes for various sensing systems, such as airborne radars [88], automotive radars [89] and (near-field) radar imaging [90, 91]. Layout synthesis techniques are based on deterministic methods (FFT-based) [92], global optimization [93, 94], or convex optimization [95], with a goal function on the side lobe levels of the multiple input, multiple output radar pattern (MIMO). Due to the complexity and non-linearity of the problem, the existing algorithms ignore the effect of MC between the antenna elements (with the assumption of isotropic radiators) and the resulting variations in the EEPs are ignored. This leads to significant deviations from the predicted SLLs by the optimizers [96], and the sensing performance may considerably degrade in real-life operation [97]. In this chapter, an accurate (i.e., MC-aware) synthesis of MIMO radar patterns has been proposed for the first time by utilizing the novel EEP prediction technique based on the theory of spherical harmonics introduced in the previous chapter.

6.1.2. PROBLEM FORMULATION

This chapter is based on the problem formulation, AUT and the prediction technique that are introduced in Section 5.3.

MIMO RADAR TOPOLOGY

As discussed previously, this work considers a K-element irregularly spaced pin-fed circular patch antenna array operating at a center frequency of 10 GHz. Figure 3.8 illustrates an example array topology, and the key design parameters are provided in Table 5.3. Furthermore, the far-field virtual array pattern of a MIMO radar is derived by the convolution of the transmitter and receiver topologies, which are placed on the y-z plane, and can be found as [95]:

$$E_M(\theta,\phi) = \sum_{k_t,k_r=1}^{K_t,K_r} E_{k_t}^{TX}(\theta,\phi) E_{k_r}^{RX}(\theta,\phi) \mathrm{e}^{\mathrm{j}2\pi/\lambda(y_{k_r}^{k_t}\sin\theta\sin\phi + z_{k_r}^{k_t}\cos\theta)},$$

where $E_{k_t}^{TX}(\theta,\phi)$ and $E_{k_r}^{RX}(\theta,\phi)$ are the EEP of the k_t-th and k_r-th element in TX and RX topologies, respectively, where the EEPs of the TX topology are taken as isolated element pattern (IEP) due to the high sparsity. Furthermore, $y_{k_r}^{k_t}$ and $z_{k_r}^{k_t}$ are superposition of the TX and RX positions and can be found as $y_{k_r}^{k_t} = y_{k_t} + y_{k_r}$ and $z_{k_r}^{k_t} = z_{k_t} + z_{k_r}$, respectively. It is worth to note that (6.1) assumes that the array does not utilize any amplitude tapering.

6.1.3. OPTIMIZATION FRAMEWORK FOR MIMO RADAR

Particle Swarm Optimizer (PSO) [98] has been used to carry out the optimization routine for the synthesis problem. During the optimization process, the location of the array elements in TX and RX is simultaneously optimized to minimize the maximum side lobe

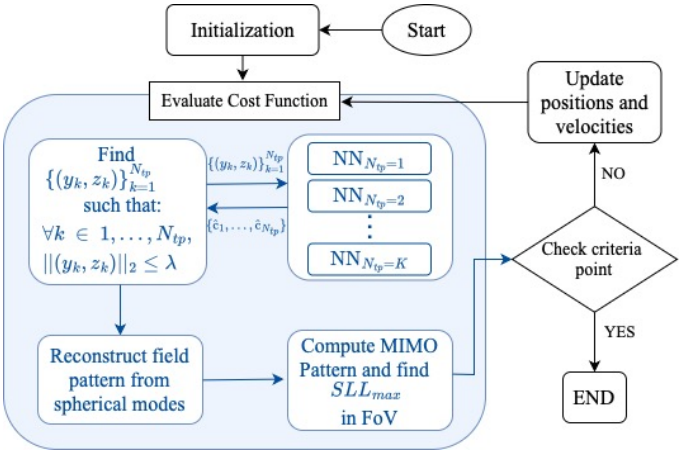

Figure 6.1: Utilized PSO framework where NN models are integrated into MATLAB. During cost function evaluation, the NN models are called for each element depending on the number of neighbor elements in the defined circle, N_{tp}, to predict the spherical wave coefficients, $\hat{\mathbf{c}}$. The predicted coefficients are further used to reconstruct the EEP of the AUT. After predicting each EEP for a given topology, the MIMO virtual pattern is calculated, and the maximum SLL is found for each candidate solution.

Table 6.1: Maximum SLL Comparison Between NN-Assisted MIMO Topology Optimization and Full-Wave Simulation of the Optimized Pattern

Steering (θ_0, ϕ_0)	(0°,0°)	(0°,30°)	(0°,-30°)	(30°,0°)	(-30°,0°)
$max(SLL_{\text{NN}})$ [dB]	-18.03	-16.23	-16.03	-16.03	-16.09
$max(SLL_{\text{fw}})$ [dB]	-17.23	-16.67	-16.17	-15.56	-15.58
$max(SLL_{\text{IEP}})$ [dB]	-17.10	-15.36	-15.36	-13.10	-13.10

level (SLL) in the defined field of view (FoV) for a multiple-beams scenario. Figure 6.1 illustrates the block diagram of the utilized PSO.

The approach proposed in Section 5.3.3 is integrated into the optimizer to achieve MC-aware synthesis. Each NN model is trained using TensorFlow in Python. For optimization, the trained models are integrated into MATLAB, leveraging its computational capabilities. In this way, the EEP of the elements are obtained in every iteration to compute the virtual array pattern of each candidate solution.

6.1.4. RESULTS

This section first discusses the results of the NN models proposed for the prediction of the spherical coefficients and then the utilization of these models for the MIMO radar topology comprising a 6-element TX and an 8-element RX.

EEP PREDICTION VIA SPHERICAL MODES

For this study, five NN models have been developed, each corresponding to a specific number of neighbor elements. Models for cases with 2 to 6 elements have been de-

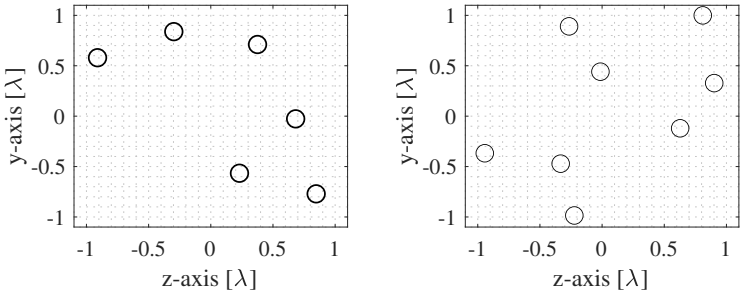

Figure 6.2: Optimized MIMO radar topologies for multi-beam application where circles indicate the element locations. (a) TX topology with 6 elements; (b) RX topology with 8 elements.

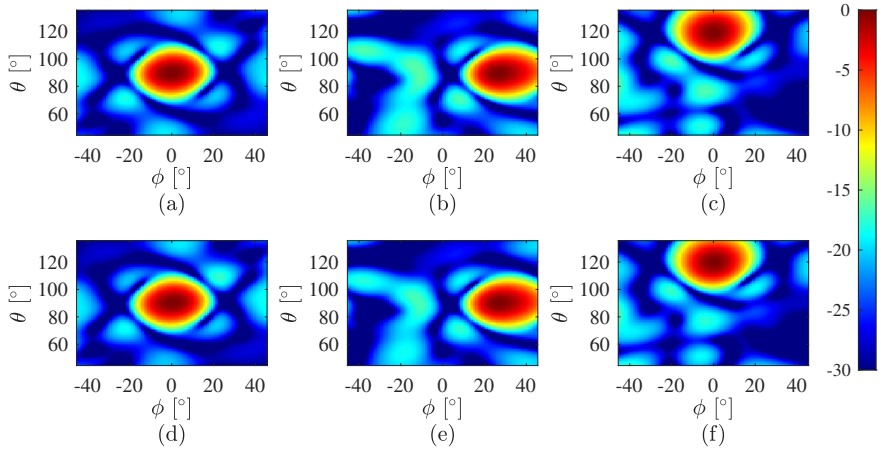

Figure 6.3: Optimized far-field patterns for all steering angles in the FoV and comparison with full-wave simulations (normalized electric fields in [dB]). Top row is the optimized patterns with predicted EEPs and bottom row is the full-wave simulations. (a) and (d) are the boresight; (b) and (e) are steered by $(\theta_o = 0°, \phi_o = 30°)$; (c) and (f) are steered by $(\theta_o = 30°, \phi_o = 0°)$.

signed, with the circular region depicted in Fig. 3.8 constrained to λ, as discussed in Section 5.3. As for the single element, the isolated element pattern is assumed due to the negligible effect of the single element on the AUT. For each case, 4000 quasi-randomly distributed data were generated with CST. These far-field patterns were then processed into the coefficients of the spherical wave modes. From this dataset, 80% are chosen as training; the rest are divided equally for the validation and test sets. The results and comparisons for this section are already given and discussed in Section 5.3, where Fig. 5.13 and 5.14 illustrate the MSE results and example topologies, respectively.

MUTUAL COUPLING-AWARE MULTI-BEAM MIMO RADAR TOPOLOGY OPTIMIZATION

The trained models in the previous section were integrated into the PSO to achieve accurate MIMO radar topology for multi-beam applications. The element positions of the TX and RX topologies comprising 6 and 8 elements, respectively, are optimized simultaneously. Furthermore, the FoV is limited to $45^\circ \leq \theta \leq 135^\circ$ and $-45^\circ \leq \phi \leq 45^\circ$. For this work, 5 different steering angle combinations are considered: (θ_o, ϕ_o) = [(0°,0°), (0°,30°), (0°,−30°), (30°,0°), (−30°,0°)].

Table 6.1 presents the optimized topology results for the maximum SLL in the FoV for each beam and Fig. 6.2 shows the optimized TX and RX topologies. The proposed optimization achieved an average maximum SLL of -16 dB, and the full-wave simulation results show good agreement with the proposed methodology, whereas the array patterns generated with the IEP remain unreliable as the Table 6.1 shows. Furthermore, Fig. 6.3 illustrates the far-field pattern of the corresponding virtual array for all steering angles, compared to the full-wave simulated pattern. As observed in the mentioned figure, the error in the predicted patterns appears in some edge regions, suggesting that the prediction accuracy for the corner elements could be improved further.

6.1.5. CONCLUSION

A novel NN-based EEP prediction method using spherical harmonics, enabling accurate reconstruction while considering MC effects. The approach was integrated into a PSO framework for MIMO radar topology optimization, effectively minimizing maximum SLL for multi-beam case. Through the synthesis of an irregular MIMO radar topology comprising 6-element TX and 8-element RX, it is demonstrated that the proposed method offers a robust and efficient solution for MC-aware array synthesis, including multiple scanned beams in a given field of view.

6.2. DETECTION OF FAULTY ELEMENTS FROM SPARSE FARFIELD DATA VIA MACHINE LEARNING

6.2.1. INTRODUCTION

In complex antenna systems, random failures in the electromagnetic radiators, ICs or IC channels may occur while the array is manufactured or assembled, or during in-field operation. The failures may lead to undesired changes in the radiation pattern, with significant effects on the gain, beamwidth, SLLs, null positions and depths [99]. Before replacing any components or taking any action to compensate for the pattern changes [100, 101], it is crucial to identify the locations of the failed elements. The ambition is to achieve such a diagnosis in almost real-time and both in post-manufacturing and in-field scenarios, which makes the problem challenging. Besides, the IC nonlinearities and mutual coupling effects [102, 103] in practical arrays bring additional difficulties in modeling and solving this inverse problem.

One approach for fault detection in active antennas is to monitor the temperature across the array, where low temperatures (relative to the operating temperature) indicate failure. At the IC level, diagnosis can be done by placing temperature sensors inside each multi-channel IC [104]. This increases the cost, size and consumption of the ICs, and detects only the number of fails among a group of antenna elements, without ac-

curate identification of the failed elements. For element-level diagnosis, the infrared thermography technique has been proposed [105, 106], which visualizes the strength of electric fields through the temperature changes on an absorption screen in front of the array. In this method, the screen causes unwanted perturbation on the radiated electromagnetic waves, while the resolution of thermal images is too low to detect failures in high-frequency antennas with small physical inter-element spacing [107]. Modulation of input power helps improve the resolution [108], yet it brings additional system cost and complexity.

Another competitive and widely studied approach is to monitor the EM fields over-the-air (OTA), either in the close proximity of the array (i.e., near-field, NF), or at farther distances (i.e., far-field, FF) [109]. In NF, a movable sampling probe is used to locate the defects [110]. Depending on the array size and sampling strategy, the data collection time for a fail scenario can reach up to several hours [111]. Alternatively, sparse source reconstruction techniques can be utilized to reduce the required number of samples [112]. However, the measurement system complexity, potential alignment and probe coupling errors and long time of pattern data collection and processing pose challenges in array diagnosis at NF. This motivates the utilization of FF in high-frequency antenna diagnosis [113, 114] for which the OTA measurement distance is practically feasible. For complexity and cost reduction in the FF measurements, amplitude-only data collection [115] and sparse sampling [116, 117] have been proposed in the literature.

The measurement techniques are complemented by various algorithms solving an optimization problem with the goal of maximizing the failure detection success ratio [118]. The examples include deterministic techniques such as the Matrix Pencil Method [119], Convex Optimization [120] and evolutionary algorithms such as the GA [114, 115, 118]. Among them, the GA-like algorithms fit well to the problem due to the binary nature of the unknowns (i.e., on-off state of the elements). However, their convergence can be very slow, especially in the case of a large search space [121].

Recently, several ML solutions have been proposed for real-time antenna array diagnosis [25, 26]. Nevertheless, the algorithms have only been developed for the full-wave simulated and densely sampled FF data and only for small-sized (i.e. 3×3, 4×4) arrays. In a practical array, the active components bring additional non-linear changes in each IC channel response, thus on the radiation patterns, due to load pull effects, manufacturing tolerances, and temperature variations [122, 123]. Such effects have never been studied in the ML-oriented fault diagnosis literature. There is also a lack of knowledge in the application of ML in large-sized (e.g., 8×8) array diagnostics. Besides, ML-based array diagnosis has never been integrated with sparse pattern sampling, which is a must for a reasonable data collection time and for compliance with in-field operation.

Towards these aims, this section proposes a novel ML-assisted real-time fault detection technique that uses amplitude-only sparse FF sampled data. The IC nonlinearities, as well as mutual coupling effects, are taken into account for the first time in the formulation and solution of this inverse problem. A practical 64-element IC-integrated phased array prototype (at 26 GHz) from NXP Semiconductors and TNO [42, 123, 124] is used with the fixed multi-probe measurement system at TU Delft (The Antenna Dome) [125, 126] for a fully-connected neural network (FCNN) development and performance demonstration. The GA optimization is used for benchmarking, and the superior failure

detection capability of the proposed ML methodology is shown.

6.2.2. PROBLEM FORMULATION AND FAULT FINDING METHODOLOGIES

PROBLEM FORMULATION

The fundamental FF equation of a uniform planar array with N elements can be written as:

$$F(\theta_i,\phi_i) = \sum_{n=1}^{N} E_n(\theta_i,\phi_i)\, w_n e^{\mathrm{jk}(x_n \sin\theta_i \cos\phi_i + y_n \sin\theta_i \sin\phi_i)} \tag{6.1}$$

where the embedded element pattern of the n-th element is indicated as $E_n(\theta_i,\phi_i)$ with the corresponding i-th sampling point (θ_i,ϕ_i) for the spherical observation angles θ and ϕ. Furthermore, k is the wavenumber in free space, $(x_n,\ y_n)$ denotes the position, and w_n is the complex excitation coefficient of the n-th element.

To mimic the element failures, the absolute value of the n-th element weight given in (6.1) is presumed to be 0 ($|w_n| = 0$) for a certain number of fails, which is assumed to be known by the measured power level on the broadside. Then the ultimate goal of this work is to correctly predict the locations (x_n, y_n) of all elements with $|w_n| = 0$. This is an inverse (source finding) problem, which maps a measured pattern with faulty elements to the functioning array layout. As the non-linear IC behavior and coupling effects on the IC-antenna interfaces are inevitable in the active phased arrays, the measured data (with additional errors from the measurement setup) deviates from the theoretical model in (6.1). The practical measured pattern can be represented in a compact form as follows:

$$F_{\mathrm{ms}}(\theta_i,\phi_i) = F(\theta_i,\phi_i) + \xi_A(\theta_i,\phi_i) + \xi_D(\theta_i,\phi_i), \quad \text{for} \quad i = 1,\ldots,M \tag{6.2}$$

where M is the total number of sampling points considered in the measurement setup, $\xi_A(\theta_i,\phi_i)$ and $\xi_D(\theta_i,\phi_i)$ denote the noise-like effects introduced by the AUT and the measurement setup, respectively. As the above-mentioned noise-like effects behave in a highly non-linear fashion, with deterministic and random components and with dependency on environmental conditions, accurate modeling of them is almost impossible. Several studies consider statistical error modeling in active phased arrays [127, 128], which will fail to represent a given AUT pattern behavior accurately. Therefore, the most viable option is to collect a large amount of pattern data by varying the fail scenarios randomly and modeling such effects by utilizing ML-based techniques.

In line with common practice, the FF pattern presented in (6.2) can be measured densely with a one-degree interval both in θ and ϕ. This approach would enable capturing the pattern variations very accurately in different element fault scenarios; however, there will be a need for continuous measurements with mechanical control, which is complex and time-consuming in collecting the pattern data. On the other hand, the nodes in a sparse and fixed pattern sampling setup (with a relatively low value of M) for fast data collection cover a particular angular region with sparsely distributed nodes. Despite the increased resolution with the number of sampling nodes, there are practical limitations that come from the node sizes and coupling between the nodes [125, 126]. This, in turn, significantly reduces the spatial resolution of the FF pattern. To capture the pattern changes, it is then important that the nodes are well-distributed over the

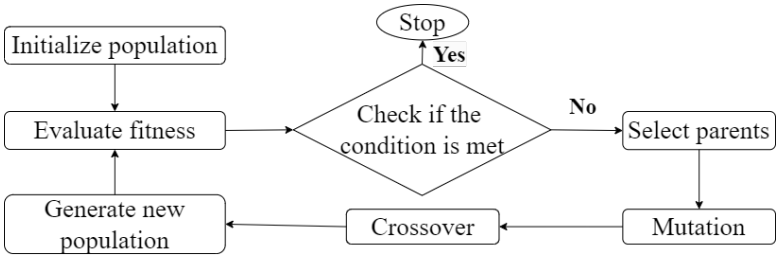

Figure 6.4: Flowchart of the Genetic Algorithm (GA).

sidelobe region and not aligned with the nulls of the pattern. Regarding the node distribution, a good trade-off between complexity and capturing pattern variability over all subarrays is to use a minimal angular spacing that is larger than the approximate beamwidth of the antenna array (i.e., wavelength divided by the largest antenna dimension, in radians). Due to the randomized nature of our problem and the non-linearities, there are no fixed null positions to be considered in the pattern sampling strategy. The receiver positions can then be decided based on standard circular, triangular or hexagonal sampling techniques, and the effect of the total number of receivers can be studied.

In this work, the goal is to minimize the error between the ground truth pattern, $F_{\text{ms}}(\theta_i, \phi_i)$, and the predicted pattern, $\overline{F}_{\text{ms}}(\theta_i, \phi_i)$, under the test scenarios with randomly failed elements. A heuristic approach as a benchmark method and a novel ML approach are proposed to achieve this aim. A geodesic dome with receivers located on hexagonal sampling points is utilized for pattern data collection.

HEURISTIC APPROACH FOR BENCHMARKING: A GLOBAL OPTIMIZER

Global optimizers (GOs) are algorithms designed to find the best possible solution (global optimum) to a problem across the entire search space rather than getting trapped in local optima. GOs, such as genetic algorithm (GA) [118], simulated annealing (SA) [129], and particle swarm optimization (PSO) [98], explore the search space more broadly, balancing exploration and exploitation to ensure a comprehensive search for the optimal solution. Therefore, they have been widely exploited in array synthesis and design problems [130][131], where real-time implementation is generally not considered crucial.

The GA is an evolutionary algorithm inspired by the principles of natural selection, iteratively evolving candidate solutions to achieve an optimal result of the given problem [132]. With its many examples in the fault finding literature (e.g. [114, 115, 118, 121]) due to its effectiveness with complex objective functions and the binary nature of the considered problem, the GA algorithm is chosen as the benchmarked heuristic approach in this paper.

As Fig. 6.4 illustrates, the algorithm begins by generating a population (consisting of 0s and 1s, representing the faulty and working elements, respectively), and selecting the fittest individuals from the initial population based on the defined fitness function. These selected individuals undergo crossover, where their genetic information is combined, and mutation, where random changes are introduced to create new offspring. This new generation replaces the old population, and the process repeats. Over successive generations, these update rules drive the population toward increasingly optimal

solutions.

PROPOSED APPROACH: NEURAL NETWORKS (NNS)

ML employs data-driven methods to make predictions or decisions, and it is widely applied in various fields. ML techniques are also used in global optimization tasks such as array diagnosis, pattern recovery, and parameter estimation. The formulation of the problem, organization of data, application of algorithms, and validation of results are crucial steps in this process. Depending on the problem type, various ML methods can be utilized, including neural networks (NNs) [133], support vector machines (SVMs) [134], and others. In EM applications, machine learning is particularly effective for capturing and modeling complex, non-linear input-output relationships, which are common in EM field interactions and system behavior with IC-antenna integration. Particularly, NNs, when designed with an appropriate architecture, trained with sufficient data, and optimized using reliable techniques, can effectively approximate these relationships, enabling accurate modeling and fast prediction in complex EM scenarios.

In this work, the approach begins by incorporating the array factor equation into the loss function, ensuring that the model aligns with the basic EM principles. Since the collected measurements cannot be mathematically defined in a closed-form equation as they include multiple non-linear effects and setup errors, a purely data-driven model is eventually employed. Such a model is particularly well-suited for capturing the complexity of the highly intricate measurement data, which cannot be modeled by traditional EM-based methods. A fully connected NN is especially well-suited for problems where every input feature may influence every output, making it a strong choice for capturing complex, global patterns in the measured pattern data.

The proposed NN architecture consists of 10 layers, with increasing density tailored to output requirements. Hidden layers process and explain neuron behavior, while activation functions handle non-linearization. A probability threshold is set for class assignment in binary problems, where higher thresholds reduce false positives and lower thresholds increase false detections. Batch normalization is applied for training stability, and dropout layers prevent overfitting. The network size is kept small to achieve the desired performance. A flowchart of the proposed architecture is illustrated in Fig. 6.5. The fully connected network provides the weights of the array elements $[y_1, ..., y_N]$ in binary form, where 0s represent failed elements and 1s represent working elements. The initial layers have ReLU activation and the final layer uses Sigmoid activation as the desired output is binary.

6.2.3. AUT AND THE ANTENNA DOME

The Antenna Dome, shown in Fig. 6.6, is a three-dimensional (3D) array pattern acquisition setup developed at TU Delft [125, 126, 135] which removes the need for scanning equipment and heavily reduces the characterization time, at the expense of decreased pattern resolution. It has a geodesic skeleton that can be scaled using different profiles, enclosed in absorbing mounted panels to mimic an anechoic environment. In its current implementation [135], it is configured using 36 fixed dual-polarized sensing nodes. The distance between the AUT and the sensing nodes is $r = 75$ cm. The nodes cover an angular region from $\theta = 0^o$ (broadside) to $\theta = 64^o$ in the spherical coordinate system

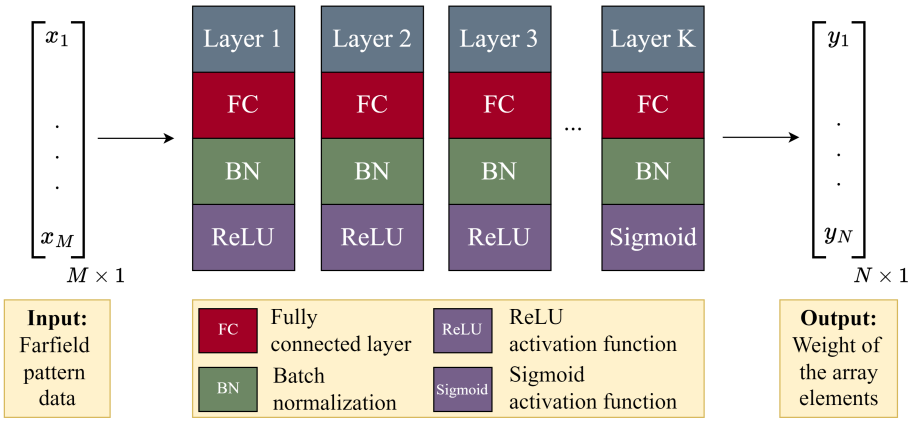

Figure 6.5: Proposed fully-connected NN architecture for detection of the faulty elements. The maximum number of layers, K, is initially defined as 10 for the 8-element failure case. Note that this number depends on the number of active sensor nodes, M.

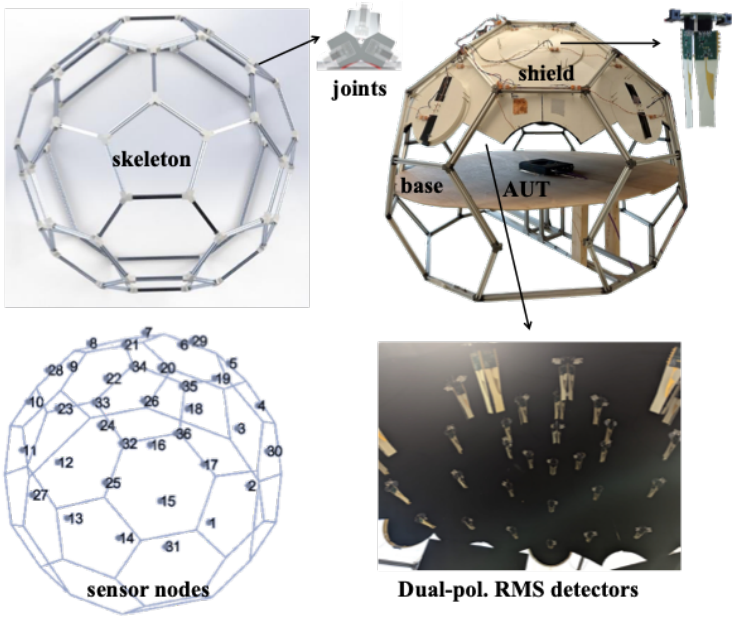

Figure 6.6: The Antenna Dome setup [125, 126, 135]: (top left) geodesic skeleton with aluminum profiles, (top right) shielded skeleton including RMS detectors and AUT, (bottom left) sensing node configuration and numbering, (bottom right) RMS detectors inside the dome.

with a sparse distribution.

As illustrated in Fig. 6.7, the sensing node is a broadband Vivaldi antenna operating from 22-51 GHz, and an RMS power meter is directly integrated with the antenna with a 12-bit digitizing unit. This node is then connected to a readout board, which can

locally process the received power and then send it to a computer. Each sensing node provides about 40 dB dynamic range (RMS detector). The dynamic range is obtained at the detector board and is independent of the number of nodes.

In this work, we utilize the Antenna Dome to collect the sparse power pattern (for a pencil beam on the broadside) of our calibrated AUT, the 64-element 26 GHz active uniform array described in Appendix A.2, while randomly turning off a pre-determined number of IC channels. The mentioned sparse power pattern is measured with the sparsely distributed receiver nodes in the Antenna Dome, where the spherical observation angle mapping of these 36 nodes is illustrated in Fig. 6.8. The fast-measured data is then used for testing the performance of the benchmarked GA algorithm, and for training and validating the proposed ML algorithm in fault diagnosis.

6.2.4. THEORY-BASED TRAINING AND PREDICTION

To utilize the physics behind the problem, to observe the mutual coupling effects to some extent, and to make a transition to the data-driven models, this section considers the full-wave simulated antenna pattern data in the 64-element array, yet without integration of the ICs. The simulated embedded element pattern (EEP) of each element is included in the pattern formulation, which leads to the theory-based training and prediction. While the NN model incorporates the FF equation, given in (6.1), into its loss function to enhance accuracy and generalization, having a theory-based step also provides a fair comparison with the GA, as it requires calculating the cost function for all candidate solutions during each iteration.

In the GA, the MSE is used as a cost function to quantify the error and is employed as a fitness function:

$$\rho = \frac{1}{M^2}\sum_{i=1}^{M}\left(\left|F(\theta_i,\phi_i)\right| - \left|\overline{F}(\theta_i,\phi_i)\right|\right)^2 \tag{6.3}$$

where M is the total number of samples which is 36 in this case, $F(\theta_i,\phi_i)$ is the simulated ground truth pattern and $\overline{F}(\theta_i,\phi_i)$ is the predicted pattern. Tuning of the GA parameters

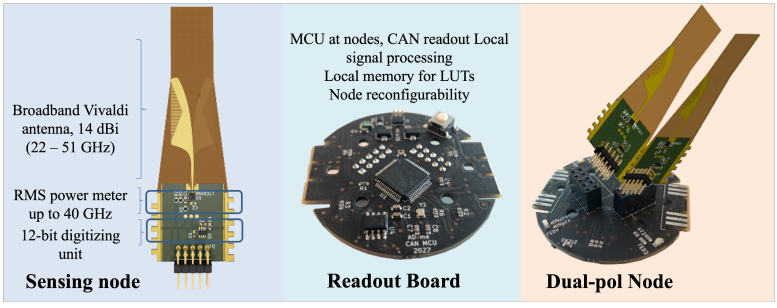

Figure 6.7: RMS detectors in the antenna board [125, 126, 135]: (left) Broadband Vivaldi antenna, 14 dBi (22 – 51 GHz), RMS power meter operating up to 40 GHz, 12-bit digitizing unit, (middle) distributed MCU, i.e., at every sensing node, providing local signal processing and memory for LUTs, CAN transceiver embedded on board, (right) illustration of the interface via DIL connectors of the orthogonally assembled sensing nodes with the readout board.

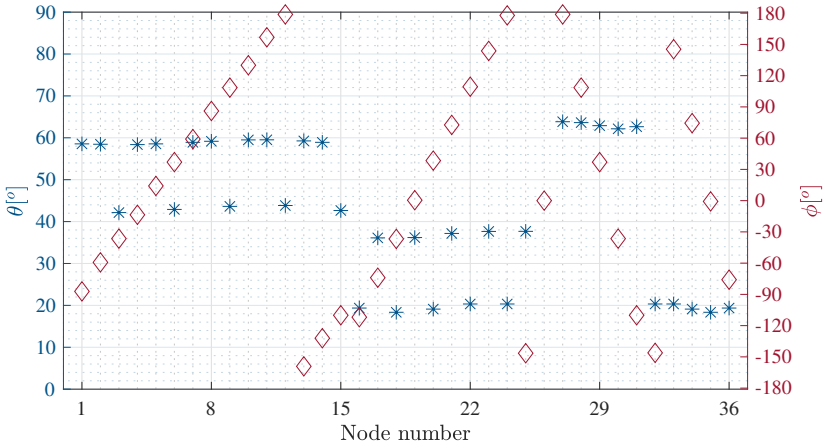

Figure 6.8: Spherical observation angle mapping of sparsely distributed 36 nodes in the Antenna Dome where the colors red and blue indicates the angles ϕ and θ, respectively.

Table 6.2: GA Parameter Settings for the Element Failure Prediction

Parameter	Value	Parameter	Value
Population size	50	Crossover probability	0.4
Number of iterations	1000	Crossover type	single-point
Number of realizations	50	Mutation probability	0.1

Table 6.3: Simulation results for theory-based training and prediction

nFail	Method	μ_{corr}	σ_{corr}	n_{corr}^{max}	n_{corr}^{min}	$\mu_{\Delta d}$	$\sigma_{\Delta d}$
8 El.	GA	3.78	1.06	6	1	2.03	0.53
	ML	7.42	0.57	8	6	0.56	0.60
4 El.	GA	1.94	0.90	4	0	1.69	0.69
	ML	3.39	0.55	4	3	0.71	0.72
2 El.	GA	1.23	0.66	2	0	1.27	1.13
	ML	1.71	0.46	2	1	0.36	0.65

is carried out to achieve the optimum solution to the problem. The optimized parameters are shown in Table 6.2.

As for the proposed NN, the ADAM (adaptive moment estimation) is utilized as an optimizer and binary cross entropy (BCE) loss is chosen as a loss function where the model itself encourages higher probabilities for working and lower for failed elements. Furthermore, a custom penalty function is created to penalize the network when it mispredicts the number of failed elements.

This study analyzes three distinct failure scenarios to validate the proposed methodology. Following the standard fail ratios from the literature [115, 118], an 8-element fail-

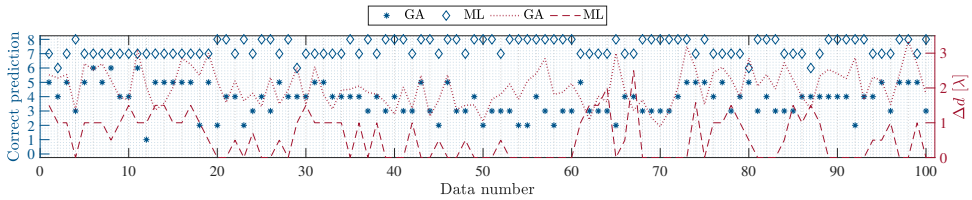

(a)

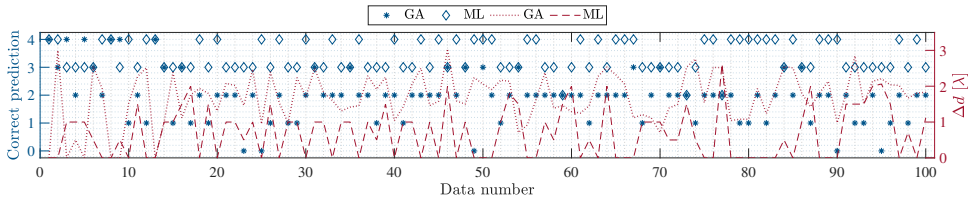

(b)

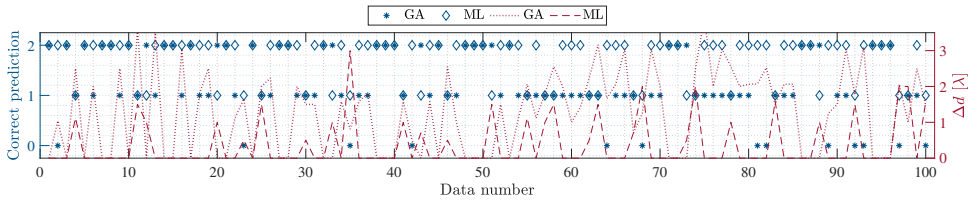

(c)

Figure 6.9: Results for the theory-based prediction from 36 sampling points of FF simulation data and comparison with the GA as a benchmark methodology over the validation set. The left y-axis (blue) represents the number of correct predictions by the utilized methodologies and the right y-axis (red) describes the distance between the mispredicted element and its ground truth. (a) 8-element failure case; (b) 4-element failure case; (c) 2-element failure case.

ure is initially considered, as it is expected to produce a more significant disturbance in the pattern. Subsequently, 4- and 2-element failures are investigated, where the resulting disturbances are anticipated to have a reduced impact on the pattern. It is worth to note that the number of faulty elements is assumed to be known by the measured power level. The methodologies are tested with 100 different fail scenarios randomly chosen in each case.

Figure 6.9(a) illustrates the results for 8-element failure over the validation set where the markers blue diamonds and stars represent the number of correctly predicted failed elements by ML and GA, respectively. Two red dashed lines represent the distance between the false prediction and the ground truth of the corresponding mispredicted element. As Table 6.3 shows, the proposed NN methodology achieves an average of 7.42 correct predictions (μ_{corr}). Additionally, it successfully identifies the location of at least 7 out of 8 elements with 96% accuracy on the validation set. On the other hand, the mean number of correct predictions (μ_{corr}) for the GA remains below 4, with a maximum cor-

rect prediction (n_{corr}^{max}) of 6 and a minimum correct prediction (n_{corr}^{min}) of 1 for the same case study due to the low number of sampling points and stochastic search nature of the GA. This significant variation in prediction accuracy is further reflected in the high standard deviation of correct predictions (σ_{corr}) across the validation set.

As the number of faulty elements decreases, the disturbances in the FF pattern become less noticeable, particularly with the 36 data points, leading to a slight reduction in prediction accuracy, as shown in Figures 6.9(b) and 6.9(c). Despite this, the NN maintains a high average correct prediction rate of 3.39 out of 4, with a low standard deviation, σ_{corr}. In contrast, the GA significantly exhibits a lower μ_{corr} and a higher σ_{corr} due to the stochastic nature of the search algorithm. This trend persists in the 2-element failure case. Although prediction accuracy may decrease with fewer faulty elements, the proposed NN method can still predict the location of the misidentified faulty element within an average of a single wavelength (λ) region, as indicated by $\mu_{\Delta d}$ in Table 6.3, with minimal deviation of $\sigma_{\Delta d}$.

Figure 6.10 illustrates the behavior of the average μ_{corr} versus average Δd, along with their respective standard deviations, as a function of the number of faulty elements. While the ML demonstrates consistent performance across all numbers of faulty elements, the GA exhibits significant fluctuations with varying numbers of faulty elements, leading to reduced reliability.

6

6.2.5. THEORY-ENHANCED LEARNING AND PREDICTION

The measurements collected cannot be expressed mathematically in a closed-form equation due to the presence of multiple non-linear effects brought by the ICs, IC-antenna integration, and the measurement setup, as described in (2). To ensure that the proposed model adheres to the underlying physics of the problem, the previously presented theory-based model is further trained with the measured data. By blending data-driven learning with the FF equation, the theory-enhanced trained model offers a powerful ap-

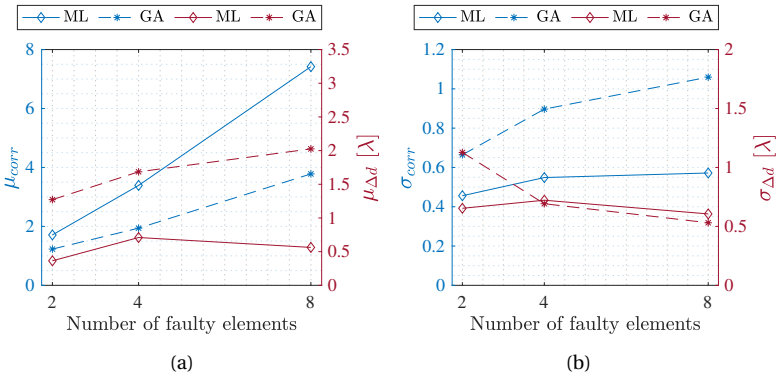

Figure 6.10: Analyses of the average correct prediction versus the average distance between the false prediction and its ground truth with corresponding standard deviations, Δd for theory-based prediction. (a) Average correct prediction versus average Δd over the number of faulty elements; (b) Standard deviation of the correct predictions versus standard deviation of Δd over the number of faulty elements.

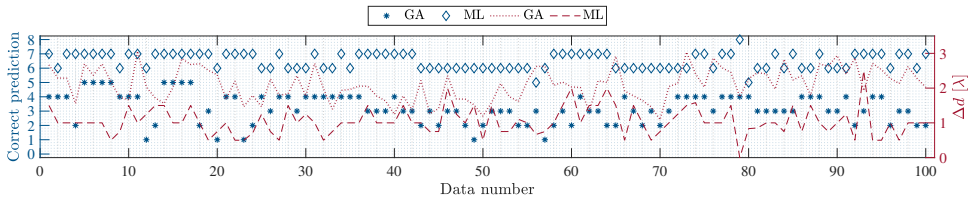

(a)

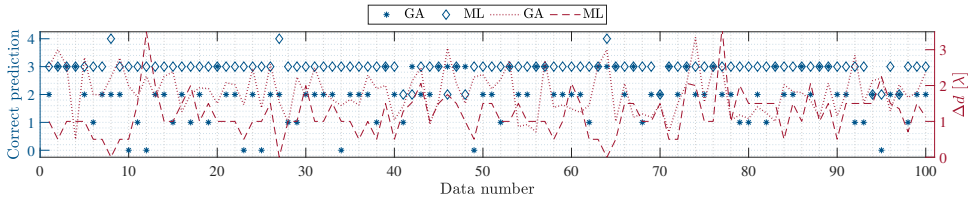

(b)

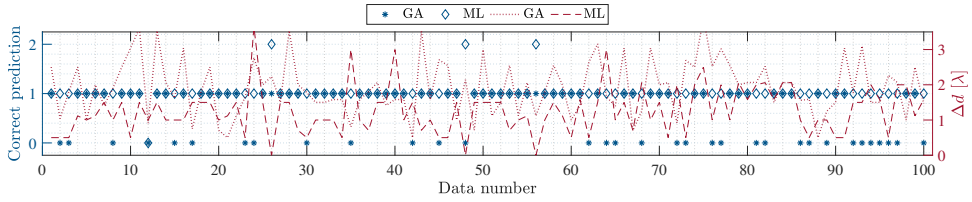

(c)

Figure 6.11: Results for the theory-enhanced prediction from 36 sampling points of FF measurement data and comparison with the GA as a benchmark methodology over the validation set. The left y-axis (blue) represents the number of correct predictions by the utilized methodologies and the right y-axis (red) describes the distance between the mispredicted element and its ground truth. (a) 8-element failure case; (b) 4-element failure case; (c) 2-element failure case.

proach for modeling the system where the data alone may not provide a complete understanding. In the literature, this methodology is also referred to as physics-informed neural network (PINN) [12].

The NN architecture shown in Fig. 6.5, is slightly modified by changing the activation function ReLU to the GeLU (Gaussian Error Linear Units), providing a smoother convergence. Furthermore, a total of 5000 measurement data is collected for the training and testing of the model. Among these data, 80% is used for the training, and the rest is used for validation and testing.

Since global optimizers require evaluating the cost for multiple candidate solutions across numerous generations to converge on an optimal result, the cost function must be adapted. Accordingly, the first term of the cost function in (6.3) now represents the measurement data corresponding to the specific failure case.

Figure 6.11(a), 6.11(b) and 6.11(c) illustrate the prediction results for the 8-, 4- and 2-element cases, respectively. As the measurement data introduces several nonlinearities,

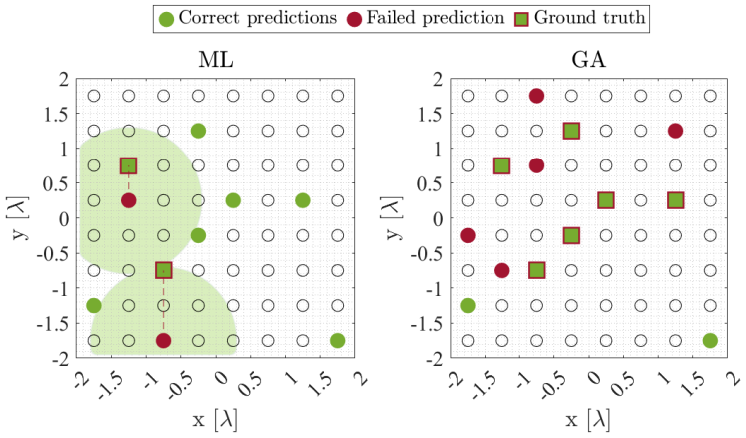

Figure 6.12: An example topology (data 70) for 8-element failure case predicted by the proposed ML technique (left) and the heuristic approach GA (right). Black circles illustrate the antenna elements, green-filled circles indicate the correct predictions, red-filled circles indicate the failed predictions and the ground truth of the failed predictions are shown as red-framed green squares. The light green circle regions in the ML plot highlight the possible positions for the ground truth of the corresponding failed prediction.

the number of correct predictions is slightly lower than the simulated data for the proposed methodology. While the prediction performance of the GA suffers critically, the proposed theory-enhanced NN model achieves robust performance by achieving an average number of correct predictions of 6.51, 2.95 and 1.02 for 8-, 4- and 2-element cases, respectively.

Although the prediction accuracy appears lower in cases with fewer faulty elements, the model is still able to identify the true location of the mispredicted elements within a region of 1.5λ radius on average with 95% accuracy. In an example case from the test data involving an 8-element failure, the proposed method successfully predicts 6 faulty elements while the GA identifies only 2 out of the 8 faulty elements (Fig. 6.12). Despite the model's failure to predict 2 faulty elements, these elements are located within the λ region, as highlighted in light green in Figure 6.12. Such errors bring minor changes in the pattern and are therefore harder to detect, yet it is possible to make a quick regional search to correct the few wrong predictions in the next iteration.

The consistency of the model over the different number of faulty elements is illustrated in Fig. 6.13 where the GA shows a similar behavior with the theory-based prediction. Notably, as the number of faulty elements decreases, both the average Δd and its standard deviation decrease correspondingly.

Lastly, two more models are trained to predict the faulty elements with a low number of pattern measurement nodes. The aim of this study is to reduce the measurement setup profile towards real-time in-field data collection without blockage from absorbing panels in the field of view (FoV). To realize this, some of the RMS detectors of the Antenna Dome are disabled, and the measured data is fed into the model. Figure 6.15 illustrates the sampling rings corresponding to the nodes' angular positions. For this purpose, the NN architecture is adopted for different numbers of input by resizing the

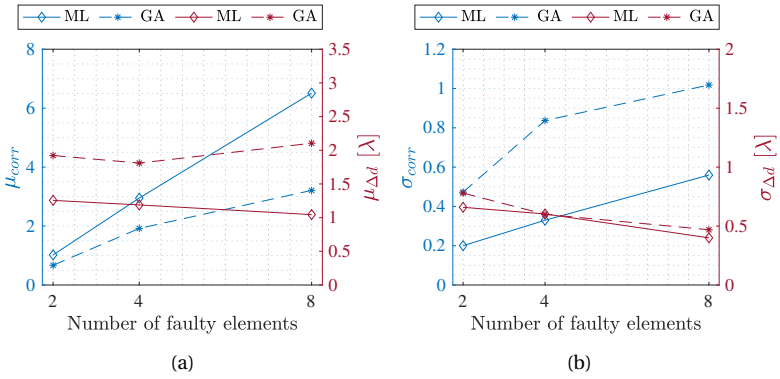

Figure 6.13: Analyses of the average correct prediction versus the average distance between the false prediction and its ground truth with corresponding standard deviations, Δd for theory-enhanced learning and prediction. (a) Average correct prediction versus average Δd over the number of faulty elements; (b) Standard deviation of the correct predictions versus standard deviation of Δd over the number of faulty elements.

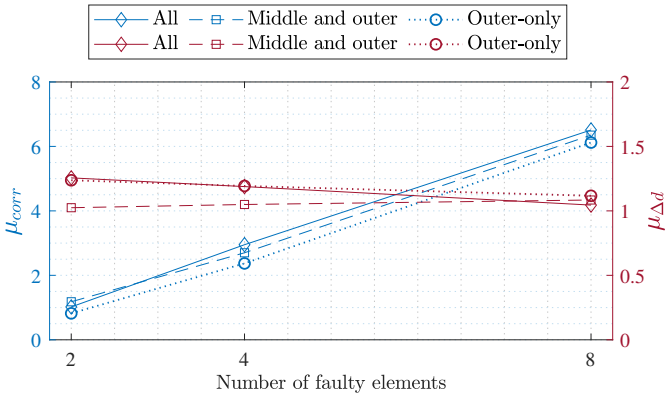

Figure 6.14: Analysis of the average correct prediction versus the average distance between the false prediction and its ground truth of the theory-enhanced prediction for the node rings.

input and adding additional layers as described in Section 6.2.2.

Initially, the middle and outer rings (comprising 25 nodes) are activated, followed by the activation of only the outer ring (comprising 15 nodes). Figure 6.14 presents the results of the proposed method for varying numbers of active nodes compared to the fully operational configuration. As the number of active nodes decreases significantly, the amount of information available for the NN to learn from also diminishes. Despite this reduction, the NN continues to perform similarly to the fully populated measurement setup.

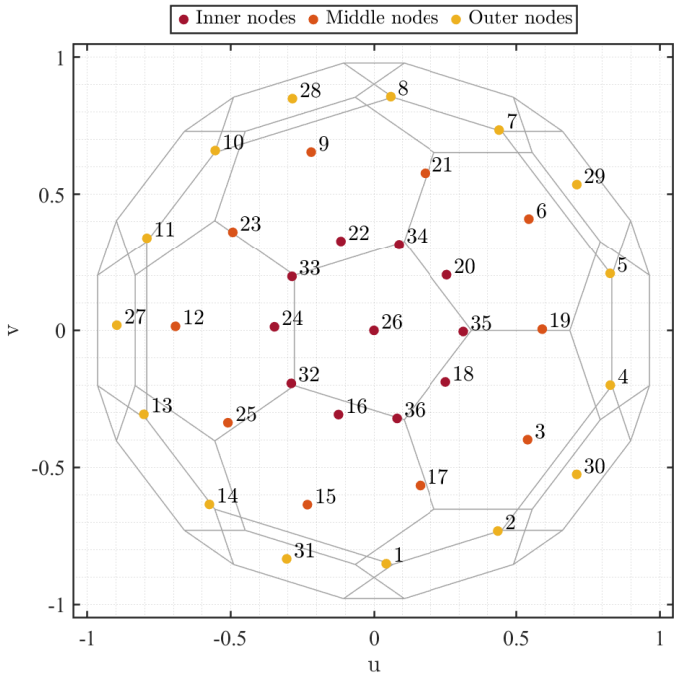

Figure 6.15: Detailed distribution of the nodes (RMS detectors) on the Antenna Dome structure. The nodes can be distributed into three different regions: inner nodes (16, 18, 20, 22, 24, 26, 32, 33, 34, 35, and 36), middle-ring nodes (3, 6, 9, 12, 15, 17, 19, 21, 23 and 25), and outer-ring nodes (1, 2, 4, 5, 7, 8, 10, 11, 13, 14, 27, 28, 29, 30, 31) which are indicated with red, orange, and yellow, respectively.

6.2.6. CONCLUSION

This study presents a novel ML-assisted approach for real-time fault detection in large-scale antenna arrays, addressing key performance limitations in the existing methodologies against real-world complexities such as IC nonlinearities and mutual coupling effects. The architecture of the proposed NN (shown in Fig. 6.5) consists of K layers, where the number K depends on the size of the array and the number of probes. The new method is successfully applied to a practical 64-element phased array operating at 26 GHz, using measurement data from a multi-probe system, the Antenna Dome.

The proposed theory-enhanced NN is capable of generating real-time predictions within seconds for the array under test, achieving better success rates of up to 40%, 25% and 20% as compared to the benchmarked heuristic (GA-based) prediction approach for 8-, 4-, and 2-element failures, respectively. Furthermore, while the prediction accuracy may be lower in scenarios involving fewer faulty elements, the proposed NN model remains capable of accurately identifying the possible correct locations of the mispredicted elements within an average range of one and a half wavelengths with 95% accuracy. The study on the impact of the number of probes for pattern sampling shows minimal performance deviations when the probes near the main beam region are removed for reduced hardware and processing complexity. These advancements mark signifi-

cant progress towards efficient, real-time antenna array diagnostics in practical settings, laying the groundwork for more reliable and scalable ML-assisted solutions. In future work, data collection under beam scanning and mechanical movement in the measurement setup will be considered, and the proposed NN technique will be enhanced with real-time pattern compensation features.

6.3. CONCLUSIONS

This chapter presents two novel ML-based methodologies addressing critical challenges in active phased array systems: (1) accurate, MC-aware MIMO radar array synthesis, and (2) real-time failure detection using sparse far-field measurements. These contributions enhance the performance, flexibility, and practical deployment of advanced antenna arrays.

In the first part, an ML-assisted design framework was introduced for the synthesis of irregular MIMO radar arrays. A spherical harmonics-based NN was developed to predict EEPs, accounting for MC effects. This model was integrated into a PSO routine, enabling realistic and efficient synthesis of MIMO radar patterns. The results showed strong agreement with full-wave simulations and significantly outperformed traditional design approaches that assume isolated elements.

In the second part, a new method for real-time fault detection was proposed, using only sparse, amplitude-only far-field data. A fully connected NN was trained using a theory-enhanced learning approach that combines EM modeling with real measurements from an active 64-element phased array operating at 26 GHz. The method demonstrated high fault localization accuracy, even with reduced numbers of measurement nodes, and significantly outperformed conventional heuristic approaches.

Together, these methods demonstrate how the integration of physics-based modeling and machine learning can lead to practical, scalable solutions for both array design and diagnostics.

7

Conclusions and Recommendations for Future Research

7.1. MAJOR RESULTS AND NOVEL CONTRIBUTIONS

The major results and contributions are discussed in the following points.

Aperiodic Phased Arrays and State-of-Art Challenges (Chapter 2)

A novel aperiodic-layout IC-integrated dual-polarized phased array system prototype was introduced, designed to assess the practical challenges of implementing non-uniform array layouts using existing components from a regular reference array. This system was experimentally verified, uncovering the potential and presenting a solution to the challenges faced by aperiodic phased arrays. Furthermore, this thesis explored the state-of-the-art mathematical modeling and optimization of aperiodic array topologies, highlighting that while these methods yield strong numerical results, practical implementation is hindered by MC effects with routing complexity and calibration challenges. The difficulty of accounting for MC effects in aperiodic arrays was discussed in detail, pointing out that oversimplified assumptions often lead to unreliable results, while accurate full-wave simulations remain computationally expensive.

EEP Prediction in Aperiodic Phased Arrays: An Approach for Sub-Arrays (Chapter 3)

A novel ANN-based method for predicting EEPs across the entire visible space (θ, ϕ plane) for flexible planar non-uniformly spaced arrays is proposed. With this method, the gap in the existing literature, which is primarily focused on linear arrays or limited visible spaces, is filled in. The framework incorporates a cascaded NN architecture, combining a fully connected NN for low-resolution EEP prediction with an efficient sub-pixel convolutional neural network (ESPCN) for high-resolution upscaling, resulting in significant reductions in computational time and load during array layout optimization. Furthermore, for the first time, the critical role of dataset size in EEP prediction via NNs is presented. This study emphasizes how the quality and size of training data directly impact prediction reliability, highlighting the variations in pattern prediction performance during validation. Additionally, it points out the need for new techniques that ensure accurate pattern predictions with smaller datasets, particularly as prediction reliability decreases with reduced dataset sizes, especially when handling larger numbers of elements and more complex mutual coupling effects.

EEP Prediction via Basis Functions and Ensemble Method (Chapters 4 and 5)

NNs can be effective for predicting EEPs and estimating MC effects in aperiodic arrays as it is shown in previous chapter. These methods are limited by the need for extensive training datasets and their high dependence on data quality, resulting in performance variations across different array elements. **Thus two novel approaches based on two auxiliary basis functions, IDM and spherical-harmonics, were proposed to achieve robust and reliable EEP predictions with smaller datasets.** First, the sunflower array topology was applied in constrained IDM to eliminate the need for optimization processes aimed at minimizing pattern error and dipole count, improving computational efficiency while maintaining reasonable accuracy. In addition to this, spherical

harmonics-based functions were introduced as an alternative basis for predicting EEPs. By using the spherical wave expansion, EEPs can be predicted more effectively, reducing the sensitivity of the model to errors from a high condition number in the IDM.

Additionally, a novel ensemble prediction technique was proposed, which integrates a two-stage neural network for $\theta - \phi$ plane EEP prediction and constrained IDM for dipole excitation prediction. Validation with a quasi-random five-element S-band pin-fed patch array topology showed a 60% reduction in mean squared error (MSE) and training data size. Further enhancing prediction accuracy, a stacked generalization method was introduced, using a meta-model to optimally combine the outputs of multiple base models, improving EEP prediction performance, especially in the presence of MC effects.

ML-Assisted Phased Array Topology Optimization for MIMO Radar (Chapter 6)

For the first time, the optimization of an aperiodic MIMO radar phased array through ML-based EEP prediction is proposed by using a novel approach that leverages the theory of the spherical wave expansion method. The technique aims to improve the accuracy and efficiency of EEP predictions. By incorporating this method into a particle swarm optimization (PSO) framework, it is possible to optimize the radar array topology and minimize the maximum SLL in a multi-beam configuration. The approach is demonstrated using a 6-element TX array and an 8-element RX array, highlighting the robustness and efficiency of the proposed solution for MC-aware radar synthesis with multiple scanned beams.

ML-Assisted Synthesis of MIMO Radar Topology and ML-Based Failure Diagnosis for Active Uniform Phased Array (Chapter 6)

A novel application of ML for MC-aware MIMO radar array design is proposed. A spherical harmonics-based NN framework was developed to accurately predict EEPs under coupling effects. Integrated into a PSO routine, this approach enabled efficient and realistic synthesis of irregular MIMO topologies.

Furthermore, for the first time, an ML-based technique was also applied to real-time fault detection in a 64-element active phased array using sparse, amplitude-only far-field measurements. A theory-assisted fully connected NN was developed and successfully identified faulty elements despite the presence of IC nonlinearities and MC effects. This approach offers a fast, scalable, and practical diagnostic solution for complex phased array systems.

7.2. RECOMMENDATIONS FOR FUTURE RESEARCH

This section outlines potential avenues for future research, each of which builds on the findings and limitations discussed in the preceding chapters.

INCORPORATING REFLECTION COEFFICIENTS INTO ML-ASSISTED MC ANALYSIS AND ARRAY SYNTHESIS

In this thesis, MC effects were primarily addressed through the prediction of EEPs, with analyses typically carried out at a fixed operating frequency for clarity and computational efficiency. While this captures key aspects of the MC effect, it does not imply a fundamental limitation of the approach. EEPs can be predicted at operational frequency band by generating and training on additional data, allowing for frequency-dependent variations due to changes in scattering behavior. However, MC also affects matching and port-to-port interactions, which are characterized by S-parameters. Although not the focus of this work, incorporating S-parameters could be beneficial in future studies, especially in scenarios where constraints on impedance matching or inter-element isolation are critical for system performance.

A recent study in [136] has demonstrated that S-parameters can be predicted using modeling techniques such as infinitesimal dipole-based representations, similar to those employed in EEP modeling within this thesis. This suggests that integrating S-parameter prediction into data-driven synthesis workflows is not only feasible but also promising. Future research should focus on embedding such information into learning-based optimization frameworks to help close the gap between simulated predictions and real-world array performance.

ENHANCING SURROGATE MODELING WITH DOMAIN KNOWLEDGE FOR SYNTHESIS APPLICATIONS

The performance and reliability of ML-based surrogate models in antenna synthesis are fundamentally shaped by the structure and quality of the data they are trained on. In this thesis, data-driven modeling was adopted in several stages of the workflow, where embedding physical theory was either impractical or infeasible at higher abstraction levels. Through these implementations, it became evident that surrogate models are most effective when the training data sufficiently spans the relevant design space and captures the behavioral diversity of the problem domain. Poorly represented or narrowly sampled datasets can significantly constrain generalization and lead to inaccurate synthesis outcomes.

While purely data-driven approaches can offer flexibility and scalability, especially when computational bottlenecks limit high-fidelity simulations, recent advances in PINNs have highlighted promising alternatives [137]. These methods, which incorporate fundamental physical laws, such as Maxwell's equations, directly into the learning process, point to the potential need for deeper theoretical integration in future modeling efforts, particularly in scenarios with limited data availability or demanding generalization requirements. Although such formulations remain challenging to apply in full generality to complex antenna systems, they provide a compelling direction for future work. Blending domain-specific insights with ML frameworks could serve as a practical compromise between purely empirical and deeply physics-driven approaches. Ultimately, advancing surrogate modeling in synthesis requires not only algorithmic innovation but also a deeper alignment between model structure, data representation, and the underlying physical model.

EMPLOYING MACHINE LEARNING FOR EFFICIENT (REAL-TIME) CALIBRATION OF ACTIVE ARRAYS

Calibration at both the post-manufacturing stage and during operation remains a critical step in active array systems, particularly due to the unpredictable deviations introduced by fabrication tolerances, thermal effects, component aging and nearby objects. A complete calibration process involves both diagnostics and compensation. In this work, we partially addressed the diagnostic aspect by studying element failures; however, full diagnostics would require characterizing the IC responses and element patterns for each IC configuration across different frequencies, temperatures, and operating conditions. These dynamic variations must then be compensated by appropriately adjusting the IC settings to meet the desired antenna performance criteria. In Appendix A.2, the benchmark heuristic calibration method based on near-field measurements has demonstrated notable improvements in beam quality with different scanning angles, SLL suppression, and gain uniformity. However, such sequential, element-wise procedures are inherently time-intensive and constrained in their adaptability to changing operating conditions or array types. Moreover, while they may suffice for basic beam steering, they fall short in enabling precise side lobe control or deep null placement, which are essential in many advanced applications.

Integrating ML into the calibration framework presents a compelling alternative by enabling data-driven approximation of the mapping between beamformer settings and array-level performance. Nevertheless, a major challenge in this direction lies in capturing the non-linear behavior of ICs, particularly the coupled response of phase shifters and variable gain amplifiers. Furthermore, practical deployment scenarios involve additional complexities such as signal path losses, impedance mismatches, and temperature-dependent drifts, all of which contribute to deviations from ideal responses.

To address these issues, future ML-based calibration frameworks must incorporate strategies that explicitly account for non-linear device characteristics and loss mechanisms. This may involve using physics-informed architectures, embedding prior knowledge about IC behavior, or employing hybrid learning schemes that combine empirical data with simulation-based augmentation. The goal is to achieve real-time, robust calibration with minimal measurement effort, while maintaining high fidelity in beamforming performance across dynamic operating environments. In this context, the DOME measurement system [135] offers strong potential as a platform for rapid and comprehensive data acquisition, which could enable scalable ML-based calibration and diagnostics in future implementations.

ADVANCED ML ARCHITECTURES FOR BRIDGING PREDICTION-PERFORMANCE GAPS AND SUPPORTING SCALABLE ARRAY CONFIGURATIONS

As antenna arrays become larger and more diverse, existing machine learning models may struggle to scale or generalize across different configurations. Future research could explore architectural adaptations that better handle such variability. For example, using modular or sparsely connected networks may improve efficiency when working with large arrays. Restructuring input data, such as dividing arrays into smaller regions, can also help manage complexity and promote learning across similar substructures. Multi-head models, which allow different parts of the network to focus on distinct aspects of

the task, may further support generalization across scanning angles, different polarizations, array or antenna types. In addition, the growing field of advanced architectures opens opportunities to design models more tailored to the characteristics of EM data. While this thesis focused on standard architectures suited to the considered challenges, more specialized models may be necessary to tackle increasingly complex scenarios and reduce the gap between predicted and real-world array performance in future work.

A

APPENDIX

A.1. GRANT PROPOSAL: CIRCULARLY-CLUSTERED APERIODIC ARRAY (CCAA) TOPOLOGY OPTIMIZATION

Our technical objective is to reduce, within the required field-of-view and for all beams scanned inside, the current -13dB side-lobe level to around -20dB and below, by using the minimum number of elements and keeping uniform excitations for the best power efficiency. Our proposed solution is based on creating an optimized irregularity/sparsity in the array layout, while minimizing the losses and calibration requirements by preserving a circular sub-array arrangement. The approach is also tailored to suitable antenna element design techniques and electromagnetic coupling between the elements. In the end product, each sub-array (consisting of four elements) will be controlled by a four-channel analog beam forming IC in a fully-integrated antenna system. The proposed methodology has been awarded the Delft Space Institute Seed Grants 2021.

A.1.1. PROBLEM DEFINITION

The main constraints required to be introduced for the innovative circular clustering algorithm are to integrate it efficiently into the optimization process. For this purpose, the following technical constraints must be considered:

- The four-channel analog beam forming chip ABF IC MMW9002KC of NXP is taken as a reference for the IC geometry.
- Each IC can control four antenna elements.
- An extra line from the IC RF output pins must be taken due to the distance from the center to the feeding point of the antenna element.

The proposed clustering algorithm allows the element to move along the pre-defined circular path during the optimization process. Figure A.1 illustrates an example IC structure with the associated array elements.

A

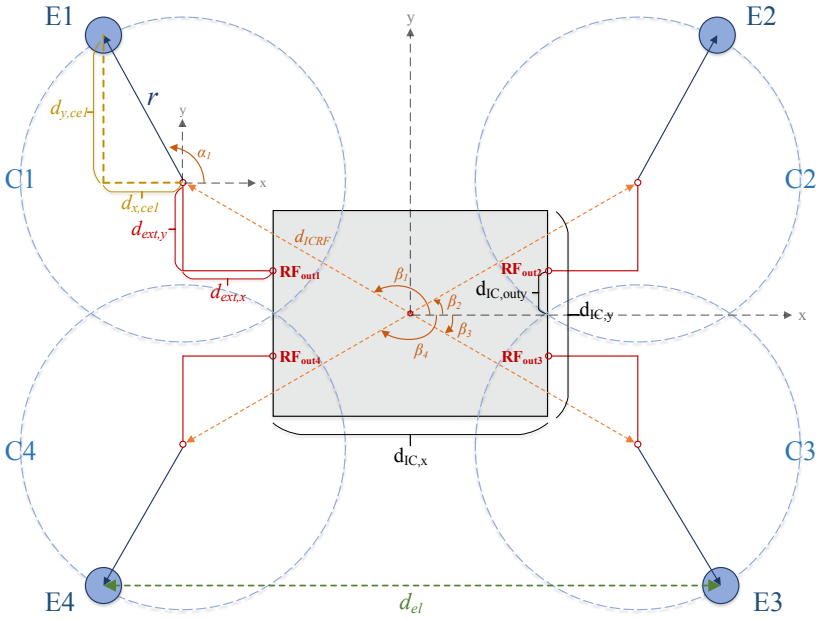

Figure A.1: Single IC geometry with four elements; the black rectangular box represents the IC, filled blue small circles represent the element positions, and blue-dotted circles illustrate an example circular path the element can move.

In the figure mentioned, the black rectangular box represents the IC structure, filled blue small circles represent the element positions, and blue-dotted circles illustrate the circular path the corresponding element can move. Hence, each element fed by the IC has its circular paths with an equal radius r. Depending on the structural preferences, the radius, initial element locations, and additional routing lines from IC can be manually or automatically adjusted by the algorithm. Next, the optimizer will optimize the element locations to achieve the desired array pattern. To formulate our problem, we need to derive the constraints of the problem. First, a single IC structure will be considered, and then an array structure comprising 9 ICs will be studied as a case study.

Let us consider an IC located at the center; $(x_{IC}, y_{IC}) = (0,0)$. The distance from the center of the circle C_i to the element location $(x^i_{\text{el}}, y^i_{\text{el}})$ can be derived as:

$$\begin{bmatrix} x^i_{\text{el}} \\ y^i_{\text{el}} \end{bmatrix} = \mathbf{RF}^{\mathbf{out}}_i + \Psi_i \cdot \begin{bmatrix} d_{x,cel} \\ d_{y,cel} \end{bmatrix} \qquad \text{for } i = 1,\ldots,4 \tag{A.1}$$

where Ψ_i is a constant matrix given as:

$$\Psi_i = \begin{cases} [-1\ 1]^{\mathrm{T}} & \text{for } i = 1 \\ [1\ 1]^{\mathrm{T}} & \text{for } i = 2 \\ [1\ -1]^{\mathrm{T}} & \text{for } i = 3 \\ [-1\ -1]^{\mathrm{T}} & \text{for } i = 4 \end{cases} \tag{A.2}$$

On the other hand, $\mathbf{RF}_i^{\mathbf{out}}$ can be pre-defined for a given IC. However, it can easily be derived from the center of the IC with given fundamental values to make the algorithm more autonomous. Therefore, in this study, the matrix above is a function of β, d_{ICRF}, $d_{ext,x}$, $d_{ext,y}$, $d_{IC,x}$, and $d_{IC,y}$ (please see Fig. A.1 for the variables).

Optimization of the element locations with a given circle constraint is computationally more expensive than the optimization of the element angle α_i, which is an angle between the x-axis and the radius vector of the element (see Figure A.1). The element angle can be calculated as:

$$\alpha_i = \tan^{-1}\left(\frac{d_{y,cel}}{d_{x,cel}}\right) \qquad \text{for } i = 1,...,4 \tag{A.3}$$

where $d_{x,cel}$, and $d_{y,cel}$ are the absolute distances between the center of the circle and the projection of the element location on x and y coordinates, respectively (see Figure A.1).

While the elements are allowed to move along the circles during the optimization process, the ICs are also planned to move freely. Hence, the optimizer will jointly optimize both the element angles and the IC locations.

A.1.2. PRELIMINARY DESIGN AND SIMULATION RESULTS

The details of the proposed design and optimization process are as follows:

- ICs have pre-calculated positions, $(x_i^{\mathrm{c}}, y_i^{\mathrm{c}})$ for $i = 1,...,N$ with N being the total number of IC, and can shift along x and y coordinates during the optimization process but, rotation around their center is not allowed.
- Each element has a common circle path with radius r. As discussed in the previous section, the element can move along the corresponding circle during the optimization process.
- An additional 1mm routing line is added (i.e., $d_{ext,x} = 1$ and $d_{ext,y} = 1$) to separate the element circles to increase the degrees of freedom.
- In total, 9 ICs (36-element topology) were used as a case study.
- The allowed minimum distance between the elements is assumed as $\lambda/2$.

Figure A.2 illustrates the discussed IC-to-element routing geometry. Figure A.2(a) is an optimized design that is given in Chapter 2 and Fig. A.2(b) is a preliminary IC routing design of the CCAA topology. Initially, we assumed 0.75λ element spacing to relax the

A

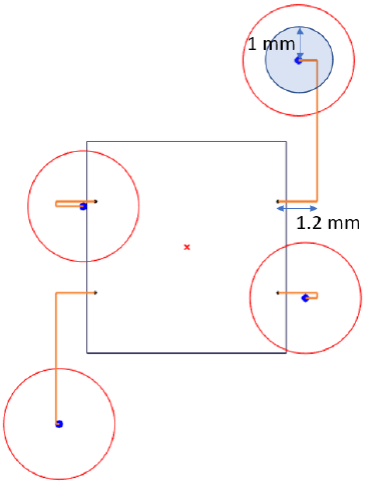

(a) Design in Chapter 2

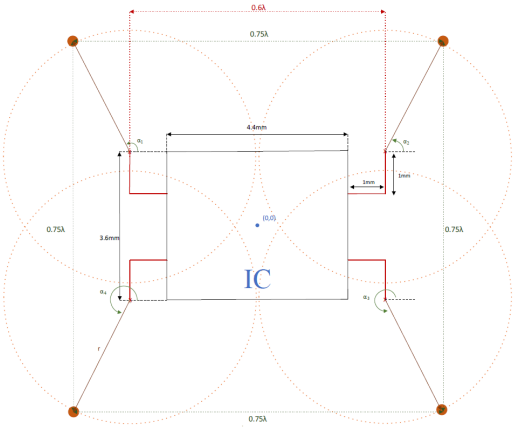

(b) Initial design in CCAA

Figure A.2: Comparison of the IC-to-element routing designs. In (b), the elements are allowed to move along the pre-defined circle without compromising the maximum routing length.

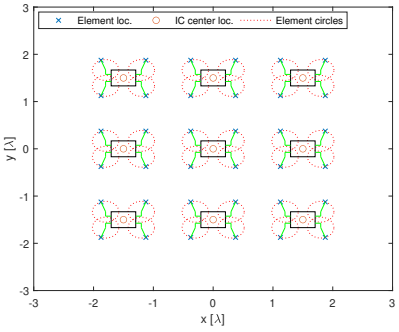

(a) Uniform layout geometry

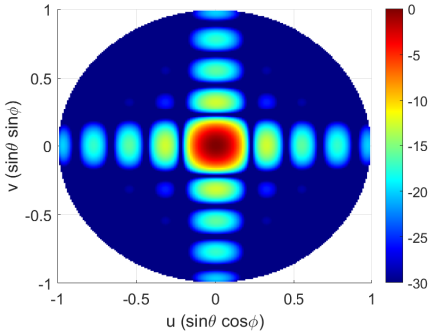

(b) Radiation pattern result

Figure A.3: The benchmark array topology concept.

circle constraint of the elements. In this way, the total routing length from an IC to a single element became:

$$L = 1\text{mm} + 1\text{mm} + r = 4.4\text{mm} \tag{A.4}$$

where r is calculated as 2.4mm. As a result, we already eliminated the 0.3dB loss per element that was caused by the additional feed line length in [28].

The regular benchmark topology and the corresponding radiation pattern are illustrated in Figure A.3. Further, the visualization of the new concept we propose and the promising preliminary results obtained by the PSO algorithm are provided in Figure A.4.

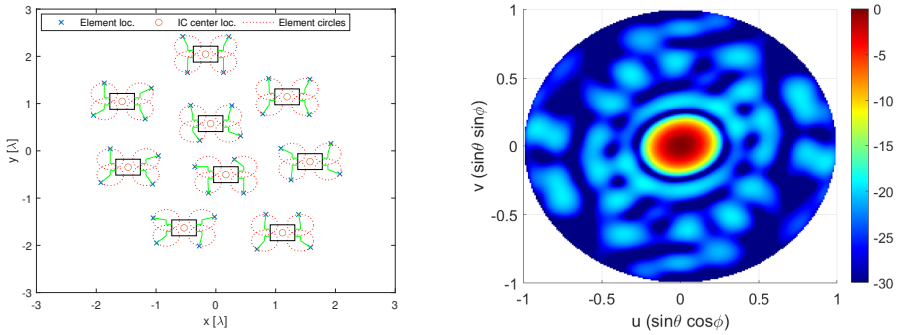

(a) A sample optimized layout geometry

(b) Radiation pattern result

Figure A.4: The proposed CCAA topology concept.

Figure A.3(a) and Figure A.4(a) visualize a 2D projection where the rectangles illustrate the IC package on one side of the substrate with the green lines showing the routing lines from the RF output of an IC to the associated antenna element on the opposite side.

The results show a sample output for a case study with 36 elements and broadside radiation with interference suppression over the entire visible space from −13 dB to about −19 dB. The algorithm can be adjusted for the requirements of our study cases by considering the number of elements, element spacing, and most importantly, the MC effects.

A.2. HEURISTIC OVER-THE-AIR CALIBRATION OF BEAMFORMER ICS IN ACTIVE MM-WAVE PHASED ARRAYS

Post-manufacturing over-the-air calibration deals with the non-linearities and variations in the IC responses for accurate beamforming (in terms of beam pointing angles and side lobe levels). The ambition is to measure the relative gain and phase contribution of each radiating element (when all other elements are active) for all frequencies and angles of interest at all possible IC settings and operating temperatures [122], which is practically infeasible. Under simultaneous excitation, obtaining even a subset of the element responses via mature techniques such as the rotating element electric field vector (REV) method [138] can be extremely time-consuming. Low-complexity alternatives such as the beam steering mode [139] limit the calibration to the specified observation angles. Therefore, the industry currently adopts sequential single-element measurement-based (with all other elements turned off) calibration with a near-field scanner [140]. This section tests the impact of such a calibration procedure on a 64-element state-of-the-art uniform mm-wave phased array that was introduced in Chapter 2.

A.2.1. ANTENNA UNDER TEST (AUT)

The 64-element dual-polarized (Horizontal: H-pol. and Vertical: V-pol.) 5G antenna by NXP Semiconductors and partners [42] is used as the AUT in the transmit mode (see

A

Figure A.5: The active 64-element millimeter-wave (24–28 GHz) phased array by NXP Semiconductors and partners [42].

Chapter 2.1 for the design details), which is shown in Fig. A.5. Furthermore, an open-ended waveguide from Microwave Vision Group (MVG OEW2200) is used as a probe (without correction, as we are interested in the relative magnitude-phase differences in transmission coefficients) in the near-field measurements. The measurement setup is installed in the Delft University Chamber for Antenna Tests (DUCAT).

A.2.2. CALIBRATION PROCEDURE

To illustrate the need for post-manufacturing calibration and its complexity, the transmission coefficients between the RF inputs and the probe for a subset of all available gain-phase settings at each channel in IC #6 at 26 GHz (center frequency) are plotted in Fig. A.6. In these measurements, the probe is accurately aligned in front of the corresponding antenna element, and only the measured IC channel is activated (i.e., sequential measurement), while all other channels are turned off. From Fig. A.6, the following observations are made:

- The transmission coefficients for the same IC settings are different for each antenna element and for each polarization.
- The changes in magnitude and phase of the transmission coefficients do not linearly depend on the digital gain-phase settings in the IC.
- The magnitude and phase of the transmission coefficients are coupled to each other. In other words, changes in the gain settings in the IC cause changes in the phase, and vice versa.

This necessitates the development of a new calibration methodology which, to a certain extent, addresses the consequences of these observations. For feasibility in terms of

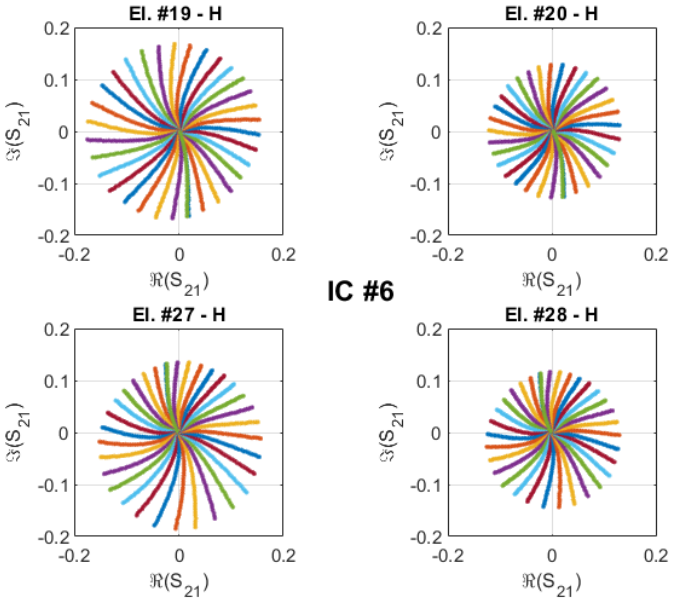

(a) H-pol.

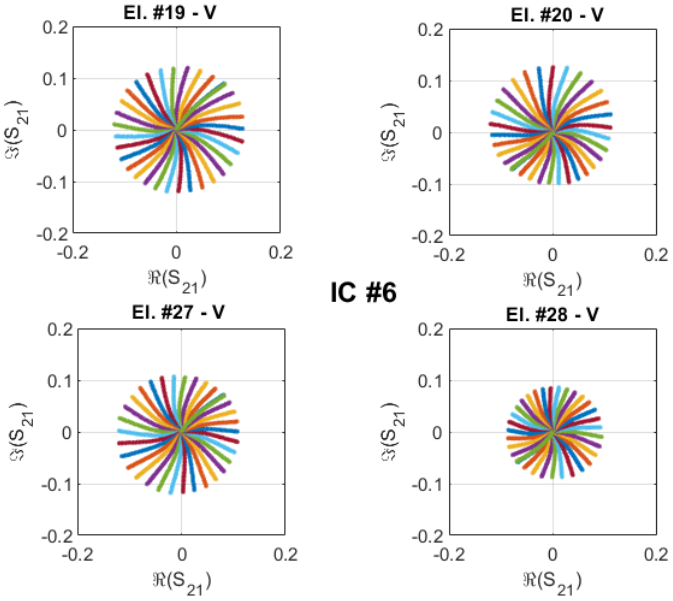

(b) V-pol.

Figure A.6: The complex transmission coefficient between the RF input and the probe for different gain-phase settings at each channel in IC #6: (a) H-pol., (b) V-pol.

A

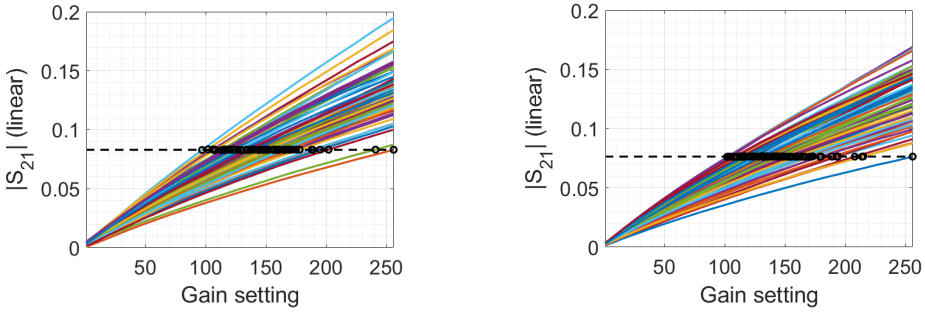

(a) H-pol. (b) V-pol.

Figure A.7: Magnitude of transmission coefficients between the RF input and the probe for different gain settings at each element (for 0 phase setting): (a) H-pol., (b) V-pol.

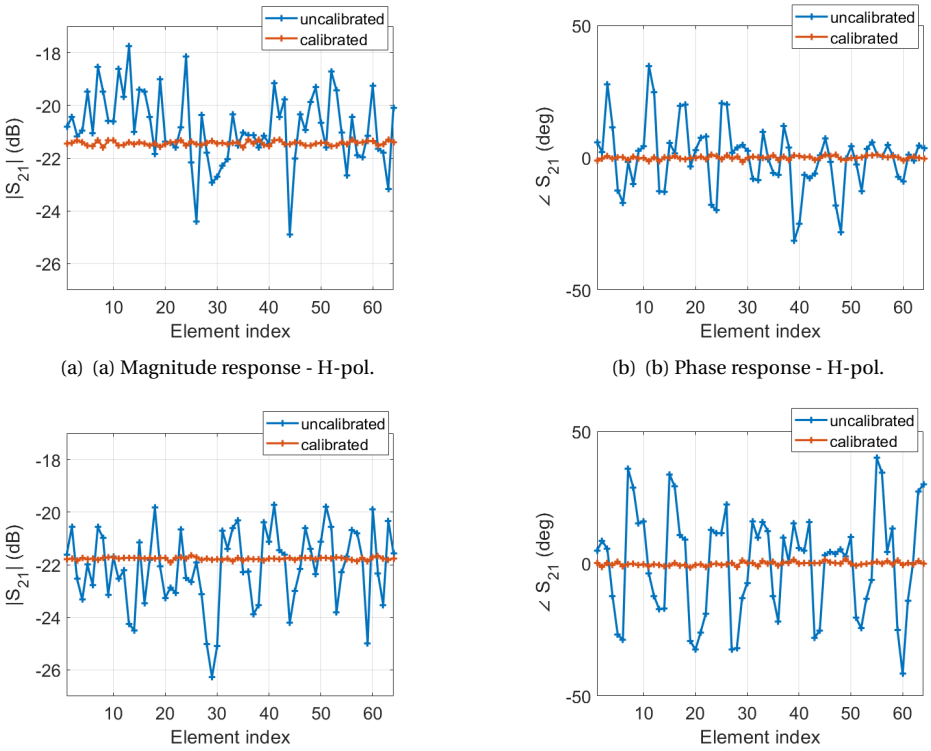

(a) (a) Magnitude response - H-pol. (b) (b) Phase response - H-pol.

(c) (c) Magnitude response - V-pol. (d) (d) Phase response - V-pol.

Figure A.8: The transmission coefficients between the RF input and the probe in front of each antenna element before and after the proposed calibration: (a) magnitude response - H-pol., (b) phase response - H-pol., (c) magnitude response - V-pol., (d) phase response - V-pol.

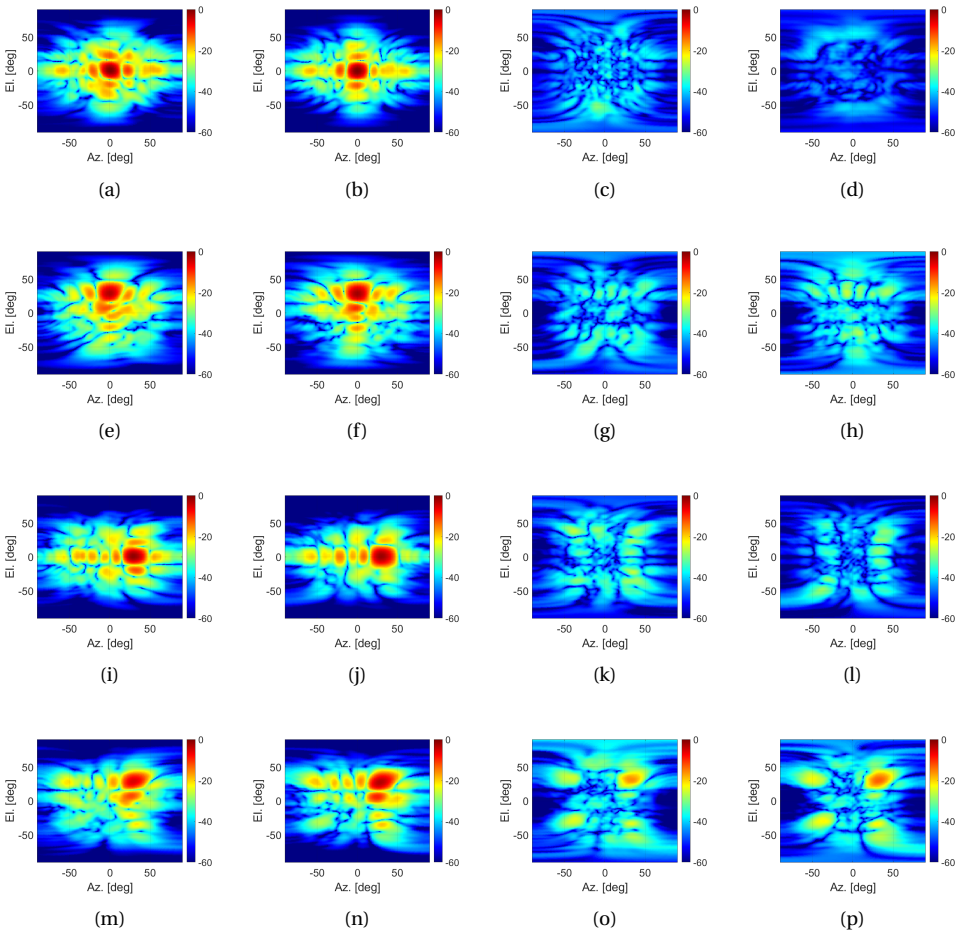

Figure A.9: Radiation patterns when H-pol. is active: (a) [0 0] deg. scan, co-pol., uncalibrated, (b) [0 0] deg. scan, co-pol., calibrated, (c) [0 0] deg. scan, cross-pol., uncalibrated, (d) [0 0] deg. scan, cross-pol., calibrated, (e) [0 30] deg. scan, co-pol., uncalibrated, (f) [0 30] deg. scan, co-pol., calibrated, (g) [0 30] deg. scan, cross-pol., uncalibrated, (h) [0 30] deg. scan, cross-pol., calibrated, (i) [30 0] deg. scan, co-pol., uncalibrated, (j) [30 0] deg. scan, co-pol., calibrated, (k) [30 0] deg. scan, cross-pol., uncalibrated, (l) [30 0] deg. scan, cross-pol., calibrated, (m) [30 30] deg. scan, co-pol., uncalibrated, (n) [30 30] deg. scan, co-pol., calibrated, (o) [30 30] deg. scan, cross-pol., uncalibrated, (p) [30 30] deg. scan, cross-pol., calibrated.

measurement time, some assumptions and simplifications have to be made in sequential measurements. The proposed heuristic calibration method includes the following 5 steps:

Step-1: The magnitude of transmission coefficients are measured sequentially for the same IC phase setting (equal to 0 in our case) at each element for each polarization for varied IC gain settings from the maximal (= 255) to the minimal (= 0). The result at 26 GHz is plotted in Fig. A.7.

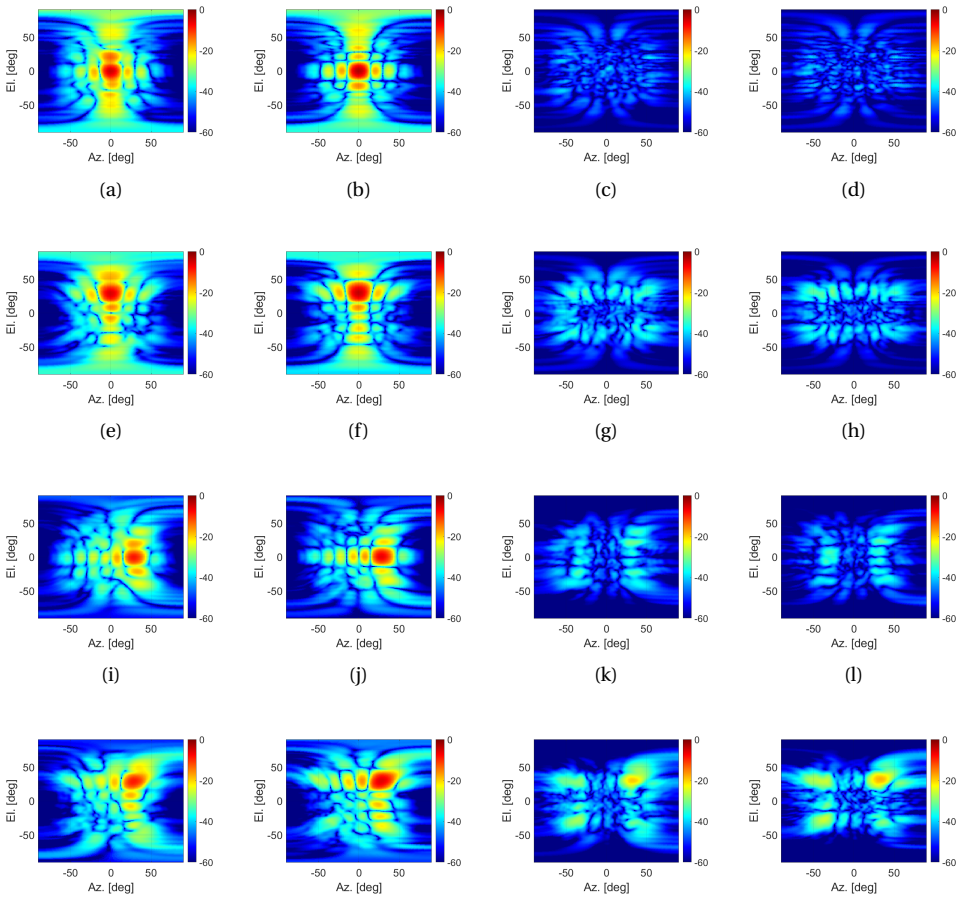

Figure A.10: Radiation patterns when V-pol. is active: (a) [0 0] deg. scan, co-pol., uncalibrated, (b) [0 0] deg. scan, co-pol., calibrated, (c) [0 0] deg. scan, cross-pol., uncalibrated, (d) [0 0] deg. scan, cross-pol., calibrated, (e) [0 30] deg. scan, co-pol., uncalibrated, (f) [0 30] deg. scan, co-pol., calibrated, (g) [0 30] deg. scan, cross-pol., uncalibrated, (h) [0 30] deg. scan, cross-pol., calibrated, (i) [30 0] deg. scan, co-pol., uncalibrated, (j) [30 0] deg. scan, co-pol., calibrated, (k) [30 0] deg. scan, cross-pol., uncalibrated, (l) [30 0] deg. scan, cross-pol., calibrated, (m) [30 30] deg. scan, co-pol., uncalibrated, (n) [30 30] deg. scan, co-pol., calibrated, (o) [30 30] deg. scan, cross-pol., uncalibrated, (p) [30 30] deg. scan, cross-pol., calibrated.

Step-2: New gain settings are determined for correction by assigning the largest gain setting (=255) to the element with the lowest $|S_{21}|$. The other elements are assigned to the gain settings that gives the corresponding value of $|S_{21}|$ for equalization. This is visualized with a dashed horizontal line in Fig. A.7.

Step-3: New phases of transmission coefficients (after gain correction) are measured sequentially.

Step-4: New phase settings are determined (based on the desired scan angle) by using

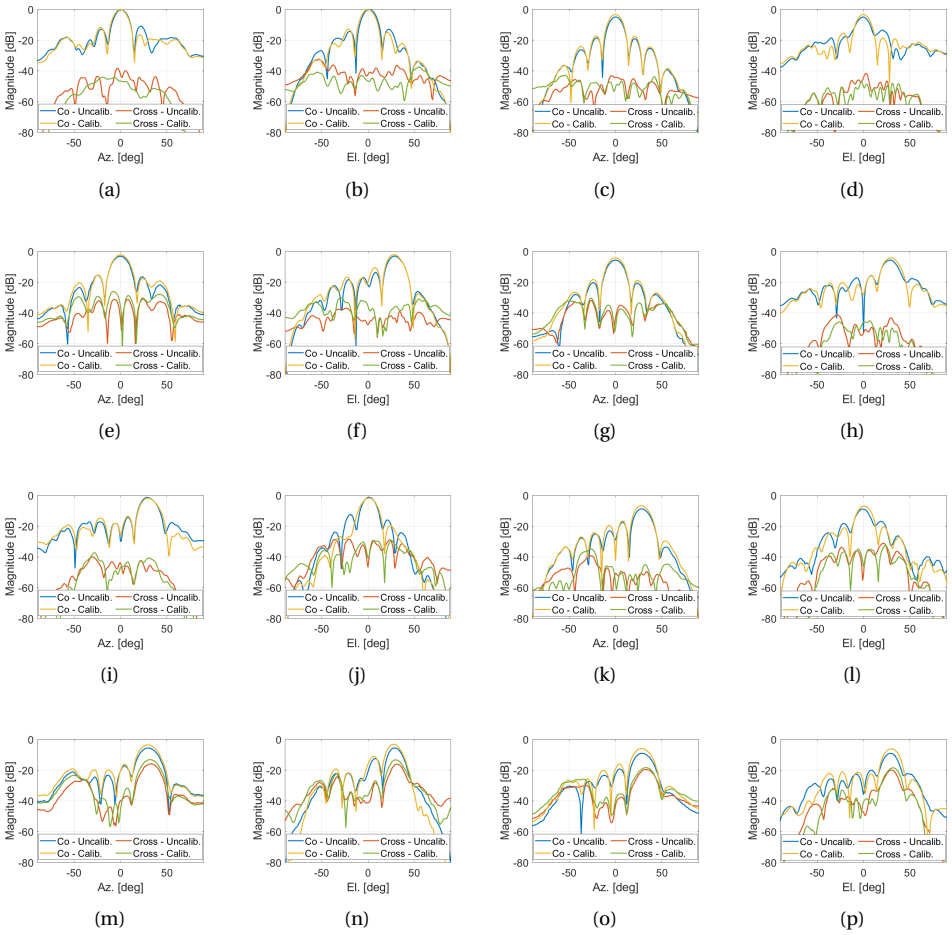

Figure A.11: Pattern cuts for the uncalibrated vs. calibrated array: (a) H-pol. active, [0 0] deg. scan, 0 deg. elevation, (b) H-pol. active, [0 0] deg. scan, 0 deg. azimuth, (c) V-pol. active, [0 0] deg. scan, 0 deg. elevation, (d) V-pol. active, [0 0] deg. scan, 0 deg. azimuth, (e) H-pol. active, [0 30] deg. scan, 30 deg. elevation, (f) H-pol. active, [0 30] deg. scan, 0 deg. azimuth, (g) V-pol. active, [0 30] deg. scan, 30 deg. elevation, (h) V-pol. active, [0 30] deg. scan, 0 deg. azimuth, (i) H-pol. active, [30 0] deg. scan, 0 deg. elevation, (j) H-pol. active, [30 0] deg. scan, 30 deg. azimuth, (k) V-pol. active, [30 0] deg. scan, 0 deg. elevation, (l) V-pol. active, [30 0] deg. scan, 30 deg. azimuth, (m) H-pol. active, [30 30] deg. scan, 30 deg. elevation, (n) H-pol. active, [30 30] deg. scan, 30 deg. azimuth, (o) V-pol. active, [30 30] deg. scan, 30 deg. elevation, (p) V-pol. active, [30 30] deg. scan, 30 deg. azimuth.

the phase differences with the idealistic 1.4-degree linear step assumption.

Step-5: The IC settings are tweaked for a few elements to get close-to-uniform gains and linear phases.

The comparison of transmission coefficients before and after calibration for the broadside beam is provided in Fig. A.8. In the uncalibrated response, the phase settings are

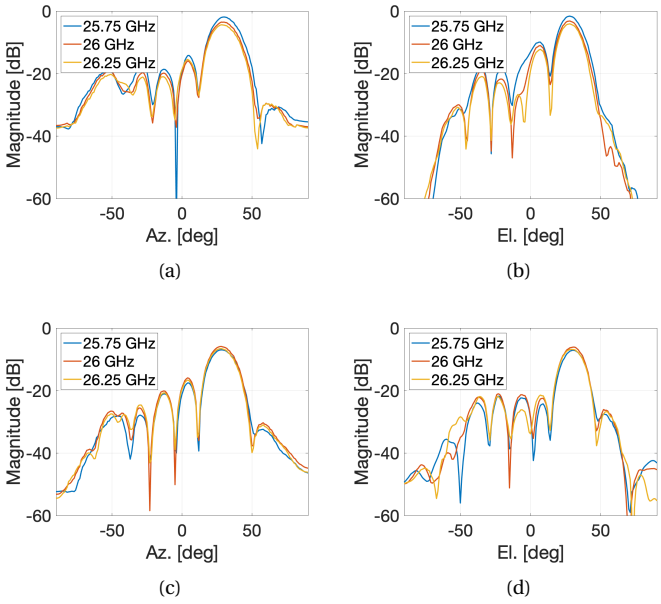

Figure A.12: Pattern cuts for the calibrated array at [30 30] deg. scan within a ±0.25 GHz (i.e., about 2%) bandwidth: (a) H-pol. active, 30 deg. elevation, (b) H-pol. active, 30 deg. azimuth, (c) V-pol. active, 30 deg. elevation, (d) V-pol. active, 30 deg. azimuth.

set to 0, while the gain settings are equal to 160, which is the approximate average of the gain settings in the calibrated case. The uncalibrated result shows large gain and phase variations between the elements. The uniformity of S_{21} in the calibrated cases in Fig. A.8 demonstrates the validity of our method. Note that we apply our calibration technique at a single operation frequency.

Next, we will discuss the impacts of the proposed calibration procedure on the radiation patterns at 26 GHz, and lastly, we will demonstrate the effect of frequency variations (within a 2% bandwidth) on the patterns.

A.2.3. PATTERN MEASUREMENT RESULTS

Fig. A.9 and Fig. A.10 show the radiation patterns for H-pol. and V-pol. operation, respectively. Both co-pol. and cross-pol. patterns are provided in case of uncalibrated and calibrated IC responses. Fig. A.11 shows the pattern cuts for clear comparison. The following major observations are made:

- In broadside radiation, the calibration method compensates for the small (1 deg.) beam pointing error when H-pol. is active. This comes at the expense of a slightly (1 dB) increased PSLL. When V-pol. is active, on the other hand, we observe a 1.8 dB increase in gain and a 4 dB decrease in the PSLL in the elevation plane.

- For the beam scanned in elevation, after calibration, the gain is increased by 1

dB (when H-pol. is active) and 1.5 dB (when V-pol. is active). The PSLL in the azimuthal plane remains unchanged, while the PSLL in the elevation plane increases by 2 dB for H-pol. and decreases by 1.5 dB for V-pol. operation.

- For the beam scanned in azimuth, we see a significant reduction in PSLL in the elevation plane (around 7 dB for H-pol. and 3.5 dB for V-pol. operation). Moreover, the gain is increased by 2 dB in the V-pol. case.
- For diagonal scanning, the cross-pol. levels become critical, which can be attributed to the antenna element design. After calibration, the peak co-pol. gains increase by 2 dB and 3 dB, while the peak cross-pol. gains also increase by 3 dB and 1 dB, for H-pol. and V-pol. operation, respectively. We also see a 4 dB reduction in the PSLL in the elevation plane for V-pol. case.

Lastly, Fig. 11 illustrates the changes in the pattern with frequency. It is observed that the calibration method is relatively robust within the 0.5 GHz bandwidth for both H-pol. and V-pol. operation. It is also observed that the peak gain is more stable in the V-pol. case.

A.2.4. CONCLUSION

A heuristic active phased array post-manufacturing calibration method is described and tested for a practical dual-polarized mm-wave antenna. The method is based on equalizing the sequential near-field responses of embedded elements (driven by analog beamformer ICs) on broadside at the center frequency (26 GHz). The measurements demonstrate that via calibration, the array performance in terms of gain, PSLL and beam pointing angle can be improved, the extent of which depends on the polarization and scan angle. Overall, the benefits of calibration become more significant in the V-pol operation and in the elevation plane, which can be attributed to the relatively large phase variations across the uncalibrated array. Measurements in a 2% bandwidth show the robustness of the calibrated array patterns against the frequency change.

BIBLIOGRAPHY

[1] P. Ninni, P. Bolli, F. Paonessa, G. Pupillo, G. Virone, and S. Wijnholds, "Electromagnetic analysis and experimental validation of the lofar radiation patterns," *International Journal of Antennas and Propagation*, vol. 2019, pp. 1–12, 01 2019.

[2] Y. Yin, Z. Zhang, T. Kanar, S. Zihir, and G. M. Rebeiz, "A 24-29.5 ghz 256-element 5g phased-array with 65.5 dbm peak eirp and 256-qam modulation," in *2020 IEEE/MTT-S International Microwave Symposium (IMS)*, pp. 687–690, 2020.

[3] M. C. Viganó, D. Llorens del Río, F. Bongard, and S. Vaccaro, "Sparse array antenna for ku-band mobile terminals using 1 bit phase controls," *IEEE Transactions on Antennas and Propagation*, vol. 62, no. 4, pp. 1723–1730, 2014.

[4] J. Puskely, T. Mikulasek, Y. Aslan, A. Roederer, and A. Yarovoy, "5G SIW-Based Phased Antenna Array with Cosecant-Squared Shaped Pattern," *IEEE Transactions on Antennas and Propagation*, vol. 70, no. 1, pp. 250–259, 2022.

[5] Y. Aslan, J. Puskely, A. Roederer, and A. Yarovoy, "Multiple beam synthesis of passively cooled 5g planar arrays using convex optimization," *IEEE Transactions on Antennas and Propagation*, vol. 68, no. 5, pp. 3557–3566, 2020.

[6] G. Oliveri, G. Gottardi, F. Robol, A. Polo, L. Poli, M. Salucci, M. Chuan, C. Massagrande, P. Vinetti, M. Mattivi, R. Lombardi, and A. Massa, "Codesign of Unconventional Array Architectures and Antenna Elements for 5G Base Stations," *IEEE Transactions on Antennas and Propagation*, vol. 65, no. 12, pp. 6752–6767, 2017.

[7] Y. Aslan, *Antenna array synthesis and beamforming for 5G applications: An interdisciplinary approach*. PhD thesis, Delft University of Technology, 2020.

[8] P. Rocca, G. Oliveri, R. J. Mailloux, and A. Massa, "Unconventional phased array architectures and design methodologies—a review," *Proceedings of the IEEE*, vol. 104, no. 3, pp. 544–560, 2016.

[9] A. Roederer, J. Puskely, Y. Aslan, and A. Yarovoy, "Shaped Elevation Patterns for 5G Base Stations," in *IEEE International Symposium on Antennas and Propagation and USNC-URSI Radio Science Meeting (APS/URSI)*, pp. 795–796, 2021.

[10] Q. Wu, H. Wang, and W. Hong, *Machine Learning-Assisted Optimization and Its Application to Antenna and Array Designs*, ch. 2, pp. 44–50. John Wiley Sons, Ltd, 2023.

[11] A. Massa, D. Marcantonio, X. Chen, M. Li, and M. Salucci, "DNNs as Applied to Electromagnetics, Antennas, and Propagation - A Review," *IEEE Antennas and Wireless Propagation Letters*, vol. 18, pp. 2225–2229, 11 2019.

[12] M. Raissi, P. Perdikaris, and G. Karniadakis, "Physics-informed neural networks: A deep learning framework for solving forward and inverse problems involving nonlinear partial differential equations," *Journal of Computational Physics*, vol. 378, pp. 686–707, 2019.

[13] J. A. Hodge, K. V. Mishra, and A. I. Zaghloul, "Deep inverse design of reconfigurable metasurfaces for future communications," 2021.

[14] Q. Wu, H. Wang, and W. Hong, *Machine Learning-Assisted Optimization and Its Application to Antenna and Array Designs*, ch. 12, pp. 371–383. John Wiley Sons, Ltd, 2023.

[15] S. Koziel and S. Ogurtsov, "Fast simulation-driven optimization of planar microstrip antenna arrays using surrogate superposition models," *International Journal of RF and Microwave Computer-Aided Engineering*, vol. 25, 11 2014.

[16] C. Maeurer, P. Futter, and G. Gampala, "Antenna design exploration and optimization using machine learning," in *2020 14th European Conference on Antennas and Propagation (EuCAP)*, pp. 1–5, 2020.

[17] Q. Liu, L. Xiao, R. Hong, and H. Hu, *Deep Learning for High Contrast Inverse Scattering of Electrically Large Structures*, pp. 435–485. 2023.

[18] I. Rekanos, "Neural-network-based inverse-scattering technique for online microwave medical imaging," *IEEE Transactions on Magnetics*, vol. 38, no. 2, pp. 1061–1064, 2002.

[19] Z.-M. Liu, C. Zhang, and P. S. Yu, "Direction-of-arrival estimation based on deep neural networks with robustness to array imperfections," *IEEE Transactions on Antennas and Propagation*, vol. 66, no. 12, pp. 7315–7327, 2018.

[20] A. Barthelme and W. Utschick, "Doa estimation using neural network-based covariance matrix reconstruction," *IEEE Signal Processing Letters*, vol. 28, pp. 783–787, 2021.

[21] M. O. Akinsolu, Q. Hua, and B. Liu, "Automated design of antennas using ai techniques: A review of contemporary methods and applications," in *2024 18th European Conference on Antennas and Propagation (EuCAP)*, pp. 1–4, 2024.

[22] C. Cui, W. T. Li, X. T. Ye, P. Rocca, Y. Q. Hei, and X. W. Shi, "An effective artificial neural network-based method for linear array beampattern synthesis," *IEEE Transactions on Antennas and Propagation*, vol. 69, no. 10, pp. 6431–6443, 2021.

[23] C. Cui, W. T. Li, X. T. Ye, Y. Q. Hei, P. Rocca, and X. W. Shi, "Synthesis of mask-constrained pattern-reconfigurable nonuniformly spaced linear arrays using artificial neural networks," *IEEE Transactions on Antennas and Propagation*, vol. 70, no. 6, pp. 4355–4368, 2022.

[24] Q. Wu, W. Chen, C. Yu, H. Wang, and W. Hong, "Machine learning-assisted array synthesis using active base element modeling," *IEEE Transactions on Antennas and Propagation*, vol. 70, no. 7, pp. 5054–5065, 2022.

[25] A. M. Kulkarni, S. S. Pattnaik, and G. Saini, "Genetic-cnn based fault diagnosis in antenna array," in *2023 IEEE International Symposium On Antennas And Propagation (ISAP)*, pp. 1–2, 2023.

[26] H. M. Yao, M. Li, L. Jiang, K. L. Yeung, and M. Ng, "Antenna array diagnosis using a deep learning approach," *IEEE Transactions on Antennas and Propagation*, vol. 72, no. 6, pp. 5396–5401, 2024.

[27] R. Adeogun, "Calibration of stochastic radio propagation models using machine learning," *IEEE Antennas and Wireless Propagation Letters*, vol. 18, no. 12, pp. 2538–2542, 2019.

[28] M. Buenaventura Camps, "Design of a sparse irregular array for beyond 5G base stations," *MSc Thesis, TU Delft, The Netherlands*, 2021.

[29] X. Gu, D. Liu, and B. Sadhu, "Packaging and antenna integration for silicon-based millimeter-wave phased arrays: 5G and beyond," *IEEE Journal of Microwaves*, vol. 1, no. 1, pp. 123–134, 2021.

[30] K. K. W. Low, G. M. Rebeiz, S. Zihir, and T. Kanar, "A reconfigurable dual-polarized 1024-element ka-band SATCOM transmit phased-array with large scan volume and +48 dBW EIRP," in *2021 IEEE MTT-S International Microwave Symposium (IMS)*, pp. 638–640, 2021.

[31] E. V. P. Anjos, M. SalarRahimi, T. A. H. Bressner, P. Takhighani, A. Lahuerta-Lavieja, A. Elsakka, J. S. Siebenga, V. Volski, C. Fager, D. Schreurs, G. A. E. Vandenbosch, U. Johannsen, A. B. Smolders, and M. Geurts, "FORMAT: A reconfigurable tile-based antenna array system for 5G and 6G millimeter-wave testbeds," *IEEE Systems Journal*, vol. 16, no. 3, pp. 4489–4500, 2022.

[32] K. Kibaroglu, M. Sayginer, T. Phelps, and G. M. Rebeiz, "A 64-element 28-GHz phased-array transceiver with 52-dBm EIRP and 8–12-Gb/s 5G link at 300 meters without any calibration," *IEEE Transactions on Microwave Theory and Techniques*, vol. 66, no. 12, pp. 5796–5811, 2018.

[33] X. Gu, B. Sadhu, D. Liu, C. Baks, and A. Valdes-Garcia, "Antenna-in-package design and module integration for millimeter-wave communication and 5G," in *2018 International Symposium on VLSI Design, Automation and Test (VLSI-DAT)*, pp. 1–2, 2018.

[34] R. Valkonen, "Compact 28-GHz phased array antenna for 5G access," in *2018 IEEE/MTT-S International Microwave Symposium - IMS*, pp. 1334–1337, 2018.

[35] Y. Aslan, A. Roederer, and A. Yarovoy, "System advantages of using large-scale aperiodic array topologies in future mm-wave 5G/6G base stations: An interdisciplinary look," *IEEE Systems Journal*, vol. 16, no. 1, pp. 1239–1248, 2022.

[36] Y. Aslan, J. Puskely, J. H. J. Janssen, M. Geurts, A. Roederer, and A. Yarovoy, "Thermal-aware synthesis of 5G base station antenna arrays: An overview and a sparsity-based approach," *IEEE Access*, vol. 6, pp. 58868–58882, 2018.

[37] G. Toso, P. Angeletti, and C. Mangenot, "A comparison of density and amplitude tapering for transmit active arrays," in *Proc. EuCAP*, pp. 840–843, 2009.

[38] Y. Aslan, J. Puskely, A. Roederer, and A. Yarovoy, "Multiple beam synthesis of passively cooled 5G planar arrays using convex optimization," *IEEE Trans. Antennas Propag.*, vol. 68, no. 5, pp. 3557–3566, 2020.

[39] A. J. van den Biggelaar, C. J. C. Vertegaal, U. Johannsen, A. B. Smolders, and M. Geurts, "On the design and calibration of a 5G millimeter-wave dual-polarized active phased array," in *2021 IEEE-APS Topical Conference on Antennas and Propagation in Wireless Communications (APWC)*, pp. 055–060, 2021.

[40] J. R. De Luis *et al.*, "Antenna-to-beamformer assignment and mapping in phased array antenna systems," 2021. US Patent 10,971,817.

[41] Y. Aslan, J. Puskely, A. Roederer, and A. Yarovoy, "Synthesis of quasi-modular circularly polarized 5G base station antenna arrays based on irregular clustering and sequential rotation," *Microw. Opt. Technol. Lett.*, vol. 63, no. 4, pp. 1278–1285, 2021.

[42] M. Geurts and J. Janssen, "Designing a 5G mm-wave antenna means balancing tradeoffs," NXP Smarter World Blog, 2023.

[43] Y. Aslan *et al.*, "Heuristic over-the-air calibration of beamformer ICs in active mm-wave phased arrays," in *Proc. IEEE CAMA*, pp. 840–845, 2023.

[44] H. Singh, S. H L, and R. Jha, "Mutual coupling in phased arrays: A review," *International Journal of Antennas and Propagation*, vol. 2013, 01 2013.

[45] B. Fuchs, A. Skrivervik, and J. R. Mosig, "Synthesis of uniform amplitude focused beam arrays," *IEEE Antennas and Wireless Propagation Letters*, vol. 11, pp. 1178–1181, 2012.

[46] J. I. Echeveste, M. A. González de Aza, and J. Zapata, "Array pattern synthesis of real antennas using the infinite-array approach and linear programming," *IEEE Transactions on Antennas and Propagation*, vol. 63, no. 12, pp. 5417–5424, 2015.

[47] J. Corcoles, J. Rubio, and M. Gonzalez, "Spherical-wave-based shaped-beam field synthesis for planar arrays including the mutual coupling effects," *IEEE Transactions on Antennas and Propagation*, vol. 59, no. 8, pp. 2872–2881, 2011.

[48] J. Corcoles, M. A. Gonzalez, and J. Rubio, "Fourier synthesis of linear arrays based on the generalized scattering matrix and spherical modes," *IEEE Transactions on Antennas and Propagation*, vol. 57, no. 7, pp. 1944–1951, 2009.

[49] J. Ignacio Echeveste, M. González de Aza, J. Rubio, and C. Craeye, "Gradient-based aperiodic array synthesis of real arrays with uniform amplitude excitation including mutual coupling," *IEEE Transactions on Antennas and Propagation*, vol. 65, no. 2, pp. 541–551, 2017.

[50] L. Cen, Z. L. Yu, W. Ser, and W. Cen, "Linear aperiodic array synthesis using an improved genetic algorithm," *IEEE Transactions on Antennas and Propagation*, vol. 60, no. 2, pp. 895–902, 2012.

[51] Y. Liu, X. Huang, K. D. Xu, Z. Song, S. Yang, and Q. H. Liu, "Pattern synthesis of unequally spaced linear arrays including mutual coupling using iterative fft via virtual active element pattern expansion," *IEEE Transactions on Antennas and Propagation*, vol. 65, no. 8, pp. 3950–3958, 2017.

[52] Y. Aslan, M. Candotti, and A. Yarovoy, "Synthesis of multi-beam space-tapered linear arrays with side lobe level minimization in the presence of mutual coupling," in *2019 13th European Conference on Antennas and Propagation (EuCAP)*, pp. 1–5, 2019.

[53] H. V. Bui, S. N. Jha, and C. Craeye, "Fast full-wave synthesis of printed antenna arrays including mutual coupling," *IEEE Transactions on Antennas and Propagation*, vol. 64, no. 12, pp. 5163–5171, 2016.

[54] Y. Gong, S. Xiao, and B.-Z. Wang, "An ann-based synthesis method for nonuniform linear arrays including mutual coupling effects," *IEEE Access*, vol. 8, pp. 144015–144026, 2020.

[55] W. Shi, J. Caballero, F. Huszár, J. Totz, A. P. Aitken, R. Bishop, D. Rueckert, and Z. Wang, "Real-time single image and video super-resolution using an efficient sub-pixel convolutional neural network," in *2016 IEEE Conference on Computer Vision and Pattern Recognition (CVPR)*, pp. 1874–1883, 2016.

[56] N. B. Onat, I. Roldan, F. Fioranelli, A. Yarovoy, and Y. Aslan, "Efficient embedded element pattern prediction via machine learning: A case study with planar nonuniform sub-arrays," in *2023 17th European Conference on Antennas and Propagation (EuCAP)*, pp. 1–5, 2023.

[57] W. Shi, J. Caballero, F. Huszár, J. Totz, A. Aitken, R. Bishop, D. Rueckert, and Z. Wang, "Real-time single image and video super-resolution using an efficient sub-pixel convolutional neural network," in *Proc. CVPR*, 2016.

[58] H. Zhao, O. Gallo, I. Frosio, and J. Kautz, "Loss functions for image restoration with neural networks," *IEEE Transactions on Computational Imaging*, vol. 3, no. 1, pp. 47–57, 2017.

[59] S. M. Mikki and A. A. Kishk, "Theory and applications of infinitesimal dipole models for computational electromagnetics," *IEEE Transactions on Antennas and Propagation*, vol. 55, no. 5, pp. 1325–1337, 2007.

[60] W.-J. Zhao, B.-F. Wang, E.-X. Liu, H. B. Park, H. H. Park, E. Song, and E.-P. Li, "An effective and efficient approach for radiated emission prediction based on amplitude-only near-field measurements," *IEEE Transactions on Electromagnetic Compatibility*, vol. 54, no. 5, pp. 1186–1189, 2012.

[61] Y.-F. Shu, X.-C. Wei, J. Fan, R. Yang, and Y.-B. Yang, "An equivalent dipole model hybrid with artificial neural network for electromagnetic interference prediction," *IEEE Transactions on Microwave Theory and Techniques*, vol. 67, no. 5, pp. 1790–1797, 2019.

[62] M. Serhir, N. Ribière-Tharaud, and D. Picard, "Robust antenna diagnostics method using equivalent elemental dipoles and the spherical wave expansion," in *Proceedings of the Fourth European Conference on Antennas and Propagation*, pp. 1–5, 2010.

[63] S. Karimkashi, A. Kishk, and G. Zhang, "Modelling of aperiodic array antennas using infinitesimal dipoles," *IET Microwaves, Antennas & Propagation*, vol. 6, no. 7, pp. 761–767, 2012.

[64] J.-R. Regue, M. Ribó, J.-M. Garrell, and A. Martín, "A genetic algorithm based method for source identification and far-field radiated emissions prediction from near-field measurements for pcb characterization," *IEEE Transactions on Electromagnetic Compatibility*, vol. 43, no. 4, pp. 520–530, 2001.

[65] T. Sijher and A. Kishk, "Antenna modeling by infinitesimal dipoles using genetic algorithms," *Progress In Electromagnetics Research*, vol. 52, pp. 225–254, 2005.

[66] T. S. Sijher and A. A. Kishk, "Infinitesimal dipoles simulation of antennas using genetic algorithms," in *2004 10th International Symposium on Antenna Technology and Applied Electromagnetics and URSI Conference*, pp. 1–4, 2004.

[67] S. J. Yang, Y. D. Kim, D. W. Yi, N. H. Myung, *et al.*, "Antenna modeling using sparse infinitesimal dipoles based on recursive convex optimization," *IEEE Antennas and Wireless Propagation Letters*, vol. 17, no. 4, pp. 662–665, 2018.

[68] M. Serhir, P. Besnier, and M. Drissi, "An accurate equivalent behavioral model of antenna radiation using a mode-matching technique based on spherical near field measurements," *IEEE Transactions on Antennas and Propagation*, vol. 56, no. 1, pp. 48–57, 2008.

[69] M. Serhir, P. Besnier, N. Ribière-Tharaud, and M. Drissi, "The use of infinitesimal dipoles and the spherical wave expansion for planar antennas modeling," in *Proceedings of the Fourth European Conference on Antennas and Propagation*, pp. 1–5, 2010.

[70] L. R. Turner, "Inverse of the vandermonde matrix with applications," tech. rep., No. NASA-TN-D-3547, 1966.

[71] W. Gautschi, "Optimally conditioned vandermonde matrices," *Numerische Mathematik*, vol. 24, pp. 1–12, 1975.

[72] M. C. Viganó, G. Toso, G. Caille, C. Mangenot, I. E. Lager, *et al.*, "Sunflower array antenna with adjustable density taper," *International Journal of Antennas and Propagation*, vol. 2009, 2009.

[73] Y. Aslan, J. Puskely, J. H. J. Janssen, M. Geurts, A. Roederer, and A. Yarovoy, "Thermal-aware synthesis of 5G base station antenna arrays: An overview and a sparsity-based approach," *IEEE Access*, vol. 6, pp. 58868–58882, 2018.

[74] V. H. Vu and T. Tao, "The condition number of a randomly perturbed matrix," in *Proceedings of the 39th Annual ACM Symposium on Theory of Computing*, pp. 248–255, 2007.

[75] H. G. Moura, E. C. Junior, A. Lenzi, and V. C. Rispoli, "On a stochastic regularization technique for ill-conditioned linear systems," *Open Engineering*, vol. 9, no. 1, pp. 52–60, 2019.

[76] N. B. Onat, I. Roldan, F. Fioranelli, A. Yarovoy, and Y. Aslan, "Efficient embedded element pattern prediction via machine learning: A case study with planar non-uniform sub-arrays," in *Proc. 17th EuCAP*, pp. 1–5, 2023.

[77] N. B. Onat, I. Roldan, F. Fioranelli, A. Yarovoy, and Y. Aslan, "Constrained infinitesimal dipole modeling-assisted ensemble prediction of embedded element patterns via machine learning," *IEEE Transactions on Antennas and Propagation*, vol. 72, no. 9, pp. 7353–7358, 2024.

[78] M. Costa, A. Richter, and V. Koivunen, "Unified array manifold decomposition based on spherical harmonics and 2-D Fourier basis," *IEEE Transactions on Signal Processing*, vol. 58, no. 9, pp. 4634–4645, 2010.

[79] R. Penrose, "A generalized inverse for matrices," *Mathematical Proceedings of the Cambridge Philosophical Society*, vol. 51, no. 3, pp. 406–413, 1955.

[80] M. Serhir, P. Besnier, and M. Drissi, "An accurate equivalent behavioral model of antenna radiation using a mode-matching technique based on spherical near field measurements," *IEEE Trans. Antennas Propag.*, vol. 56, no. 1, pp. 48–57, 2008.

[81] N. B. Onat, A. Yarovoy, and Y. Aslan, "Sunflower array of infinitesimal dipoles for constrained antenna modeling," in *Proc. 18th EuCAP*, 2024, accepted for publication.

[82] W. Shi, J. Caballero, F. Huszár, J. Totz, A. P. Aitken, R. Bishop, D. Rueckert, and Z. Wang, "Real-time single image and video super-resolution using an efficient sub-pixel convolutional neural network," 2016.

[83] D. Stathakis, "How many hidden layers and nodes?," *International Journal of Remote Sensing*, vol. 30, no. 8, pp. 2133–2147, 2009.

[84] X. Xu, Y. Ding, S. X. Hu, M. Niemier, J. Cong, Y. Hu, and Y. Shi, "Scaling for edge inference of deep neural networks," *Nat. Electron.*, vol. 1, pp. 216–222, Apr. 2018.

[85] H. Zhao, O. Gallo, I. Frosio, and J. Kautz, "Loss functions for image restoration with neural networks," *IEEE Trans. Comput. Imaging*, vol. 3, no. 1, pp. 47–57, 2017.

[86] D. Kingma and J. Ba, "Adam: A method for stochastic optimization," in *Proc. ICLR*, 2014.

[87] D. P. Kingma and J. Ba, "Adam: A method for stochastic optimization," 2017.

[88] E. Loew and R. L. Haupt, "Two-way pattern synthesis for the airborne phased array radar (apar)," in *2022 IEEE International Symposium on Phased Array Systems Technology (PAST)*, pp. 1–3, 2022.

[89] S. Sun and Y. D. Zhang, "4d automotive radar sensing for autonomous vehicles: A sparsity-oriented approach," *IEEE Journal of Selected Topics in Signal Processing*, vol. 15, no. 4, pp. 879–891, 2021.

[90] X. Zhuge and A. G. Yarovoy, "Study on two-dimensional sparse mimo uwb arrays for high resolution near-field imaging," *IEEE Transactions on Antennas and Propagation*, vol. 60, no. 9, pp. 4173–4182, 2012.

[91] X. Zhuge, A. G. Yarovoy, T. Savelyev, and L. Ligthart, "Modified kirchhoff migration for uwb mimo array-based radar imaging," *IEEE Transactions on Geoscience and Remote Sensing*, vol. 48, no. 6, pp. 2692–2703, 2010.

[92] J. Wang, P. Aubry, and A. Yarovoy, "3-d short-range imaging with irregular mimo arrays using nufft-based range migration algorithm," *IEEE Transactions on Geoscience and Remote Sensing*, vol. 58, no. 7, pp. 4730–4742, 2020.

[93] Y. Jiang, J. Dong, F. Liu, Y. Yue, and R. Shi, "Pattern synthesis of mimo radar using differential particle swarm optimization algorithm," *Optik*, vol. 126, no. 24, pp. 5781–5786, 2015.

[94] J. Wang, X. Wu, J. Ye, J. Sun, and G. Hua, "A novel two-way pattern synthesis method with the uniform and thinned arrays," *IEEE Antennas and Wireless Propagation Letters*, vol. 23, no. 10, pp. 3108–3112, 2024.

[95] R. Z. Syeda, M. C. van Beurden, and A. B. Smolders, "Sparse virtual array synthesis for mimo radar imaging systems," *IET Microwaves, Antennas & Propagation*, vol. 15, no. 11, pp. 1458–1472, 2021.

[96] W. P. Keizer, "Planar phased-array antennas: Mutual coupling and ultralow peak sidelobes," *IEEE Antennas and Propagation Magazine*, vol. 61, no. 1, pp. 14–28, 2018.

[97] E. BouDaher, F. Ahmad, M. G. Amin, and A. Hoorfar, "Effect of mutual coupling on direction-of-arrival estimation using sparse dipole arrays," in *2016 IEEE International Symposium on Antennas and Propagation (APSURSI)*, pp. 2189–2190, 2016.

[98] C. Guo, W. Hong, H. Lin, and B. Wu, "Planar near-field diagnosis of the large-scale antenna arrays using particle swarm optimization," in *2020 Asia Conference on Computers and Communications (ACCC)*, pp. 20–24, 2020.

[99] M. Levitas, D. Horton, and T. Cheston, "Practical failure compensation in active phased arrays," *IEEE Transactions on Antennas and Propagation*, vol. 47, no. 3, pp. 524–535, 1999.

[100] T. Peters, "A conjugate gradient-based algorithm to minimize the sidelobe level of planar arrays with element failures," *IEEE Transactions on Antennas and Propagation*, vol. 39, no. 10, pp. 1497–1504, 1991.

[101] F. Zaman, H. u. Hassan, S. U. Khan, A. u. Rehman, M. A. Z. Raja, and S. A. Niazi, "Backtracking search optimization paradigm for pattern correction of faulty antenna array in wireless mobile communications," *Wireless Communications and Mobile Computing*, vol. 2019, no. 1, p. 9046409, 2019.

[102] S. J. Spiegel, "Analysis of impairments, error correction and evaluation of adaptive antenna arrays based on vector modulators beamforming ics," in *2022 IEEE Microwaves, Antennas, and Propagation Conference (MAPCON)*, pp. 1255–1260, 2022.

[103] A. J. van den Biggelaar, C. J. C. Vertegaal, U. Johannsen, A. B. Smolders, and M. Geurts, "On the design and calibration of a 5g millimeter-wave dual-polarized active phased array," in *2021 IEEE-APS Topical Conference on Antennas and Propagation in Wireless Communications (APWC)*, pp. 055–060, 2021.

[104] Y. Aslan, C. E. Kiper, A. J. van den Biggelaar, U. Johannsen, and A. Yarovoy, "Passive cooling of mm-wave active integrated 5g base station antennas using cpu heatsinks," in *2019 16th European Radar Conference (EuRAD)*, pp. 121–124, IEEE, 2019.

[105] D. L. Balageas, P. Levesque, and A. A. Deom, "Characterization of electromagnetic fields using a lock-in infrared thermographic system," in *Thermosense XV: An International Conference on Thermal Sensing and Imaging Diagnostic Applications*, vol. 1933, pp. 274–285, SPIE, 1993.

[106] D. Prost, F. Issac, and P. Reulet, "Large scale measurement of microwave electric field using infrared thermography and electromagnetic simulation," in *Progress In Electromagnetics Research Symposium Proceedings, Marrakesh, Morocco*, 2011.

[107] J. Norgard and R. Musselman, "Direct diagnostic testing of phased array antennas using infrared imaging techniques," in *2006 17th International Zurich Symposium on Electromagnetic Compatibility*, pp. 292–295, IEEE, 2006.

[108] K. Muzaffar, L. I. Giri, K. Chatterjee, S. Tuli, and S. Koul, "Fault detection of antenna arrays using infrared thermography," *Infrared Physics & Technology*, vol. 71, pp. 464–468, 2015.

[109] A. Hubrechsen and T. Van den Biggelaar, "Over-the-air techniques for measuring integrated rf electronics and antennas.," *Microwave Journal*, vol. 67, no. 1, 2024.

[110] J. Lee, E. Ferren, D. Woollen, and K. Lee, "Near-field probe used as a diagnostic tool to locate defective elements in an array antenna," *IEEE Transactions on Antennas and Propagation*, vol. 36, no. 6, pp. 884–889, 1988.

[111] O. Bucci, M. Migliore, G. Panariello, and P. Sgambato, "Accurate diagnosis of conformal arrays from near-field data using the matrix method," *IEEE Transactions on Antennas and Propagation*, vol. 53, no. 3, pp. 1114–1120, 2005.

[112] H. Zhao, Y. Zhang, Q. Wan, J. Hu, and Z. Chen, "Near-field-based array failure diagnosis using sparse source reconstruction," in *2017 Asia-Pacific International Symposium on Electromagnetic Compatibility (APEMC)*, pp. 309–311, 2017.

[113] O. J. Famoriji, Z. Zhang, A. Fadamiro, Z. Khan, and F. Lin, "Active antenna array diagnosis from far-field measurements," in *2018 IEEE International Conference on Integrated Circuits, Technologies and Applications (ICTA)*, pp. 38–39, 2018.

[114] J. Miao, B. Chen, X. Zhang, and Y. Chen, "An improved method of diagnosis of failed elements in arrays based on far-field radiation pattern," in *2016 Progress in Electromagnetic Research Symposium (PIERS)*, pp. 467–471, 2016.

[115] O. Bucci, A. Capozzoli, and G. D'Elia, "Diagnosis of array faults from far-field amplitude-only data," *IEEE Transactions on Antennas and Propagation*, vol. 48, no. 5, pp. 647–652, 2000.

[116] B. Fuchs, L. L. Coq, and M. D. Migliore, "Fast antenna array diagnosis from a small number of far-field measurements," *IEEE Transactions on Antennas and Propagation*, vol. 64, no. 6, pp. 2227–2235, 2016.

[117] Z. Li, P. Huo, and J. Wu, "Fast antenna array diagnosis based on shifted base mode character from sparse measurements," *IEEE Transactions on Antennas and Propagation*, vol. 70, no. 12, pp. 12163–12176, 2022.

[118] N. Boopalan, A. K. Ramasamy, and F. Nagi, "A comparison of faulty antenna detection methodologies in planar array," *Applied Sciences*, vol. 13, no. 6, p. 3695, 2023.

[119] G. Bai, C. Liao, Y. Liu, and Y.-F. Cheng, "Rapid failure diagnosis of impaired linear antenna arrays based on matrix pencil method," *IEEE Antennas and Wireless Propagation Letters*, vol. 21, no. 8, pp. 1708–1712, 2022.

[120] R. Moretta, G. Leone, M. A. Maisto, R. Pierri, and R. Solimene, "Array faulty element diagnostics by few phaseless data and convex optimization," in *2023 17th European Conference on Antennas and Propagation (EuCAP)*, pp. 1–4, 2023.

[121] S. K. Goudos, C. Kalialakis, and R. Mittra, "Evolutionary algorithms applied to antennas and propagation: A review of state of the art," *International Journal of Antennas and Propagation*, vol. 2016, no. 1, p. 1010459, 2016.

[122] A. van den Biggelaar, C. Vertegaal, U. Johannsen, M. Geurts, and A. Smolders, "Post-manufacturing calibration procedure for medium-sized silicon-based active phased arrays for mm-wave wireless communications," in *2020 14th European Conference on Antennas and Propagation (EuCAP)*, pp. 1–5, 2020.

[123] Y. Aslan, P. Aubry, N. B. Onat, J. Janssen, M. Geurts, and A. Yarovoy, "Heuristic over-the-air calibration of beamformer ics in active mm-wave phased arrays," in *2023 IEEE Conference on Antenna Measurements and Applications (CAMA)*, pp. 840–845, 2023.

[124] A. Garufo *et al.*, "Mm-wave antennas in package for 5G applications," in *Proc. IEEE ISAP*, 2021.

[125] F. A. Musters, R. Coesoij, M. Migliore, F. Schettino, and M. Spirito, "The antenna dome real-time distributed antenna pattern characterization system," in *2021 97th ARFTG Microwave Measurement Conference (ARFTG)*, pp. 1–5, 2021.

[126] R. A. Coesoij, F. A. Musters, D. Roos, T. van Velden, and M. Spirito, "Calibration approaches in multi-node antenna characterization setups," in *2023 100th ARFTG Microwave Measurement Conference (ARFTG)*, pp. 1–4, 2023.

[127] M. Lange, "Impact of statistical errors on active phased-array antenna performance," in *MILCOM 2007 - IEEE Military Communications Conference*, pp. 1–5, 2007.

[128] M. H. Moghaddam, S. Rezaei Aghdam, and T. Eriksson, "Statistical analysis of antenna array systems with perturbations in phase, gain and element positions," in *2019 IEEE Global Conference on Signal and Information Processing (GlobalSIP)*, pp. 1–5, 2019.

[129] S. Kirkpatrick, C. D. Gelatt, and M. P. Vecchi, "Optimization by simulated annealing," *Science*, vol. 220, no. 4598, pp. 671–680, 1983.

[130] S. Chatterjee, S. Chatterjee, B. Bandyopadhyay, and A. Majumder, "Simultaneous control of side lobe level and beamwidth in planar array antenna using restricted search evolutionary algorithms," in *2019 IEEE Asia-Pacific Microwave Conference (APMC)*, pp. 673–675, 2019.

[131] P. Swain, S. K. Mohanty, and B. B. Mangaraj, "Linear dipole antenna array design and optimization using gravitational search algorithm," in *2016 2nd International Conference on Advances in Electrical, Electronics, Information, Communication and Bio-Informatics (AEEICB)*, pp. 514–518, 2016.

[132] D. Goldberg and J. Holland, "Genetic algorithms and machine learning," *Machine Learning*, vol. 3, p. 95–99, 1988.

[133] H. M. Yao, M. Li, L. Jiang, K. L. Yeung, and M. Ng, "Antenna array diagnosis using a deep learning approach," *IEEE Transactions on Antennas and Propagation*, vol. 72, no. 6, pp. 5396–5401, 2024.

[134] B.-K. Yeo and Y. Lu, "Fast detection and location of failed array elements using the fast svm algorithm," in *2010 14th International Symposium on Antenna Technology and Applied Electromagnetics the American Electromagnetics Conference*, pp. 1–4, 2010.

[135] M. S. R. A. Coesoij, F. A. Musters, "The antenna dome high-speed characterization system for OTA characterization of FR2 5G active antenna panels," in *2024 18th European Conference on Antennas and Propagation (EuCAP)*, pp. 1–5, 2024.

[136] D.-J. Yun, H. Kang, I.-J. Hwang, and Y.-D. Kim, "Direct s calculation using infinitesimal dipole modeling," *IEEE Access*, vol. 11, pp. 118907–118915, 2023.

[137] G. Shaviner, H. Chandravamsi, S. Pisnoy, Z. Chen, and S. Frankel, "Pinns for solving unsteady maxwell's equations: Convergence issues and comparative assessment with compact schemes," 04 2025.

[138] S. Mano and T. Katagi, "A method for measuring amplitude and phase of each radiating element of a phased array antenna," *Electronics and Communications in Japan (Part I: Communications)*, vol. 65, no. 5, pp. 58–64, 1982.

[139] Z. Wang, F. Zhang, H. Gao, O. Franek, G. F. Pedersen, and W. Fan, "Over-the-air array calibration of mmwave phased array in beam-steering mode based on measured complex signals," *IEEE Transactions on Antennas and Propagation*, vol. 69, no. 11, pp. 7876–7888, 2021.

[140] L. Kuai, J. Chen, Z. H. Jiang, C. Yu, C. Guo, Y. Yu, H.-X. Zhou, and W. Hong, "A N260 band 64 channel millimeter wave full-digital multi-beam array for 5G massive MIMO applications," *IEEE Access*, vol. 8, pp. 47640–47653, 2020.

EPILOGUE

In concluding this thesis, it is important to acknowledge that the presented results and conclusions may evolve as machine learning methods and electromagnetic modeling techniques continue to advance. The frameworks and methodologies developed here provide a foundation for integrating data-driven approaches into the design and operation of active array antennas. As machine learning algorithms become more accurate, efficient, and interpretable, their role in electromagnetic system design is expected to grow further. The continuous improvement in computational tools and data availability will allow these models to capture physical phenomena with greater precision, ultimately enabling more reliable, adaptive, and efficient antenna systems. While challenges remain, particularly in ensuring generalization and robustness, the progress in this field is promising and will likely strengthen the connection between physical modeling and data-driven optimization in future research.

ACKNOWLEDGEMENTS

I would like to conclude by thanking the individuals who played a crucial role in the completion of this thesis, whether through their direct input or their ongoing encouragement. My sincere gratitude goes to my promotor and supervisor, *Prof. DSc. Olexander Yarovyi*, for his invaluable guidance and advice. Your support and the reassurance that I could always rely on both you and the group made a real difference throughout this journey.

Yanki, I could easily fill pages just describing how much you've supported me during my PhD. Your hard work and dedication are truly inspiring, and your care for your students goes above and beyond. You've always been there whenever I needed guidance or a word of encouragement, combining your sharp attention to detail with genuine warmth and understanding. Your kindness and support have made this journey not only possible but also much more enjoyable, and I feel very lucky to have had you by my side.

I want to thank all my colleagues in the MS3 group for welcoming me so warmly. My four years in the group have been a true pleasure, largely thanks to all of you, and I'm glad that the end of my PhD does not mean the end of our planned activities. I am particularly grateful to *Ignacio Roldan* and *Tworit Dash* for their invaluable collaboration on parts of my projects. With their support, I was able to make significant progress in my research and successfully bring some of the work to fruition.

I also want to thank *Pascal Aubry* and *Fred van der Zwan* for all their support during my PhD. Pascal, we spent countless hours in the anechoic chamber, facing problem after problem, but your patience and help made it much more bearable, and even fun at times. Fred, thank you for always being there when I needed advice or a hand, and for the fun kiting session that gave me a great break from the research. Special thanks to Esther de Klerk and Minke van der Put for always being there to help with any administrative matters throughout my PhD.

I am grateful to my doctoral committee, *Prof. dr. F.P. Widdershoven, Prof. dr. S. Pollin, Prof. dr.M. Uetz, Prof. dr.M.C. van Beurden* and *Dr. R.F. Remis* for their time, effort, and valuable expertise in reviewing my thesis, and for providing insightful feedback.

I would like to express my deep gratitude to *Muharrem Demirtas*, who has been a great source of inspiration. He taught me not only about electronics but also about mechanics, and his guidance and example have had a lasting impact on my approach to research and learning. A special thanks to *Kaan Alper*, who played a key role in helping me begin my life in the Netherlands. Beyond that, he has always been there whenever I needed technical guidance or personal support. His help and encouragement have made a big difference throughout my journey here, and I am truly grateful.

Finally, I want to express my deepest gratitude to *my family* and *my wife*. Their unwavering support, patience, and encouragement have been my anchor throughout this

journey. They have always believed in me, celebrated my successes, and provided comfort during the challenging times. Without their love and understanding, completing this PhD would not have been possible, and I am truly grateful for everything they have done for me.

About the Author

Nehir Berk Onat received his BSc degree in Electrical Engineering from the Eindhoven University of Technology in 2019. Afterward, he continued his master's study at the same university as a full-time student, and at the Delft University of Technology as a minor student. He specialized in signal processing and electromagnetics groups and received his MSc degree (cum laude) in 2021. He completed his master thesis at MetaSensing B.V. where he has worked on performance analysis and array pattern optimization techniques for monostatic and bistatic spaceborne Synthetic Aperture Radar (SAR) systems. In September 2021, he joined Microwave Sensing, Signals and Systems Group as a PhD candidate.

LIST OF PUBLICATIONS

10. **N. B. Onat**, T.Dash, A. Yarovoy and Y. Aslan, "Machine Learning-Assisted Prediction of Spherical Harmonics and Application to the Synthesis of Accurate MIMO Radar Patterns," in IEEE Antennas and Wireless Propagation Letters, under revision.

9. T. Dash, **N. B. Onat**, Y. Aslan and A. Yarovoy, "Embedded Element Pattern Reconstruction Using Spherical Harmonics to Model Mutual Coupling," International Conference on Electromagnetics in Advanced Applications (ICEAA), Palermo, Italy, 2025, accepted.

8. **N. B. Onat**, I. Roldan, F. Fioranelli, A. Yarovoy and Y. Aslan, "Stacked Generalization for Enhanced Embedded Element Pattern Prediction in Non-Uniform Arrays," in URSI Radio Science Letters, accepted for publication.

7. A. Kannan, **N. B. Onat**, M. S. A. Yarovoy and Y. Aslan, "Detection of Faulty Elements From Sparse Far-Field Data in Active Phased Arrays via Machine Learning," in IEEE Open Journal of Antennas and Propagation, doi: 10.1109/OJAP.2025.3542185.

6. **N. B. Onat**, I. Roldan, F. Fioranelli, A. Yarovoy and Y. Aslan, "Constrained Infinitesimal Dipole Modeling-Assisted Ensemble Prediction of Embedded Element Patterns via Machine Learning," in IEEE Transactions on Antennas and Propagation, vol. 72, no. 9, pp. 7353-7358, Sept. 2024, doi: 10.1109/TAP.2024.3433515.

5. **N. B. Onat**, A. Yarovoy and Y. Aslan, "Sunflower Array of Infinitesimal Dipoles for Constrained Antenna Modeling," 2024 18th European Conference on Antennas and Propagation (EuCAP), Glasgow, United Kingdom, 2024, pp. 1-5.

4. M. Buenaventura-Camps, Y. Aslan, P. Freidl, P. Pascal, **N. B. Onat**, J. Janssen, M. Geurts, A. Yarovoy, "An Aperiodic mm-Wave Phased Array Controlled by Multi-Channel Analog Beamforming ICs," 2024 54th European Microwave Conference (EuMC), Paris, France, 2024, pp. 668-671.

3. **N.B. Onat**, I. Roldan, F. Fioranelli, A. Yarovoy, Y. Aslan, "Dataset Dependency of Data-Driven ML Techniques in Pattern Prediction Under Mutual Coupling", 2024 4th URSI Atlantic Radio Science Meeting (AT-RASC), pp.1-4, 2024.

2. Y. Aslan, P. Aubry, **N. B. Onat**, J. Janssen, M. Geurts and A. Yarovoy, "Heuristic Over-the-Air Calibration of Beamformer ICs in Active mm-Wave Phased Arrays," 2023 IEEE Conference on Antenna Measurements and Applications (CAMA), Genoa, Italy, 2023, pp. 840-845, doi: 10.1109/CAMA57522.2023.10352655.

1. **N. B. Onat**, I. Roldan, F. Fioranelli, A. Yarovoy and Y. Aslan, "Efficient Embedded Element Pattern Prediction via Machine Learning: A Case Study with Planar Non-Uniform Sub-Arrays," 2023 17th European Conference on Antennas and Propagation (EuCAP), Florence, Italy, 2023, pp. 1-5.

ARTICLES PUBLISHED DURING PHD, NOT PART OF THE THESIS

2. N. Van De Kreeke, Y. Aslan, **N. B. Onat** and A. Yarovoy, "Statistical Effects of Propagation Environment and Transmit Array Topology on Cell-Edge User Service Quality at mm-Waves," 2023 17th European Conference on Antennas and Propagation (EuCAP), Florence, Italy, 2023, pp. 1-5, doi: 10.23919/EuCAP57121.2023.10133400.

1. Y. Aslan and **N. B. Onat**, "Optimization of Uniform Amplitude Periodic Linear Phased Arrays for Grating Lobe Reduction," 2022 16th European Conference on Antennas and Propagation (EuCAP), Madrid, Spain, 2022, pp. 1-5, doi: 10.23919/EuCAP53622.2022.9769377.

GRANTS

- TU Delft Space Institute Seed Grant, Project title: "SpaceTaper: A Spatially Tapered Phased Array Antenna for Future Space Communications", 2022.

THESIS CO-SUPERVISED

- A. Kannan, "Detection of Faulty Elements in IC-Controlled Phased Arrays Using Sparse Far-Field Data: A Machine-Learning Approach", *MSc. Thesis*, Delft University of Technology, Sept. 2024.